TÉCNICO LISBOA

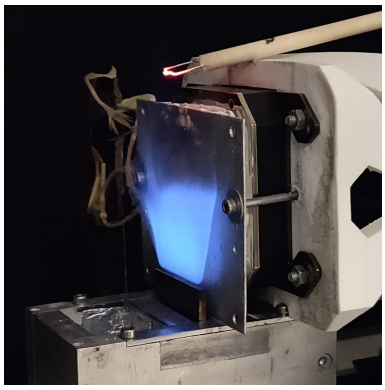

Impact of H_2 on biogas flame-wall interaction for thermoelectric power generation

Miguel Dias dos Santos

Thesis to obtain the Master of Science Degree in

Mechanical Engineering

Supervisors: Prof. Edgar Caetano Fernandes
Dr. Sandra Isabel Godinho Dias

Examination Committee

Chairperson: Prof. Carlos Frederico Neves Bettencourt da Silva
Supervisor: Prof. Edgar Caetano Fernandes
Members of the Committee: Prof. Teodoro José Pereira Trindade
Dr. Rui Pedro da Costa Neto

November 2020

"Shall I refuse my dinner because I do not fully understand the process of digestion?"

Oliver Heaviside

Acknowledgments

This thesis becomes a reality with the kind support of many individuals.

My deep gratitude goes first to my closest family and my parents in particular: Paulo Santos and Isabel Dias. They have always shown supportive and trusted in me for deciding my future since the very beginning of my graduation at IST. Without their help, I would not have the facilitated tools and means to take part in many experiences (academic and others) that deeply enriched me, helped me grew up, and contributed to the person I am today, at the culmination of my academic journey so far.

I would like to express also my sincere gratitude to all professors I came across during my graduation. To teach students, empower them for their future and, at the same time, contribute to a more literate society, is by me considered one of the noblest jobs.

In special, I am grateful to my supervisors Professor Edgar Fernandes and Dr. Sandra Dias. Even though I consider myself a curious person, eager to learn, their interest and critical attitude during this work motivated me and helped to highlight the best of my competences as an (almost) Mechanical Engineer. During this work, I developed a taste for experimental techniques and diagnostics, for which the possibility to work with advanced equipment in the LAB was crucial. I appreciate a lot that opportunity. A special thanks goes also to Dr. António Gonçalves, whose expertise in thermoelectric technology was very important for the type of subject studied.

Finally, I take this opportunity to thank all the friends at IST that made part of my daily routine during the period I have been working on this thesis. That includes long-standing friends: Carolina Guerra, João Castro, João Salgueiro, Micael Coelho, Miguel Carreira, Pedro Messias, Sofia Carreira, Vasco Cepêda; Formula Student (and specially Powertrain) teammates: Henrique Silva, Paula Cunha and Tiago Santos; and the fantastic colleagues I came across in the lab. From the last ones, I am thankful in particular to the ones who worked closely with me and with whom experimental work challenges were overcome together: Alexandre Gamboa, Francisco Vaz, Mafalda Medeiros, Miguel Fechado, Muhammad Raiyan, Filipe Quintino, André Justino and Bruno Gouveia. I wish them all the best in their professional career. I would like to thank all these people for the camaraderie, the share of knowledge and experiences, or even the important discussions at Abílio Spot. Those created a healthy and sociable working environment, and led to what I consider was an incredible period at the end of my MSc degree.

This work was developed at the Thermofluids, Combustion and Energy Systems laboratory of the IN+ - Center for Innovation, Technology and Policy Research.

Resumo

Neste trabalho estudou-se a viabilidade do uso de chamas de pré-mistura de biogás+H_2 para conversão directa de calor em electricidade com um gerador termoeléctrico (TEG). Avaliou-se a influência de diferentes combustíveis e condições de chama nas temperaturas e funcionamento do TEG, que foi colocado em contacto com a parede de uma câmara de combustão, onde uma chama estabiliza em *side-wall quenching*. A transferência de calor da chama e gases queimados para o TEG foi a chave para optimizar a potência e eficiência do sistema. Para tal, analisou-se a velocidade dos gases, a distância de extinção de chama (d_q) e a taxa de geração de calor (HRR), recorrendo a técnicas de PIV e quimioluminescência dos radicais excitados OH^* e CH^*. Desenvolveu-se um modelo matemático para prever o funcionamento do TEG para os diferentes combustíveis e condições de chama, recorrendo ao método dos volumes finitos e a uma rede neuronal. Os resultados do modelo ficaram próximos dos experimentais ($R^2 > 0.97$), ultrapassando-os ligeiramente.

A adição de H_2, mesmo em pequena quantidade (até 20% em volume), revelou melhorias no funcionamento do TEG (+10% de potência) e na estabilização da chama (d_q reduzida em 18%, para níveis do metano). O impacto foi mais significativo para misturas de biogás com mais CO_2, demonstrando o valor do H_2 quando utilizado juntamente com o biogás em aplicações portáteis, com pequenas câmaras de combustão, onde a importância das interacções chama-parede é maior. Verificaram-se correlações entre quimioluminescência, HRR e d_q: a quimioluminescência de OH^* está fortemente relacionada com d_q e a convecção contribui na mesma ordem de grandeza que a condução para a transferência de calor na zona de extinção de chama.

Palavras-chave: gerador termoeléctrico, hidrogénio, biogás, interacção chama-parede, transferência de calor, quimioluminescência

Abstract

In this work, the viability of using premixed biogas+H_2 flames together with a thermoelectric generator (TEG), for direct heat-to-electricity conversion, was studied. We aimed to understand the influence from different fuel blends and flame conditions in TEG working temperatures and operating point. In the setup used, a TEG module contacts a wall of a combustion chamber, where a flame stabilizes in side-wall quenching. The major challenges for power and efficiency optimization were found related to the heat transfer from flame and burnt gases to the wall and TEG. Gases velocity field, flame quenching and heat release rate (HRR) were hence studied via PIV and chemiluminescence of excited OH^* and CH^* radicals. A mathematical model was developed to predict TEG operation for the different fuel and flame conditions, resorting to the finite volume method and a neural network. Its results correlated well with experimental ones ($R^2 > 0.97$), with a small over-prediction.

Even in small amounts (up to 20% in volume), we found that H_2 addition to biogas (BG) improved both TEG operation (power yielded increased by 10%) and flame stabilization (quenching distance d_q was reduced by 18%, to levels typical of methane). The impact of H_2 was more significant for the lower BG grades, which emphasized its importance for BG use in smaller, portable applications, with downsized combustion chambers (where the importance of flame-wall interaction is larger). Correlations between chemiluminescence, HRR and d_q were deduced: it was found OH^* chemiluminescence to be strongly related with d_q and convection to contribute in the same order of magnitude as conduction for heat transfer in the quenching region.

Keywords: thermoelectric generator, hydrogen, biogas, flame-wall interaction, heat transfer, chemiluminescence

Contents

List of Tables

List of Figures

Nomenclature

Acronyms

AD	Anaerobic Digestion.
BC	Boundary Condition.
BG	Biogas.
FWI	Flame-Wall Interaction.
HOQ	Head-on Quenching.
HRR	Heat Release Rate.
HT	Heat Transfer.
HX	Heat Exchanger.
IA	PIV Interrogation Area.
LHV	Low Heating Value.
NN	Neural Network.
PIV	Particle Image Velocimetry.
STP	Standard Temperature and Pressure conditions.
SWQ	Side-wall Quenching.
TEG	Thermoelectric Generator.

Chemical species

Al	Aluminium.
Al_2O_3	Alumina.
CH^*	Methylidyne radical.
CH_4	Methane.
CO_2	Carbon Dioxide.

H_2	Hydrogen.
H_2O	Water.
N_2	Nitrogen.
O_2	Oxygen.
OH*	Hydroxyl radical.

Greek symbols

α	Thermal diffusivity.
β	Camera - wall misalignment angle.
$\Delta\%$	Percentage increase/loss.
Δt	PIV time interval between pulses.
Δ	Absolute difference.
δ_{flm}	Flame thickness.
$\delta_{q,\mathrm{OH}}$	Heat release thickness in the quenching region, derived from OH* chemiluminescence.
ϵ	Under-relaxation factor.
η	Efficiency.
θ	Flame stabilization angle.
κ	Thermal conductivity.
λ	Wavelength of electromagnetic wave.
μ	Dynamic viscosity.
ν	Kinematic viscosity.
ρ	Density.
σ	Electrical conductivity.
τ	Thomson coefficient.
ϕ	Air-fuel mixture equivalence ratio.
χ	Molar fraction.

Roman symbols

A	Area.
c_p	Constant pressure specific heat.

D	Diameter.
d_q	Quenching distance.
E	Electric potential.
E_p	Expected value of probabilistic distribution.
$f/$	Camera aperture f number.
I	Intensity of image pixel.
I_e	Electric current.
$\mathrm{IA}_{x,y}$	PIV interrogation area width, height.
L	Thermoelectric leg half length.
l	Burner slit length.
M	Image magnification factor.
m	Mass.
$\dot{m}$	Mass flow rate.
N	Number of pairs of p and n legs in thermoelectric module.
n	Number of mols.
Nu	Nusselt number.
o_{IA}	PIV interrogation area overlap.
Pr	Prandtl number.
p	Pressure.
P_{flm}	Flame power.
P_{TEG}	Power yielded by TEG.
q	Heat transfer rate.
q''	Heat flux.
$\dot{q}$	Heat generation rate.
$\overline{\dot{q}'''}$	Average volumetric heat generation rate (average HRR).
res	Pixel resolution.
R^2	Statistical coefficient of determination.
R_0	Ideal gas constant.

Re	Reynolds number.
R_e	Electrical resistance.
$R_{e,load}$	Electrical circuit load resistance.
$R_{e,TEG}$	TEG internal electrical resistance.
S	Seebeck coefficient.
S_L	Laminar Flame Speed for an adiabatic, freely propagating flame.
T	Temperature.
U_m	Voltage measured in acquisition board.
U_{oc}	TEG open circuit voltage.
U_{cc}	TEG closed circuit voltage.
$u_{95\%}$	Uncertainty with 95% confidence level.
u_b	Bias error.
u_r	Relative uncertainty.
u_σ	Uncertainty standard deviation.
V	Velocity.
$\dot{V}$	Volumetric flow rate.
w	Burner slit width.
x, y, z	Cartesian coordinates.
Y_F	Fuel mass fraction.
$Z\overline{T}$	TEG figure of merit.

Subscripts

i, f	Initial and final states.
max, min	Maximum, minimum values.
i, j, k, m, n	Computational indexes.
x, y, z	Cartesian coordinates components.
W, E	Left (west) and right (east) elements in finite volume method.
p, n	p-type and n-type thermoelectric semiconductors.
$wall$	Referring to Al plate surface exposed to the flame.

C, H	Cold and hot sides of TEG.
ad	Adiabatic.
b	Referring to burnt gases.
u	Referring to unburnt gases.
$stoich$	Stoichiometric condition or proportion.
flm	Refering to flame.
$flm, 0$	Point of the flame front closest to the wall (quenching point).
$flm, 1, 2$	Points in quenching region bounding the 25% OH^* normalized chemiluminescence intensity of the flame.
q	Referring to quenching.
OH, CH	Derived from OH^* or CH^* chemiluminescence information.
$cond, conv$	Conduction and convection heat transfer.

Chapter 1

Introduction

1.1 Motivation

From temperature rise (both in atmosphere and oceans) to shrinking ice sheets, extreme events and ocean acidification, there is no shortage of signs that climate change is real and is undeniably a serious problem with multiple and uncontrollable consequences. It constitutes a threat to all living beings of our planet and therefore it is a responsibility from the scientific community to work in terms of slowing down and suppress the advance of global warming.

According to the International Energy Agency, in 2017, only 49.21% of the total energy harvested worldwide (19 751 Mtoe) was consumed [1]. Besides that, from the 5313 Mtoe of energy designated to the power plants, only 41.45% were converted into electricity. The rest corresponds to heat generation, from which only 10.96% were used effectively. It becomes important then to adopt energy management tools and study energy conversion processes to diminish this energy waste.

At the same time, with the technological advance, the demand for electricity has risen in rural and remote places, not connected to the grid. Communication antennas, water pumps, household appliances, all rely in an energy conversion process to electrically power them. Besides, for activities isolated from communities (sea and land expeditions, camping, hiking, caravanning), the non-existence of electrical plugs to charge essential equipment such as computers, mobile phones and GPS devices is still an inconvenient.

Among different possible technologies to cover these problems, like solar photovoltaic systems (combined with batteries for energy storage), thermoelectric generators (TEGs) are yet to be fully exploited. They are of great interest due to their easy deployment and implementation. This allows them to generate electricity noiselessly, harvesting energy from any kind of heat source or reusing waste heat in a smart way. The absence of emissions in their long lifetime operation makes also thermoelectrics competitive in what regards carbon footprint.

The combustion of adequate fuels with appropriate and optimized processes remains a suitable (and often unique) option for heat and power generation. Nowadays, renewable and bio fuels in particular have a say in what regards energy systems decarbonization. One cannot be indifferent to the high specific energy (50 MJ/kg for methane) and power ($\sim$ 1000 W/kg for internal combustion engines) of

fuels and related technologies [2]. For these reasons, combustion proves capable of accompanying or even change the *status quo* of energy management for lightweight and portable applications. Fuels can help extend the devices operation times and eliminate the risk of unexpected energy shortage in the mentioned inhospitable environments, not connected to the grid.

Biomass anaerobic digestion (AD) produces biogas from organic matter which, if disposed without any treatment, would be harmful to the environment. Biogas (BG) lowers greenhouse gas emissions, avoids soil and water contamination from used biomass and helps reduce dependence on fossil fuels. That said, biomass AD has all the ingredients to expand in the near future, specially in rural and underdeveloped regions, for the urgency in increasing populations quality of life, boost economic development and ensure energy security.

The weak combustion properties of BG constitute, however, a handicap for its use in such small applications. On the contrary, hydrogen (H_2) has unrivaled combustion properties (fast burning rate, large flammability limits and small ignition energy, for example). Many of the research conducted now is directed to its use as fuels dopant, in order to enhance their burning characteristics. Biogas is one of the fuels where this H_2 addition produces interesting results, which can play an important role in the dissemination of BG technology. Putting into perspective the mentioned potential of fuels to serve as energy source for portable devices, there is an increasing importance of flame-wall interaction (FWI) as combustion chambers get downsized and have larger surface to volume ratios. For those situations, FWI becomes the predominant phenomena controlling aspects like flame stabilization, heat transfer and pollutants formation.

1.2 Thermoelectric technology

1.2.1 Theoretical background

Thermoelectric modules are devices capable of converting electricity into heat (or vice versa) in a noiseless, simple and reliable operation. They rely on thermoelectric semiconductors to do so. In a module, these are designated legs and are electrically connected (usually in series) using metallic conductors, as Figure 1.1 illustrates. The mentioned components are fixed to ceramic plates, whose mechanical properties confer integrity to the assembly and protect the components from the eventual harsh exterior environment.

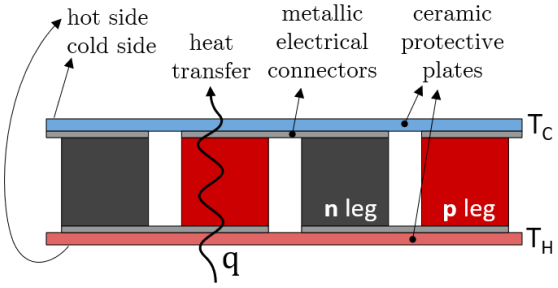

Figure 1.1: Components of a thermoelectric module; heat flows from the hot plate, at T_H, to the cold one, at T_C, through p and n legs.

There are two types of thermoelectric materials in any thermoelectric module: a n-type and a p-type. The n-type semiconductor is doped with atoms of materials with more electrons in their valence band (than the base material), while the p-type is doped with atoms with less electrons in their valence bands. This creates negative and positive carriers in each of the legs. For the case of a thermoelectric generator, heat is supplied to the module to generate electricity. When a temperature gradient in the module is created by the heat flux, the charge carriers will diffuse through the material and generate an electromotive force. This will drive the electrons when the circuit is closed and generate power. If the module is operated as a thermoelectric cooler, it generates heat from a electric power source and the order of events is the opposite.

For a given amount of heat absorbed by the thermoelectric generator (TEG), the power that the thermoelectric can yield will increase whenever the temperature difference between each side increases. This is accomplished with a small thermal conductivity across the module. In order to take advantage of that temperature gradient and generate electricity, a higher Seebeck coefficient difference ($S_p - S_n$) will allow to generate a larger voltage drop in each leg. Finally, in order to maximize electric current in the module for that accumulated voltage, the TEG electrical resistance $R_{e,TEG}$ should also be small; for that purpose, the conductive parts need to have a small electric resistance.

The aspects referred in the last paragraph can be translated into the quantity designated dimensionless thermocouple figure of merit $Z\overline{T}$, defined as:

$$Z\overline{T} = \frac{S_{p-n}^2}{K\,R_e}\,\overline{T} \tag{1.1}$$

It is used to measure the conversion efficiency between electricity and heat for a certain p-type and n-type materials. The thermal conductance $K = \kappa L$ is the parallel equivalent of the two materials, while $R_e = L/(\sigma A)$ is their average electrical resistance (they are connected in series). If constant properties are assumed, they should be evaluated at temperature $\overline{T}$, which is the average between the hot and cold operating temperatures (T_H and T_C).

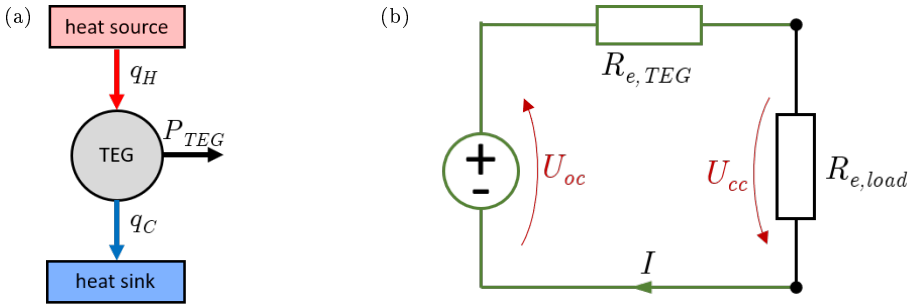

Figure 1.2: Thermoelectric generator (a) thermodynamic and (b) electrical analogues.

In this perspective, the TEG can be interpreted as a thermodynamic system (Figure 1.2a) with a well defined efficiency η_{TEG}:

$$\eta_{TEG} = \frac{P_{TEG}}{q_H} \tag{1.2}$$

where only a certain amount of heat absorbed q_H can be converted into electrical power P_{TEG}. The rest,

q_C, is rejected to the heat sink. In the electrical perspective, and as Figure 1.2b illustrates, the power yielded P_{TEG} is consumed in the load resistance $R_{e,load}$, connected to the TEG terminals. By deriving an equation for P_{TEG} as function of the value of that load resistance, it can be demonstrated that the function has a maximum when $R_{e,load} = R_{e,TEG}$ [3].

For a typical operating condition of the TEG used in this thesis (characterized by a open circuit voltage U_{oc} and internal resistance $R_{e,TEG}$), current I_e and power P_{TEG} curves are derived from the electric circuit analogue and displayed in Figure 1.3a. It can be seen that the power output is very sensitive when $R_{e,load} < R_{e,TEG}$, where it exhibits a sharp decrease. For matched load (and maximum power) conditions, the close circuit voltage is half the voltage generated by the TEG, *i.e.* $U_{cc} = U_{oc}/2$ (Figure 1.3b). These curves were verified experimentally by Oliveira, T. [4], working with the same thermoelectric device.

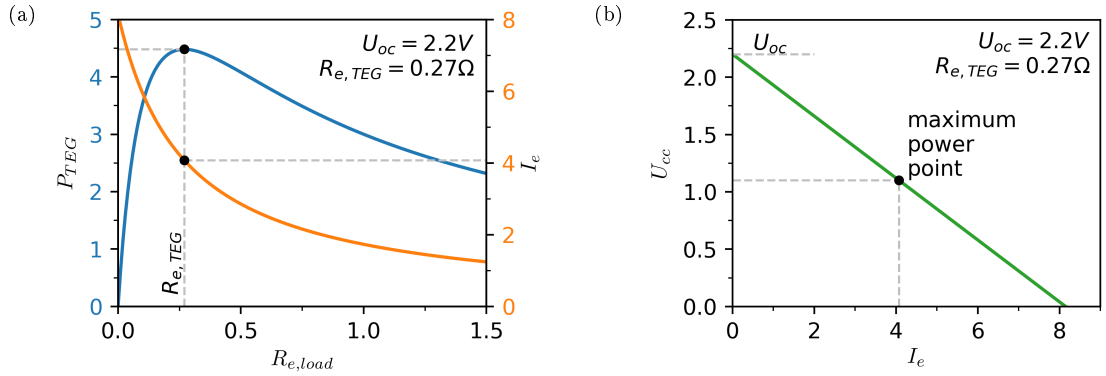

Figure 1.3: Influence of load resistance value $R_{e,load}$ in TEG operating point for (a) power P_{TEG} yielded, circuit current I_e, and (b) close circuit voltage U_{cc}.

In ideal operating conditions (no heat losses and matched load resistance), it was demonstrated algebraically that η_{TEG} is proportional to Carnot's efficiency by a factor which depends on the thermoelectric figure of merit $Z\overline{T}$ [5, 6]:

$$\eta_{TEG} = \left(1 - \frac{T_C}{T_H}\right) \frac{\sqrt{1 + Z\overline{T}} - 1}{\sqrt{1 + Z\overline{T}} + \frac{T_C}{T_H}} \tag{1.3}$$

1.2.2 Applications and technological advances

In the early days of TEG devices, their use was mainly restricted to niche applications, valued for their reliability when operating in extreme environments. Nowadays, the engineering community is recognizing the potential of this technology to be applied in a vast range of applications [7, 8].

Thermoelectric devices have been successfully implemented to manage waste heat and help processes to get closer to Carnot's efficiency, in industrial [9] and transportation [10, 11] sectors. By controlling the power drawn (given) from (to) it, heat fluxes and temperatures can be imposed in several equipments [12].

The electricity generation in severe environments, where undeniable fidelity is required, is one of the most successful applications of TEGs. The use of thermoelectric technology in voyager I and II satellites are the ultimate proof of its reliability [13], with the TEGs in those space missions working ceaselessly for 43 years by the time this text was written. The heat generated from the natural radioactive decay

of plutonium 238 (around 7000W), the TEG supplies 423W of electricity to power the satellite instruments and transmission electronics, in places sunlight cannot reach. As another interesting application, researchers investigated and tested the generation of electricity from deep-sea hydrothermal vents [14]. That turned out to be a great solution for deep-sea observation, in locations where access with cabled instrumentation is impractical.

The last group of most relevant applications relates to the decentralized domestic power and heat generation. The low power requirements combined with the low population income makes grid connection not viable in many rural places. In developed countries, connection to the grid is not a problem but in many situations people are looking for greener solutions. In any of the cases, TEGs can help decrease the use of primary fuel for electricity generation and also help to heat any facility, constituting therefore a combined heat and power generation system.

Cascade TEG systems optimized to work with different temperature levels were also investigated [15], with efficiency improvements of 21.56% from a single stage system.

Despite the potential described for the different areas, the majority of researchers are aware of the work yet to be done seeking cheaper and better thermoelectric materials, that certainly would increase the competitiveness of this technology for electrical power generation. Beretta *et al.* [6] made an extensive revision of the state of the art materials, with an interesting analysis of their evolution from 1950 to the present. The recent technological advances led to significant improvement in the figures of merit since the beginning of the twenty-first century.

Scientists distinguish thermoelectric materials suited for low (below 450 K), medium (450 K to 850 K) and high temperatures (above 850 K), depending on the temperature of peak $Z\overline{T}$. Bismuth telluride is the material which yields higher figures of merit for the low temperature range, with a maximum registered $Z\overline{T} = 1.9$. In the mid temperature range, the best performing materials are lead telluride and its alloys (with an average $Z\overline{T} = 1.7$ and a peak of 2.5 for 923 K. Finally for the high temperature range, the figures of merit are around 1, promoted by Silicon-germanium alloys, oxides and Zinc compounds.

To give an example, for a cold temperature of 300 K and a hot temperature of 450 K, a thermoelectric device with $Z\overline{T} = 1.9$ would have, at its best, 9.9% conversion efficiency (Equation 1.3).

1.3 Biogas

Among different possible options for renewable energy sources, bioenergy ones are considered competitive and atractive. The International Renewable Energy Association shows, in a 2018 report [16], that bioenergy LCOE [1] of 0.062 USD/kWh for electricity generation is one of the lowest among the different renewable energy options (Figure 1.4) and close to the lower limit of fossil fuel range. It also does not suffer from dispatchability (rapid response to the grid demands) nor availability issues, typical from other renewable sources such as Solar PV, Wind Energy or even Hydro.

[1] The Levelised Cost of Electricity (LCOE) is an economic assessment of the average total cost to build and operate a power-generating asset over its lifetime divided by the total energy output of the asset over that lifetime. The LCOE calculation considers all plant-level costs, such as initial investments, operation costs and fuel costs during the power plant's lifetime.

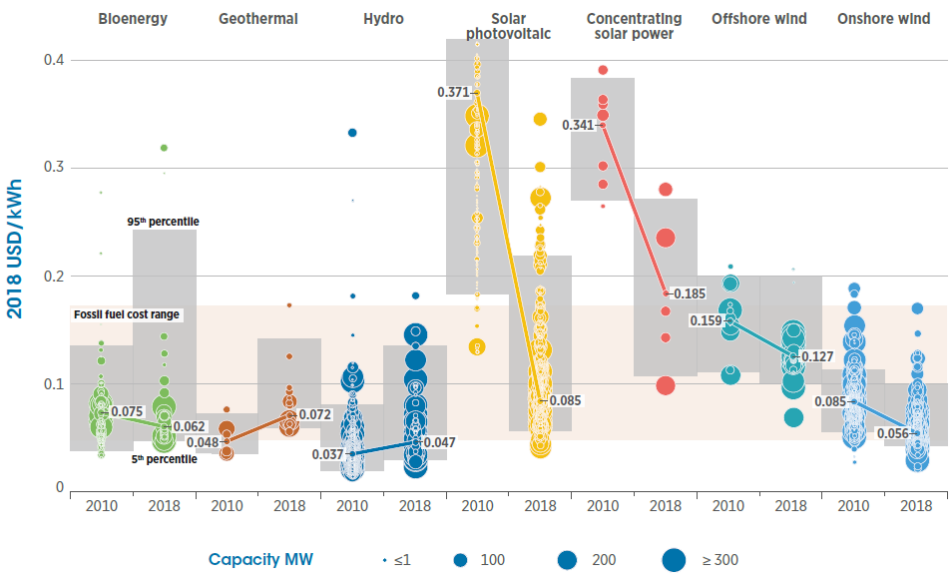

Figure 1.4: Global LCOE of utility-scale renewable power generation technologies, from 2010 to 2018; the single horizontal band in the background represents the fossil fuel-fired power generation cost range, while the vertical bands for each technology and year represent the 5th and 95th percentile bands for renewable projects (adapted from IRENA 2019 [16]).

The European Commission proposed to set a greenhouse gas emission reduction target for domestic EU emissions of 40% in 2030, relative to emissions in 1990 [17]. In 2014, when this decision was communicated, the figure attained was only of 21%. Furthermore, they announced that "food-based bio fuels should not receive public support after 2020". This led to a increasing importance of biomass anaerobic digestion over other bioenergy renewable sources.

Biomass anaerobic digestion (AD) is a pure biochemical process, conducted by bacteria in an oxygen free environment, where the organic molecules in biomass are destroyed and biogas (BG) is produced. There are plenty of possible biomass types for AD like water treatment plants sludge, manure, municipal solid waste and agri-food industry waste [18]. Biogas can be collected in landfill as well as in dedicated digestors. When anaerobic digestors are used, the typical methane (CH_4) volume percentage in biogas ranges from 50% to 75%, depending mainly on the biomass composition, type of reactor, residence time and bacteria ambient conditions. CO_2 and CH_4 together account for more than 95% of the composition of BG produced by anaerobic digestion [18, 19]. An upgrade and purification of biogas is normally required to remove CO_2 and other contaminants (like H_2S and siloxanes, with a typical concentration below 1000 ppm_v[2]) that can corrode and damage engines and combustion chambers. Processes for CO_2 removal include a scrubbing (with water or organic solvent), pressure swing adsorption, membrane separation or even cryogenic separation. For any of these processes, final concentrations of CH_4 above 96% can be attained [19].

Available statistics show that Europe is pushing on biomass AD technology. It solely was responsible for roughly half of the 61 billion m^3 of biogas produced globally in 2016, while Asia share was around 30% [20]. In 2015, the installed biomass AD capacity was 15GW at global level (where 10.4GW were

[2]parts per million on volume basis

allocated to Europe) [21]. From several published articles assessing the current status of biomass AD and its potential, Scarlat *et al.* [22] made a detailed, geographical analysis to show what can be the installed biomass AD capacity in Europe, just dedicated to manure waste. They predicted a range from 6.14GW to 7.15GW, with greatest potential in Bretagne, Benelux and Po valley regions.

This technology also proves to have a great potential in developing countries, for which several rural household digesters are being developed to serve as family size biogas plants [23]. Biomass AD is also a powerful waste management tool: the remaining waste after the anaerobic digestion process is no longer harmful to the soil and can be used as a natural fertilizer. The heat generated during the process can also be used to warm any facility close to the plant (for example greenhouses or housing).

1.3.1 BG + H_2

Hydrogen is one of the of the most abundant elements on earth. In nature, it is usually present as water or organic compound forms, rather than H_2 molecules. There are already several ways to obtain hydrogen in renewable industrial processes (which is denominated renewable H_2): reforming renewable fuels (biogas included), by water electrolysis (using excess electrical power from the grid and avoiding curtailments), or even with the fermentation of certain biomass [24].

Hydrogen produced this way is also of great interest for energy storage in large scale, for long periods of time. However, its low volumetric energy density compared to other fuels (shown in chapter 1.4), is still an inconvenient for certain storage infrastructures. In comparison with methane, hydrogen needs three times more space to store the same amount of energy, for a certain pressure and temperature. The types of storage are diverse: gaseous (pressurized at lower temperatures), as cryogenic liquid, chemical, and physical (using carbon nanotubes adsorption, for example). This constitute an important topic of research in hydrogen technology [25].

Despite this, its blend with biogas has made possible the direct use of BG in burners, without the need for upgrading and purification. At the same time, the use of small amounts of hydrogen as fuel dopant constitute an intermediate step in the growth of H_2 technology, driving the build of infrastructures for production and distribution of hydrogen.

Internal combustion engines have been the main focus of study of the H_2 addition to biogas. The results are homologous for different engine types and can evidence in which manner biogas combustion is influenced. Researchers report improved power and higher cylinder peak pressure thanks to faster combustion and increased heat release rate (HRR) [26]. Exhaust hydrocarbons and CO_2 concentrations diminished, and lean misfire limit improved, as percentage of H_2 increased [27]. In a $700\,cm^3$ spark-ignition engine, for $10\%H_2$, hydrocarbons emissions near stoichiometry were reduced by 56% [28]. Best thermal efficiency improvement occurred between 5% and 20% of H_2 addition (depending on the engine type and biogas composition), beyond which heat losses became significant [29]. The major disadvantages were related the increased NOx emissions (due to higher flame and burnt gases temperature) and the need to retard the ignition timing to avoid knock (due to the faster flame speed).

1.4 Fuel properties and flame-wall interaction

Burning characteristics of fuels are dependent on the chemical composition of reactants (fuel, oxidant and catalysts) and ambient related variables (pressure, temperature and flow fields). These will influence and dictate the propagation mechanisms of flames in a complex manner, sometimes difficult to describe and model with accuracy. Nevertheless, those lead to a set of combustion properties, used to characterize and evaluate the fuel on several levels. These are fundamental to help engineers choose the most suitable fuel for a certain application. The most common ones, for premixed flames, are: heat of combustion (LHV or HHV); stoichiometric air-fuel ratio (AFR); flammability limits; laminar flame speed (S_L) and ignition energy. For the type of fuels used in this work, Table 1.1 contains some of their burning characteristics.

Table 1.1: Combustion properties of methane [30], biogas (66.4%CH_4, 30.6%CO_2, 3%N_2) [31] and hydrogen [32] with air, at ambient temperature (298 K) and atmospheric pressure

Property	CH_4	BG	H_2
LHV [MJ/kg$_{fuel}$]	50.0	21.68	120.0
LHV [MJ/dm$^3_{fuel}$]	32.77	21.48	9.90
AFR [kg$_{air}$/kg$_{fuel}$]	17.12	7.31	34.00
Flam. limits [AFR$_{stoich}$/AFR]	0.53 - 1.56	0.6 - 1.2	0.14 - 2.54
S_L (for $\phi = 1$)	0.36	0.26	2.1
T_{ad} [K]	2236	2129	2527

The influence of mixing different fuels is usually grouped in reaction kinetics, thermal or species dilution effects. All of them are strongly interconnected and, in general, whenever one of them is affected, it can be a cause or consequence of any of the other two e.g., faster chemical reactions are associated with higher flame temperatures, faster diffusion, and higher concentration of species in the flame front; if any of these is affected in the opposite way, the other two will escalate in the same manner.

When CO_2 is blended with CH_4 (and H_2), it does not contribute to increase the heat of combustion, since in a complete reaction it is not consumed. From the different abundant species present in hydrocarbons combustion, CO_2 molecule has the highest constant-pressure specific heat (c_p) [33]. With this, the thermal inertia of the mixture is increased (considered to be the principal effect of CO_2 addition [34]) and the flame and burnt gases temperature reduced. Wei *et al.* [35] emphasizes chemical effects as well: the chemical path of reaction is altered, less exothermic reactions are favored, leading also to decreased HRR. These constitute the main causes for other side effects on the combustion reaction, which contribute for the poor performance of biogas mixtures on several combustion applications.

The introduction of H_2 can help mitigate these problems. Hydrogen can act in combustion process on several levels at the same time. Increased thermal and species diffusion, along with less relatively slow reactions of CO oxidation into CO_2 (present in hydrocarbon flames), will promote faster kinetics, more intense flames and higher S_L [33]. The raised concentrations of species that have a pivotal role in the HRR [35, 36] will promote higher reaction rates and also raise flame temperatures. Tang *et al.* [37] quantified the contribution of each aspect to the combustion of H_2 with methane. They concluded that the kinetic effect is the most important, followed by thermal effect. The dilution effect was the less important of the three. Nevertheless, the last aspect should not be forgotten when dealing with biogas, since adding H_2 to the fuel blend will also reduce the final molar fraction of non combustible fuel (CO_2).

1.4.1 Flame-wall interaction

Combustion applications rely on the use of walls and geometries on several aspects. Engineers use them to stabilize flames, promote air-fuel mixing or even control temperature, flow and pressure fields of burnt gases in a combustion chamber. FWI encompass multiple phenomena that arise from the development of flames in the vicinity of walls (Figure 1.5), inevitable in many situations. These have a pivotal importance for many power generation applications, where the control of heat transfer from flame to wall can help increase system efficiencies and make competitive processes and equipments. Even if heat transfer is not prioritized, FWI will largely affect pollutants formation, flame instabilities, acoustics and wall temperatures. These in turn will have a significant impact on the lifetime of combustion chambers [38].

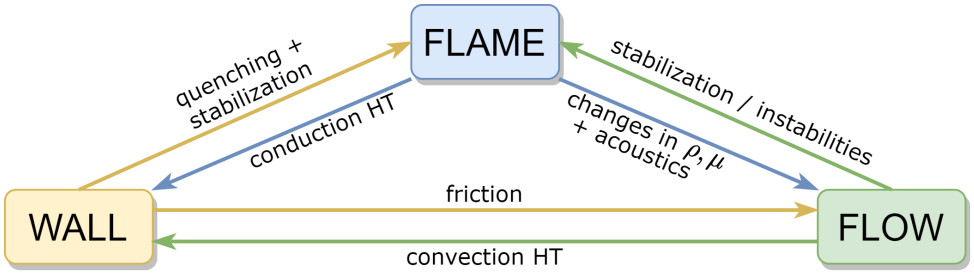

Figure 1.5: Mutual dependence of flame, wall geometry and flow for several important phenomena related with combustion.

Due to aspects such as (i) small time and length scales, (ii) strong temperature and species concentration gradients and (iii) ambiguity in defining flame front boundaries, there is a consensus in scientific community to consider FWI a complex process, difficult to model and study experimentally, without simple interpretation and explanation of results.

From the different FWI phenomena, quenching refers to the process of flame extinction near a cold wall. Its governing mechanisms, for premixed flames, can be understood from mass and energy diffusive processes, which are the base for flame propagation. Mass diffusion is mainly governed by differences in radicals or molecules concentration; however, at lower temperatures and for species with small molecular weight (H, H_2), the contribution from temperature gradients in mass diffusion (Soret effect) is not negligible [33]; if present, strong pressure gradients can promote mass diffusion also. As for energy diffusion, the main contributions come from heat conduction and energy transport due to mass diffusion; Dufour effect (the counterpart of Soret effect), is important only to the extent of the same particular conditions where Soret effect is present. Radiation is negligible in premixed lean/stoichiometric flames (used in this work) due to the absence of yellow flames and wavelengths in the red and infra-red regions.

For most cases of quenching, flame extinction is attributed to heat losses. If the flame burns closer to the wall, it will lose more heat, its temperature will decrease and combustion reaction rates diminish. This will make it impossible for the flame to survive, forcing its retreat farther away from the wall. The opposite will happen if the flame is found capable of losing more heat. There is hence an equilibrium between the heat generated by combustion and the heat transferred to the wall. Temperature serves as an indicator of the heat required to activate chemical reactions. Westbrook *et al.* [39] claim that a CH_4 +

Air premixed flame in quenching extinguishes close to the 1500 K isothermal. Beneath this temperature, reaction rates decrease sharply and flame extinguishes. Analysis to the temperature of maximum HRR location in a freely propagating flame confirm that those are close to 1500 K [40], supporting this theory. The characteristic length at which the flame stabilizes is designated quenching distance, d_q. It has a minimum around $\phi = 1$, when the amount of heat released is greater and at a higher rate.

The use of different type of burners in different types of applications led to multiple definitions of quenching distances. Those are illustrated in Figure 1.6. Whenever the flame lays in between two parallel walls (or inside a tube), it is defined as the minimum distance (or minimum diameter) for which the flame can propagate (Figure 1.6a). If the case studied involves only a single wall (Figure 1.6b), then two situations and definitions of d_q can be distinguished, depending on the direction of flame propagation relative to the wall: head-on quenching (HOQ) and side-wall quenching (SWQ). For any of the situations described, the definitions of d_q remain the same for stationary/transient and premixed/diffusion flames.

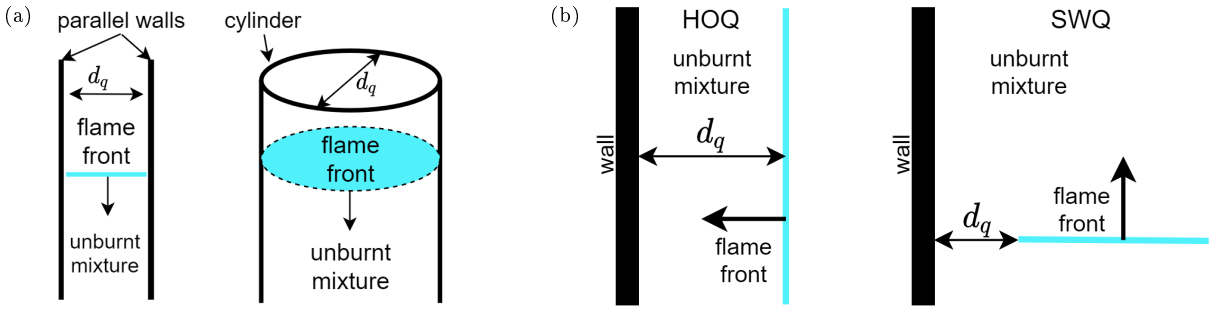

Figure 1.6: Quenching distances measurements for (a) double wall/cylindrical and (b) single wall systems; for single wall systems, quenching is classified as head-on quenching (HOQ) or side-wall quenching (SWQ).

Since the quenching zone is very small (d_q in the order of 1 mm or below) and temperature difference between cold wall and flame is high (around 1000 K), the importance of heat diffusion is considerable. For that reason, heat flux to the wall is widely described as pure 1D conduction, based of Fourier's Law ($\overline{\kappa}$ is the mean thermal conductivity):

$$q''_{cond} = -\kappa \frac{dT}{dx} \;\Rightarrow\; q''_{cond} = \overline{\kappa} \frac{T_{flm} - T_{wall}}{d_q} \tag{1.4}$$

If quenching is governed heat losses, and given the mentioned assumption of flame extinction near a well defined flame isothermal, one can deduce from Equation 1.4 that d_q decreases when T_{wall} increases. In fact, this is what is observed in many works that assessed the influence of a inert wall temperature in flame quenching in SWQ [41–43] and HOQ [44–46] configurations.

Nevertheless, if the wall surface (T_{wall}) and mixture temperatures become high enough, heat conduction is accompanied by facilitated mass diffusion and radical recombination reactions at the surface. Those reactions have a low activation energy and are promoted by species that have a pivotal importance in the preheat/induction zone of the flame, to generate heat at lower temperatures and start chain-branching reactions. When the flame is depleted of those important species in the quenching zone, it is forced to stabilize at a higher d_q. The higher quenching distances do not necessarily mean, however, less heat transfer to the wall: since the recombination reactions in question are considerably exothermic

and occur at the wall surface, they can contribute in large amount to the overall wall heat flux and compensate for the reduced q''_{cond} from flame heat losses (Equation 1.4) [47]. Radical consumption at the surface and flame heat losses always coexist, although with different relative importance [48]. The onset temperature of non negligible contribution of radical recombination reactions will depend not only on the surface temperature, but also on the concentration and type of species present in the flame.

1.5 State of the art

The first successful attempt to use the heat from a flame for a practical power generation application using TEGs came in the beginning of the cold war period, thanks to the findings of a Soviet physicist, Abram Ioffe, about thermoelectric semi-conductors. The United States emitted a secret engineering procurement of a "Russian Kerosene Radio set" , dated August 1956, after knowing about this innovative concept. Soviets were using the heat from a kerosene lamp and metallic fins to create a temperature difference around 270 K, sufficient to generate 2 W of electricity from a TEG and power a small radio. A picture of it is displayed in Figure 1.7.

Figure 1.7: The use of a TEG incorporated in a kerosene lamp to power a small radio was idealized by Soviets in the beginning of cold war; those were useful in rural places of Siberia and China, not yet electrified.

Regarding recent published works about use of flames for dedicated thermoelectric power generation, Jiang *et al.* [49] used a 150 W lean ($\phi = 0.7$) dimethyl ether flame, stabilized in a small, separated combustion chamber. The burnt gases pass through a small channel, in contact with two TEGs cooled by water. The system had a maximum power output of 2.5 W and a best overall efficiency of 1.25%. In their setup, leaner flames benefited efficiency while stoichiometric ones maximized power output.

The use of a heating cup to pre-heat the air-fuel mixture [50] allowed to increase the stability limits of a small liquefied petroleum premixed flame, inside a 4 mm diameter combustion chamber. This permitted to stabilize a flame from 1 W to 20 W and therefore explore the best working conditions. Using two TEG modules heated by burnt gases, they produced 1.56 W and could attain 2.56% efficiency. If adaptations were made to include two more TEGs, these figures would rise to 2.35 W and 4.6%, respectively.

Shimokuri *et al.* [51] stabilized a propane flame (400 W to 600 W) using a small scale vortex combustor. Two water cooled TEGs yielded a large power of 18.1 W, with a reasonable efficiency of 3.01%. The

amount of heat transferred from flame to TEG reached figures above 70% thanks to the vortex combustor, that faciliated flame stabilization and increased flame surface area.

Aravind *et al.* [52] in their recent works developed a more efficient device. It also has two TEG modules in contact with the exterior walls of a micro combustion chamber and uses the heat from two small liquefied petroleum flames. The TEGs are cooled by water and yielded 4.5 W. The conversion efficiency reached a remarkable figure of 4.66% for $\phi = 0.9$. They indicate a power density for the whole system of $0.14\,\mathrm{W/cm^3}$, also notable in these concepts.

On commercial level, Gentherm, a company focused on remote power generation solutions, sells different generators with nominal power ranging from 30 W to 500 W. The 30 W model, shown in Figure 1.8, has $348 \times 356 \times 450$mm dimensions and weights 20 kg (excluding gas canister) [53]. It can work either with methane or propane and is cooled by fins through natural convection. If working with CH_4, it consumes 1.38 SLPM[3], which will lead to a global efficiency of 3.64% for that rated power. The best working point is tuned by the user, regulating the amount of air intake (and thus mixture air-fuel ratio) and measuring the voltage generated across the TEG.

Figure 1.8: Gentherm 5030 thermoelectric power generator is the smallest of a vast range of models commercialized by Gentherm; it yields 30W of electricity using a methane or propane flame [53].

Despite the reduced number of published works and commercialized products, all of them share a common concern for a proper burner design, to favor flame stabilization and heat transfer to the thermoelectric device. Those aspects are essential to allow for posterior efficient and powerful operation which, of course, will also depend on the choice of a suitable thermoelectric.

In a previous work [4], developed in a similar setup used by us, the possibility to use a flame for thermoelectric power generation was investigated successfully using a CH_4 + air premixed flame.

Although multiple types of fuels were used in the examples given, there is no record or references to renewable fuels. This is not aligned with the discussed relevance and potential of them in fighting climate change and reduce global inequality in rural areas, where these decentralized power generators can be extremely useful.

[3] standard liters per minute

1.6 Scope of the work

Given the arguments and considerations about (i) the potential of thermoelectric technology (in harvesting energy from multiple heat sources); (ii) the importance of fuels and biofuels (specially biogas, for rural and remote locations); and (iii) the relevance of flame-wall interaction for the trending small and portable applications [54], a study that contributes to advances in all three aspects is proposed, aligned with what is believed can integrate the energetic paradigm in the near future.

In this thesis, with the objective to fill the void in the use of renewable fuels for thermoelectric power generation, biogas and hydrogen are used to create a lean/stoichiometric premixed flame. Hydrogen is added in small amounts (10% and 20%) to two biogas mixtures, with different compositions. A TEG module, together with the flame, generates electricity in a compact assembly. The impact in power and efficiency are quantified, with respect to fuels and flame conditions used. In any of the research works cited in the state of the art, TEGs are heated with flue gases of small, separated combustion chambers, and are not in close contact with any flame, as it happens in our setup.

A focus is made on the role of H_2 in overcoming the challenges of biogas combustion in small and portable applications. For that, flame-wall interaction is extensively studied in the perspective of side-wall quenching and velocity flow field. Their effects on the heat transfer to the TEG will be interpreted. No research on the influence that H_2 has in biogas quenching distance was found by the time this thesis was written.

In the process, important considerations and useful techniques/methodologies to study thermoelectric power generation and FWI are described. In particular, alignment methods (required for d_q measurement) are defined, and chemiluminescence of OH^* and CH^* flame radicals is used to identify flame front and obtain information about heat release rate HRR.

Key aspects to take into account for harvesting power and increase efficiency with this flame+TEG configuration will be explained in what regards both flame condition and thermoelectric device. A mathematical model, capable of predicting with accuracy the outcome of using different flames and fuel compositions in power harvested and efficiency, was also developed.

Chapter 2

Mathematical model

The development of a mathematical model can lead to a better understanding of electric and thermal phenomena involved in the production of electricity with TEGs. It can also be useful in the experimental work, when deciding between different methods and equipment (choice of the most suitable load resistance value, for example). Finally, if an optimized concept is to be commercially distributed, it will be of great value if power output and conversion efficiency could be controlled according to the load demands, by changing fuel and flame condition. That control will be more precise and robust if there is a complete mathematical description.

The mathematical model developed in this work aims to provide the power yielded (P_{TEG} [W]), TEG electrical internal resistance ($R_{e,TEG}$ [Ω]), current (I_e [A]), hot and cold side temperatures (T_H, T_C [K]) and heat fluxes (q_H, q_C [W]). Other variables, such as efficiencies, can be computed from these ones.

To do so, the model requires several inputs related with fuel composition (biogas composition and H_2 concentration), flame condition (air-fuel equivalence ratio ϕ and burner Reynolds number Re) and the electric load resistance $R_{e,load}$ [Ω].

Five major simplifications were assumed in this model:

1. Homogeneous TEG surface temperatures T_H and T_C;
2. No heat losses to the surroundings, which implies that temperature gradients are one dimensional in the TEG's legs;
3. Electrical connectors between p and n legs (Figure 1.1) have high thermal and electrical conductivities (κ and σ, respectively) and thus do not generate temperature differences or voltage drops;
4. Negligible thermal and electrical contact resistances between all parts;
5. Isotropic properties of thermoelectric materials.

The model uses the finite volume method to solve non homogeneous, second order differential equations (chapter 2.2) and a neural network to translate flame and fuel boundary conditions (BCs) to TEG BCs (temperatures and heat fluxes), described in chapter 2.3.2.

2.1 Governing equations

The process of direct heat-to-electricity in the TEG encompasses different thermoelectric effects in both p and n legs, illustrated in Figure 2.1. All the effects occur between $-L < x < L$, which was the domain considered in the mathematical model (L is the leg half length). The TEG contains N pairs of legs connected electrically in series and thermally in parallel. For the TEG module used in this work, $L = 1.9\,\text{mm}$ and $N = 49$.

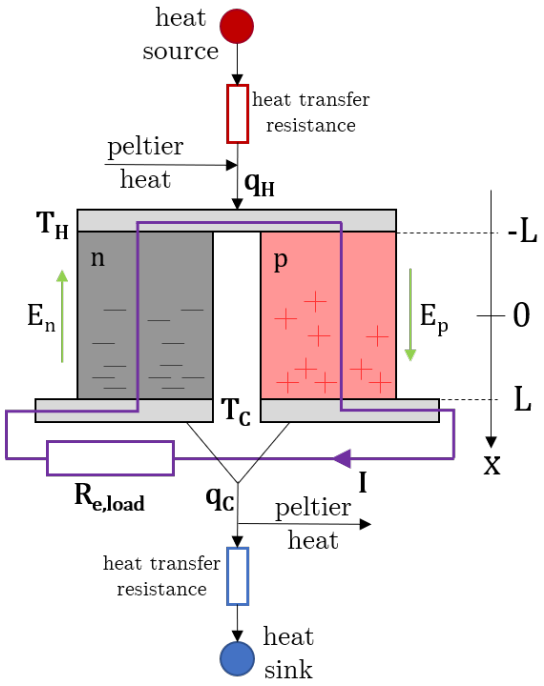

Figure 2.1: Thermoelectric phenomena and relevant thermal and electrical variables in p and n legs; the TEG cointains N pairs of legs.

These thermoelectric effects are: heat conduction q, in each leg (with section area $A_{leg} = 20.25\,\text{mm}^2$), due to strong temperature gradients between hot and cold sides

$$q = A_{leg}\,\kappa\,\nabla T\ , \tag{2.1}$$

where $\kappa\,[\text{W}/(\text{K m})]$ is the thermal conductivity of the material; heat generation $\dot{q}\,[\text{W}]$, when electrical current $I_e\,[\text{A}]$ flows throughout the leg with conductivity $\sigma\,[\text{S/m}]$ (Joule heating)

$$\dot{q} = \frac{2L}{A_{leg}\,\sigma}\,I_e^2\ ; \tag{2.2}$$

Thomson effect, which is the heat generation (absorption) when electrical current flows in the direction of increasing (decreasing) temperature in a material. It is characterized by the Thomson coefficient $\tau = T \times dS/dT$ (where $S[\text{V/K}]$ is the Seebeck coefficient)

$$\dot{q} = -\tau\,I_e\,\nabla T\ ; \tag{2.3}$$

the Peltier effect where heat is generated or absorbed when electrical current flows through junctions with a discontinuity in Seebeck coefficient

$$\dot{q} = I_e \, \Delta S \, T \, , \tag{2.4}$$

which allows the thermoelectric module to convert electricity into heat; and finally, the Seebeck effect (considered the counterpart of Peltier effect) is the build up of an electric potential $E\,[\mathrm{V/m}]$ across a temperature gradient, proportional to the Seebeck coefficient

$$E = -S \, \nabla T \, . \tag{2.5}$$

The different effects can thus be inserted in an energy balance equation for p and n legs:

$$\begin{cases} \frac{d}{dx}\left[A_{leg}\,\kappa_p(T_p)\frac{dT_p}{dx}\right] - \tau_p(T_p)\,I_e\,\frac{dT_p}{dx} + \frac{I_e^2}{A_{leg}\,\sigma_p(T_p)} = 0 \\ \frac{d}{dx}\left[A_{leg}\,\kappa_n(T_n)\frac{dT_n}{dx}\right] + \tau_n(T_n)\,I_e\,\frac{dT_n}{dx} + \frac{I_e^2}{A_{leg}\,\sigma_n(T_n)} = 0 \end{cases} \tag{2.6}$$

where the terms of the equation correspond, respectively, to transport of heat by conduction, generation (in p leg) and absorption (in n leg) of heat by Thomson effect and heat generation by Joule heating. Thermal and electrical conductivities, as well as Seebeck coefficients, can be found in the TEG datasheet (Appendix B.1).

Regarding heat exchanged at the boundaries (q_H at $x = -L$ and q_C at $x = L$), besides heat transferred by conduction, Peltier effect in the p-n junctions must also be considered:

$$\begin{cases} q_H/N = A_{leg}\left[-\kappa_p(T_H)\frac{dT_p}{dx}\big|_{x=-L} - \kappa_n(T_H)\frac{dT_n}{dx}\big|_{x=-L}\right] + I_e\,T_H\,\left[S_p(T_H) - S_n(T_H)\right] \\ q_C/N = A_{leg}\left[-\kappa_p(T_C)\frac{dT_p}{dx}\big|_{x=+L} - \kappa_n(T_C)\frac{dT_n}{dx}\big|_{x=+L}\right] + I_e\,T_C\,\left[S_p(T_C) - S_n(T_C)\right] \end{cases} \tag{2.7}$$

Once the temperature distribution in each leg is obtained, all the other properties can be determined. The voltage build up at the TEG terminals, U_{oc}, can be calculated with the equation

$$U_{oc} = N \int_{T_C}^{T_H} \left[S_p(T_p) - S_n(T_n)\right] dT \tag{2.8}$$

TEG internal electrical resistance, $R_{e,TEG}\,[\Omega]$, was calculated from the electrical properties of the legs and cables, that serve as TEG terminal connectors. For the TEG used, the cables are made of Aluminium (Al), have a diameter of 0.6 mm and a length of $L_{cable} = 11\,\mathrm{mm}$.

$$R_{e,TEG} = N \int_{-L}^{L} \left[\frac{1}{A_{leg}\,\sigma_p(T_p(x))} + \frac{1}{A_{leg}\,\sigma_n(T_n(x))}\right] dx + 2 \times \frac{L_{cable}}{A_{cable}\,\sigma_{\mathrm{Al}}} \tag{2.9}$$

Knowing the electrical resistance of the final circuit ($R_{e,TEG} + R_{e,load}$) and voltage drop created by the Seebeck effect, the current $I_e\,[\mathrm{A}]$ was deduced from the formula:

$$I_e = \frac{U_{oc}}{R_{e,TEG} + R_{e,load}} \tag{2.10}$$

The electrical power harvested, P_{TEG}, can finally be computed from the thermodynamic or from the electric circuit analogues (Figure 1.2). The value obtained should be equal but, depending on the degree of simplification and assumptions of the model, they can be approximated. In this work the electrical analogue was used for calculating P_{TEG} [W].

$$P_{TEG} = I_e^2 \, R_{e,load} \approx q_H - q_C \tag{2.11}$$

2.2 Finite volume method

Even though the full characterization of TEG electrical and thermal behavior is possible using Equations 2.8-2.11, those require knowledge of temperature distribution in each leg $T_p(x)$ and $T_n(x)$. For that, the energy balance in Equation 2.6 needs to be solved. In the literature, material properties (κ, σ, S) are often considered invariable with temperature to solve equations algebraically and, consequently, Thomson effect for heat generation/absorption is neglected [55, 56]. Using finite volume method it is however possible to have sufficiently accurate solutions for Equation 2.6. To do so, the domain was discretized in a uniform grid with a large number of elements (100 was found to be sufficient), each with Δx in width. For 1D domains, nodes from left and right adjacent elements are often identified with capital letters W (West) and E (East), as Figure 2.2 illustrates. Small letters w and e are used to denote the boundaries of the element.

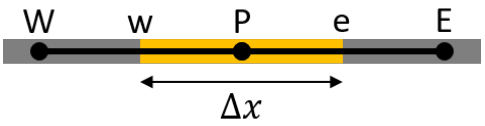

Figure 2.2: Elements nodes and boundaries nomenclature for a 1D grid, in finite volume method.

To evaluate the derivatives, a central difference differentiation scheme was used. To compute the derivative of a property ψ, for example, at the right boundary "e" or at the center of the element "P":

$$\frac{\partial \psi}{\partial x}\Big|_{x_e} = \frac{\psi_E - \psi_P}{x_E - x_P} = \frac{\psi_E - \psi_P}{\Delta x} \tag{2.12}$$

$$\frac{\partial \psi}{\partial x}\Big|_{x_P} = \frac{\psi_e - \psi_w}{x_e - x_w} = \frac{\frac{\psi_E + \psi_P}{2} - \frac{\psi_P + \psi_W}{2}}{\Delta x} = \frac{\psi_E - \psi_W}{2\Delta x} \tag{2.13}$$

The analogous for other nodes and boundaries follows the same reasoning.

That said, the governing equations in Equation 2.6 can now be discretized. The subscripts for p and n legs were omitted for sake of simplicity. The integration of the equation inside the element with boundaries x_w and x_e:

$$\int_{x_w}^{x_e} \left\{ \frac{d}{dx}\left[A_{leg}\, \kappa(T) \frac{dT}{dx} \right] \mp \tau(T)\, I_e \frac{dT}{dx} + \frac{I_e^2}{A_{leg}\, \sigma(T)} \right\} dx = 0 \tag{2.14}$$

leads, considering the differentiation scheme, to the discretized equation

$$A_{leg}\left[\kappa(T_e)\frac{T_E-T_P}{\Delta x}-\kappa(T_w)\frac{T_P-T_W}{\Delta x}\right]\mp\tau(T_P)\,I_e\,[T_e-T_w]+\frac{\Delta x\,I_e^2}{A_{leg}\,\sigma(T_P)}=0 \tag{2.15}$$

If the terms in the last equation are rearranged, one can obtain a non-linear expression only with the unknowns T_W, T_P, T_E and I_e. Nevertheless, it would be preferable the equation to be linearized, in order to be represented in a matrix form for all elements and to be solved efficiently. To tackle this, an iterative process was implemented, where the electrical current I_e and some of the temperatures (henceforth denoted T') were evaluated using the temperature distribution of the previous iteration. At each iteration they got successive corrections, until convergence was attained.

$$\frac{A_{leg}}{\Delta x}\left\{\kappa(T'_w)\,T_W-[\kappa(T'_w)+\kappa(T'_e)]\,T_P+\kappa(T'_e)T_E\right\}\mp\tau(T'_P)\,I_e\,\frac{1}{2}\,[T'_E-T'_W]+\frac{\Delta x\,I_e^2}{A_{leg}\,\sigma(T'_P)}=0 \tag{2.16}$$

When Equation 2.16 was solved for the first time, a linear temperature distribution between T_H and T_C (derived from boundary conditions) was assumed. This permitted an initial estimation of I_e (using Equations 2.8, 2.9 and 2.10), as well as the evaluation of different temperatures T'. A flowchart of the steps involved can be found in Appendix C.1.

For each element of the domain, the discretized Equation 2.16 can be written in the form

$$a_W\,T_W+a_P\,T_P+a_E\,T_E=b_P\,T_P+b_u \tag{2.17}$$

where the coefficients associated with heat transport (a_W, a_P and a_E) were included in a tridiagonal matrix $[a]$ and the heat source terms (b_u and b_P) in the vector $\{b\}$. The solution of temperatures for all element nodes of the domain was obtained from

$$[a]\,\{T\}=\{b\}\quad\Rightarrow\quad\{T\}=[a]^{-1}\,\{b\} \tag{2.18}$$

Convergence using this method is guaranteed if Scarborough criterion is verified [57].

For the elements in the interior of the domain, the final coefficients a and b are:

$$a_E=A_{leg}/\Delta x\times\kappa(T'_e) \tag{2.19}$$

$$a_W=A_{leg}/\Delta x\times\kappa(T'_w) \tag{2.20}$$

$$b_P=0 \tag{2.21}$$

$$a_P=a_E+a_W-b_P \tag{2.22}$$

$$b_u=\mp\tau(T'_P)\,I_e\,[T'_E-T'_W]\,/2 \tag{2.23}$$

These should be adjusted in the hot and cold boundaries of the domain using the BCs prescribed.

The stop criteria used for the iterative process was based in the relative difference of important quantities between consecutive iterations. If that value was below 10^{-4} for I_e, $R_{e,TEG}$ and temperatures at each node, then the iterative process stopped and the model returned the desired outputs.

2.3 Boundary conditions

Being a second order differential equation, Equation 2.6 needs two boundary conditions for each leg. The model can either work with two essential boundary conditions or one essential and one natural BCs. Those can be set manually or inferred from fuel composition and flame condition using a neural network.

If two essential BCs (T_C and T_H) were given, we assumed an initial linear temperature distribution and made successive corrections to it, in the iterative process. This encompasses the calculation of U_{oc}, $R_{e,TEG}$, I_e (Equations 2.8 - 2.10) and solving the energy balance for each leg with the finite volume method.

2.3.1 Handling natural BCs

If a natural and an essential BCs were given instead (fixed temperature and heat flux at the cold boundary, for example), then the process of determining the temperature distributions $T_p(x)$ and $T_n(x)$ involved the estimation the other essential boundary condition (T_H in this example).

Since the legs are thermally connected in parallel, there is no way to know, in the beginning, how much of the heat flux imposed flows through the p and n legs. A mean thermal conductivity at the cold boundary was firstly calculated

$$\overline{\kappa}(T_C) = \left[\kappa_p(T_C) + \kappa_n(T_C)\right]/2 \tag{2.24}$$

to be included in the following equation

$$-A_{leg}\,\overline{\kappa}(T_C)\,\frac{dT}{dx}\Big|_{x=L} \approx \frac{q_C}{2N} \;\Rightarrow\; \frac{T_H - T_C}{2L} \approx \frac{q_C}{2N}\,\frac{1}{A_{leg}\,\overline{\kappa}(T_C)} \tag{2.25}$$

which is an approximation of the heat rejected at the cold boundary, neglecting Peltier effect and considering a unique and invariable thermal conductivity in p and n legs, equal to $\overline{\kappa}(T_C)$.

Notice that the need for neglecting Peltier effect arises from the impossibility to determine any figure of I_e before knowing the temperature distribution. After using Equation 2.25 to foresee T_H, the initial linear temperature distribution was calculated and the process described for the case of two essential BCs follows.

At the end of each iteration the calculated heat flux at the boundary (Equation 2.7) was compared with the value imposed. A correction to T_H was made from the simple inference that: if the heat flux in the current iteration $q_{C,i}$ is underestimated, then T_H must increase (and vice-versa). If we neglect, again, the Peltier effect at the boundary (Equation 2.25), one can deduce that

$$\frac{dT_H}{dq_C} \approx \frac{L}{N}\,\frac{1}{\overline{\kappa}\,A_{leg}} \tag{2.26}$$

and, together with $T_{H,i}$ and the specified q_C, use this result to correct T_H and re-scale $T_p(x)$ and $T_n(x)$ for the next iteration $i+1$

$$T_{H,i+1} = T_{H,i} + \epsilon\,\frac{dT_H}{dq_C}\,\left[q_C - q_{C,i}\right] \tag{2.27}$$

The parameter ϵ can be interpreted as a under-relaxation factor. The approximation of neglecting Peltier

effect and the considerable amount of variables that were getting corrected in each iteration resulted in the loss of convergence in some situations. The value used, $\epsilon = 0.3$, led to a slower yet more robust convergence.

2.3.2 Neural network

The desire to endow the model with the capability to work with flame and fuel conditions as inputs, led to the use of a neural network (NN) to translate fuel and flame BCs to TEG BCs. This "translation" was built on experimental results and thus only works if aspects like water flowrate, TEG position with respect to burner, or even cooling water temperature close to 20 °C are maintained.

Due to the powerful interpolation capabilities and pattern recognition of neural networks, temperatures and heat fluxes can be predicted from any fuel and flame condition. Although some extrapolation capabilities are also expected, one should be careful and recognize its limitations based on the type of data used to train the NN. Correct inference of BCs is not expected, for example, in rich mixtures $\phi > 1$ (not tested) or for situations were it would not be possible to stabilize a flame.

The NN inputs were (i) equivalence ratio, (ii) burner Reynolds number and (iii) fuel composition; since the fuel used was a mixture of three gases, it was sufficient to give the molar fractions $\chi_{\mathrm{CO_2}}$ and $\chi_{\mathrm{H_2}}$ as input ($\chi_{\mathrm{CH_4}}$ is a function of the other two). The outputs of the NN are T_H, T_C and q_C. All these mentioned variables were measured for 142 different conditions and constitute the available data for training, validation and testing.

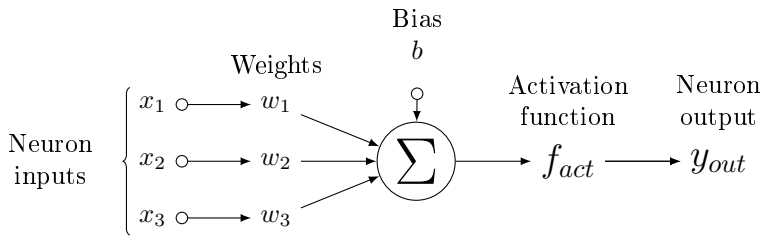

Figure 2.3: Inputs and output of each neuron.

Each neuron in the neural network accepts multiple inputs and has a single output, as Figure 2.3 shows. Those inputs are multiplied by weights and summed together. Besides the inputs and respective weights, a bias is usually included to allow for more degrees of freedom and, eventually, a better performance from the NN. The process of training the NN involved the adjustment of these weights and bias for all neurons, until a stop criterion was reached.

Associated with each neuron, there is an "activation function" (f_{act} in Figure 2.3) which has a direct impact in the training of the net. The hyperbolic tangent sigmoid function is one of the most common and was selected for all neurons in our net. Its derivative permits a relatively fast learning and its output is bounded between -1 and 1, promoting also a stable and smooth convergence. For the nomenclature of Figure 2.3 and activation function in question, the output of the neuron is:

$$y_{out} = f_{act}\left(x_1 w_1 + x_2 w_2 + x_3 w_3 + b\right) = \frac{2}{1 + \exp\left[-2 \times \left(x_1 w_1 + x_2 w_2 + x_3 w_3 + b\right)\right]} - 1 \tag{2.28}$$

A multilayer feed-forward neural network has multiple neurons organized by layers. As Figure 2.4 indicates, there are no connections between neurons within the same layer; connections are made between neurons of successive layers. Those can be of three types: input layer, output layer and hidden layers (can be more than one). The number of neurons in hidden layers should be adjusted, whilst the number of neurons in input and output layers is predetermined by the number of inputs and outputs of the NN.

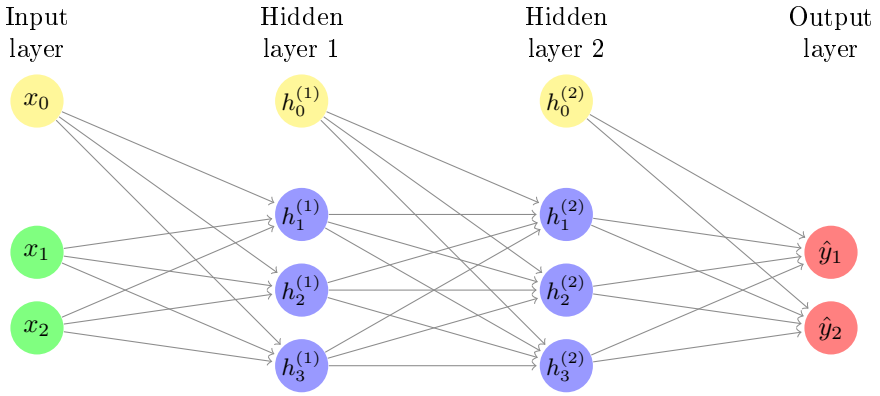

Figure 2.4: Structure of a multilayer feed-forward neural network with two inputs (x_1, x_2), two outputs ($\hat{y}_1$, $\hat{y}_2$) and two hidden layers with three neurons each; sketch of connections between neurons, where x_0, $h_0^{(1)}$ and $h_0^{(2)}$ correspond to bias values.

The algorithm chosen to train the net was the back-propagation with Bayesian regularization and, for the error function, the mean squared error was selected. Back-propagation calculates the Jacobian of the error function with respect to each weight and bias, for the chosen activation function. From the difference between target (what we wanted the NN to return) and output (what it returned), the error "back-propagates" from output layer to input layer, making adjustments in weights and biases, based on the sensitivity of them to the output error [58]. This progressively took the NN error to a local minima. If Bayesian regularization was not included, the portion of the data allocated to validation would be used as stopping criteria: if the error for validation data kept increasing in successive iterations, then the NN was over-fitting the training data.

For an under-fitted NN, the source of error is associated with bias; for over-fitting, it is related with variance instead. Making use of conditional probability [59, 60], a Bayesian NN can distinguish the nature of the training error and act on the basis of Occam's razor, automatically and optimally penalizing excessively complex models [61]. Therefore, there was no need to assign part of available data for validation. This training algorithm is useful for cases where the amount of data is relatively small, like the present one.

The data was hence split in 75% for training and 25% for testing (independent data reserved to evaluate performance of the NN at the end). The structure of the neural network (number of hidden layers and neurons in each of them) was optimized based on the testing mean squared error and fixed in: 4 neurons for a first hidden layer and 6 neurons for a second one. Results of performance for the final NN, used in the model, can be found in Appendix C.2.

Chapter 3

Experimental

3.1 Equipment and setup

Throughout the experimental work, different setups were assembled depending on the type of analysis. Three major types of analysis can be distinguished: (i) power and temperature acquisitions, (ii) particle image velocimetry (PIV) for perceiving flow velocity field, and (iii) chemiluminescence setup for analyzing flame structure, quenching distances and heat release rate.

(a) (b)

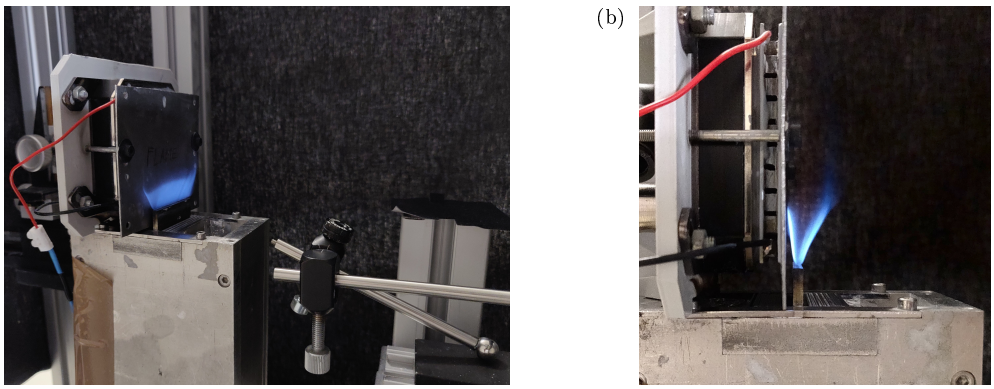

Figure 3.1: Experimental setup (a) perspective and (b) front views.

The laminar premixed flame stabilizes on a lamella burner with a stainless steel flame holder (Figure 3.1), acquiring a 2D V-shape in most of its width. It has two slits with dimensions 40×2mm ($l \times w$) each, from where unburnt gases are supplied. Side-Wall Quenching (SWQ) occurs as one of the sides of the flame approaches the surface of an Aluminium (Al) plate ($90 \times 75 \times 1$mm). The Al plate, henceforth designated by wall, is positioned 2 mm apart from the flame holder. In that position, the flame is less prone to resonate. The wall is also as close as possible (1.5 mm) to the burner, preventing the unburnt mixture from escaping underneath. These positions were maintained for all the conditions (Figure 3.2).

A thermoelectric generator (TEG) is placed between the wall and a CPU-adapted heat exchanger (HX) (Phanteks Glacier C350i). The wall protects the hot surface of the thermoelectric from direct contact with the flame, while the heat exchanger serves as the system heat sink. Table 3.1 contains information about the GM200-49-45-30 (European Thermodynamics) TEG module used. Its datasheet can be found

Table 3.1: GM200-49-45-30 thermoelectric general characteristics.

Dimensions	$62 \times 62 \times 5.8$mm	
Maximum temperature:	$T_{H,max} = 473\,\mathrm{K}$	$T_{C,max} = 448\,\mathrm{K}$
Performance for:	$T_H = 473\,\mathrm{K}$,	$T_C = 303\,\mathrm{K}$
Matched load output power	$7.5\,\mathrm{W}$	
Matched load resistance	$0.28\,\Omega \pm 15\%$	
Open circuit voltage	$2.8\,\mathrm{V}$	
Heat flow through module	$\sim 149\,\mathrm{W}$	

in Appendix B.1. As Figure 3.2a shows, the TEG is placed above the flame holder height, to be in contact with the hottest region of the wall. To diminish the thermal contact resistances between wall, TEG and HX, a thermal paste (AG Termopasty HPX) with a thermal conductivity of $2.8\,\mathrm{W/(K\,m)}$ was used; its dielectric constant of 5.1 ensures it does not affect the thermocouples readings. The mentioned components are fixed with bolts to a 3D printed piece (Figure 3.2b), facilitating its change between different setups.

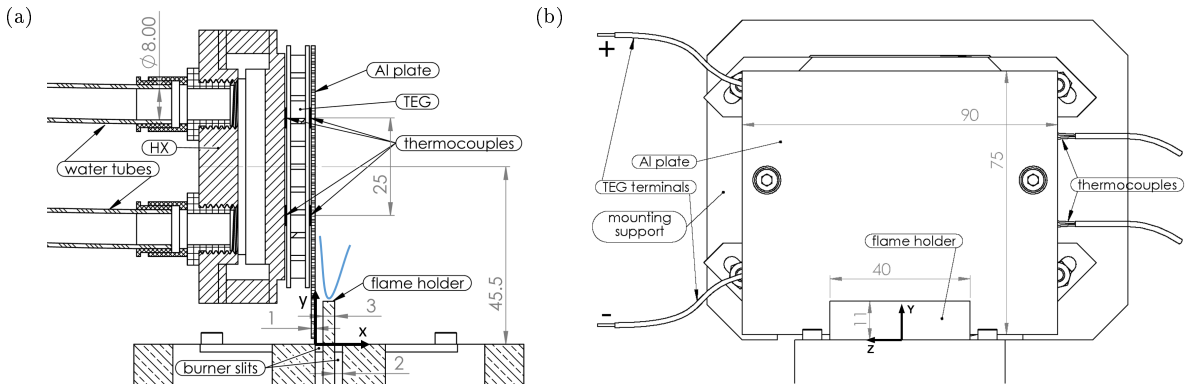

Figure 3.2: Details and dimensions of burner, TEG and Al plate (units in mm), with (a) front and (b) side views; XYZ cartesian coordinate system considered for experimental results.

Tap water is supplied through a tube connected to the bottom of the heat exchanger. The water exits in the same manner, from the top of the HX, after passing through a series of fins. For a water flow of 1.619 LPM[1], it has an estimate head loss of 0.945 m of water, based on experimental tests.

Six OMEGA *K-type* thermocouples and a DataTranslation DT9828 acquisition board were used to monitor system temperatures: four of the thermocouples are placed in the hot and cold sides of the TEG (two on each side), 25 mm apart in the y direction (Figure 3.2a) and at $z = 0$ plane. The other two thermocouples are inserted in small holes drilled in the water tubes, right before (after) the inlet (outlet) of the HX. The acquisition board is connected to a computer, where data is visualized and exported using QuickDAQ software.

The TEG terminals are connected to an electric load, composed of ceramic resistances. Their use is justified by the improved closed circuit voltage (U_{cc}) stability in steady state operation, noticed in preliminary tests. With the help of the mathematical model and temperature readings in hot and cold sides, a range of expected TEG internal electrical resistance, $R_{e,TEG}$, was determined. The electric load

[1] liters per minute

was dimensioned to have a resistance always above TEG's matched one, *i.e.* $R_{e,load} > R_{e,TEG}$. This ensures that we are working always beyond the maximum power point (see power curve of Figure 1.3a) and, consequently, that the variation of power with the heat across the TEG is monotonic. It diminishes the complexity of variables, avoiding erroneous reasoning and inferences from obtained measurements. The final measured resistance value was $R_{e,load} = 0.281\,\Omega$.

The closed circuit voltage U_{cc} was also monitored, using the same acquisition board and software described for the thermocouples. Since the TEG can reach, for the maximum temperature difference, an open circuit voltage U_{oc} close to 3 V, the acquisition board analog inputs (which can only handle voltages up to 312 mV) were connected in parallel with TEG's electric load using a voltage divider circuit. Figure 3.3 contains a scheme of the electrical circuit used. The measured voltage in the acquisition board, denoted U_m, is nearly 10 times smaller than U_{cc}.

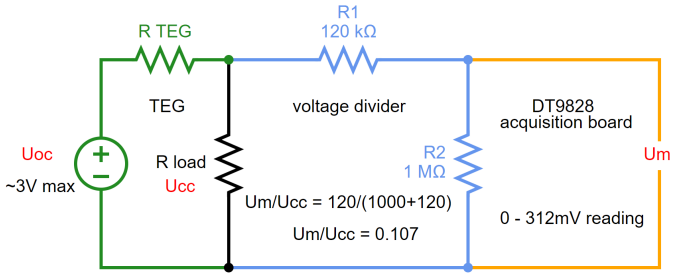

Figure 3.3: Electric circuit; from left to right: TEG electrical equivalent, voltage divider circuit, DT9828 acquisition board.

The different flame conditions are obtained using four Alicat Scientific M-series gas flow meters, one for each gas. After being dried and filtered, air passes through a flow meter with a capacity of 50 SLPM[2]. CH_4 and H_2 are drawn from gas bottles (Air Liquid Alphagaz 99.95%). Their flow meters have a maximum capacity of 5 SLPM and 1 SLPM respectively. Finally, CO_2, also drawn from a gas bottle (Air Liquid Alphagaz 99.95%), can have a maximum flow rate of 5 SLPM. The mixture is blended in a small chamber, which then connects to the burner using a single tube. The water flow rate in the HX is controlled using an Alicat Scientific LCR flow meter with 2 LPM capacity.

PIV - particle image velocimetry

Aluminium oxide (Al_2O_3) particles were used as tracers for their inertness and high melting point, which are needed when studying combustion reactive flows. Their diameter of 1 µm and density of 3950 kg/m^3 led to an estimate Stokes number in the order of 10^{-4}, which is below the maximum advised value of 0.1 [62] (hence having a sufficient response time for the flow characteristics). The Al_2O_3 particles are seeded from a flask using a magnetic stirrer, whose frequency was adjusted to obtain the desired particle density.

An ANDOR Zyla 5.5 sCMOS camera, combined with a Nikon AF Nikor 60mm f/2.8D lenses, was used to capture particle images (Figure 3.4). The camera, with 5.5MP, is capable of double-frame acquisitions at 15 Hz and has a quantum efficiency of 55% for the laser wavelength. The area of study was chosen to include the flame holder, the flame itself, and a portion of the region upstream the flame, to understand

[2]standard liters per minute

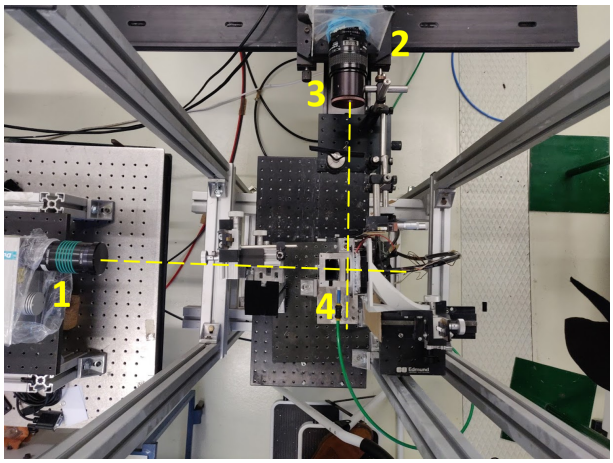

Figure 3.4: Top view of PIV experimental setup, showing (1) laser, (2) camera and lens, (3) 532 nm optical filter, and (4) main setup shown in Figure 3.1.

how the hot gases would interact with the wall. The spatial resolution was not a determining variable and was rather constrained by the described area of interest.

The Dantec DualPower 65-15 Nd:YAG laser was used to illuminate the Al_2O_3 particles. It has four energy levels, a 532 nm (1064 nm fundamental) beam wavelength, which lasts for 4 ns, and a maximum output energy of 400 mJ. The common coherence lengths for this type of laser ranges from 1m to 2m. The laser sheet intensity profile is Gaussian distributed to avoid complete black-out of particles with velocity component perpendicular to laser sheet plane.

Whenever acquisitions with a flame were performed, a 532 nm CVI Melles Griot light filter (3 nm bandwidth) was used. It is transparent only to the scattered light from particles (enabling the correct correlation between frames) and blocks out the intense light emitted by the flame in other wavelengths, that would damage the sensitive camera CMOS with the large aperture used on the lens.

Finally, the laser and camera were connected to a synchronizer (BNC Model 575). The camera configuration and its acquisitions were processed in a computer with the Dantec DynamicStudio v5.1 [63] software.

Chemiluminescence

In this setup, the same camera, synchronizer and software described for the PIV were used. Figure 3.5 shows the required equipment for the analysis. To capture the radicals chemiluminescence, a Coastal Optics 105mm f/4.5 UV-Micro-APO camera lens, which is permeable to the UV light, was used. An image intensifier (Hamamatsu C9547-03L3) was placed between lens and camera. It uses a Multialkali photocathode, has a spectral response from 185 nm to 900 nm and a radiant emittance gain up to 6.2×10^3 (for the wavelength of maximum response). The gain of the intensifier is adjustable through an analogic potentiometer.

Finally, a support for the different filters is placed after the lens, to block out the majority of surrounding light. Two optical filters are used to monitor chemiluminescence from OH radical with peak emission at 309 nm (Andover *310FS10-50*, $\tau_{max} = 17.40\%$, $\bar{\lambda} = 311.142$ nm) and CH radical with peak

emission at 431 nm (Andover *430FS10-50*, $\tau_{max} = 50.76\%$, $\bar{\lambda} = 430.850\,\text{nm}$). The chemically excited radicals are henceforth denoted OH* and CH*, respectively.

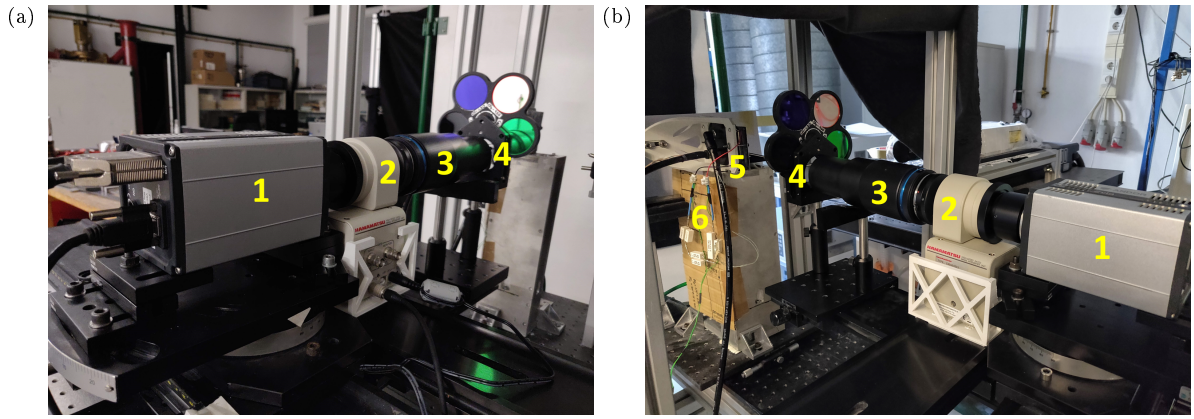

Figure 3.5: Chemiluminescence experimental setup with (1) camera, (2) image intensifier, (3) camera lens, (4) optical filters, (5) main setup and (6) respective electric circuit.

3.2 Methodologies

The flow meters set points were defined through a in-house designed LabView software, that allowed to compute each gas flow rate directly from fuel composition, Reynolds number (Re) and mixture equivalence ratio (ϕ) conditions.

Table 3.2: Overview of fuel blends and operating conditions tested.

Reynolds number, Re	100, 150, ..., 300, 350
Equivalence ratio, ϕ	0.7, 0.8, 0.9, 1.0
Base fuels H_2 dope	BG100, BG80, BG60 0%, 10%, 20%
Min flame power, $P_{flm,min}$ Max flame power, $P_{flm,max}$	$\sim 263\,\text{W}$ $\sim 1387\,\text{W}$
Water flow rate in the HX, $\dot{V}_{H_2O}$	1.25 LPM

For the experiments, several fuels, flame conditions and hydrogen concentrations were used (Table 3.2). Biogas mixtures were simulated with a blend of $CH_4 + CO_2$, since these gases account for more than 95% of the composition of BG produced by anaerobic digestion [18, 19]. Pure methane (BG100) and two types of biogas fuels were used: one with 80% of CH_4 and 20% of CO_2, designated BG80, and another with 60% of CH_4 and 40% of CO_2 (BG60). The number after "BG" indicates therefore the amount of CH_4 in the biogas. 10% and 20% of H_2 (volume percentage) was added to BG60 and BG80 biogas blends.

For a mixture termed BG **X** **Y**%H_2, the molar fraction χ of each specie can be calculated through:

$$\chi_{H_2} = \mathbf{Y}/100 \tag{3.1}$$

$$\chi_{CH_4} = \mathbf{X}\,(1 - \chi_{H_2}) \tag{3.2}$$

$$\chi_{CO_2} = 1 - \chi_{H_2} - \chi_{CH_4} \tag{3.3}$$

The Reynolds numbers tested range from 100 to 350. In the lower limit the flame is small and close to flashback. In the upper limit the flame tips are prone to resonate. The equivalence ratios were chosen to have three lean and one stoichiometric flame conditions (see Table 3.2). When monitoring the TEG cold side temperature, T_C, and the power yielded P_{TEG}, it was possible to conclude that only if the water flow rate $\dot{V}_{\mathrm{H_2O}} \leq 0.8\,\mathrm{LPM}$, the performance would start to decrease. From that point on, P_{TEG} remained constant until the flow meter maximum capacity. The water flow rate was therefore fixed in $\dot{V}_{\mathrm{H_2O}} = 1.25\,\mathrm{LPM}$ to reduce the number of variables.

The burner Reynolds number is defined with a characteristic length equal to the burner slit width $w = 2\,\mathrm{mm}$, and described by the equation:

$$Re = \frac{V \times w}{\nu_u} = \frac{[\dot{V}_u/(w \times l)] \times w}{\nu_u} = \frac{\dot{V}_u}{l \times \nu_u} \tag{3.4}$$

where $\dot{V}_u[\mathrm{m^3/s}]$ is the unburnt mixture volumetric flow rate, $\nu_u[\mathrm{m^2/s}]$ represents the mixture kinematic viscosity and $l = 40\,\mathrm{mm}$ is the burner slit length. $V_u[\mathrm{m/s}]$ is the mean velocity of the gases at the slit exit.

The unburnt gases exiting the burner were assumed to be at room temperature $T_u = 298.15\,\mathrm{K}$ and at atmospheric pressure. The volumetric flow rate at standard conditions for temperature and pressure (STP conditions), used in flow meters, was calculated using the ideal gas law $p = \rho_u R_0 T$. The flame power P_{flm} was calculated from the fuel low heating value (LHV[J/kg]), fuel mass fraction (Y_F) and unburnt mixture density ($\rho_u[\mathrm{kg/m^3}]$):

$$P_{flm} = LHV \times Y_F \times \rho_u \times \dot{V}_u \tag{3.5}$$

The Cantera [64] Python module was used to calculate different mixture properties. Whenever calculating dynamic viscosity, thermal conductivity or other transport quantity, the GRI-Mech3.0 [65] mechanism was used, taking into consideration the transport properties of each species individually.

Uncertainties

At the end of each methodologies sub-chapter, an uncertainty analysis is carried out for measurements and variables involved. When the uncertainty of any result with expected value a is presented as $a \pm u_{95\%}$, that corresponds to the upper and lower bounds of the 95% confidence interval. If the uncertainty is presented as a percentage $a \pm u_r\%$, it refers to the relative uncertainty, calculated from:

$$u_r = \frac{u_{95\%}}{a} \times 100 \tag{3.6}$$

Guidelines advised from Abernethy *et al.* [66] about quantifying uncertainties were followed. For particular cases other reference documents were also used [67]. For most cases, populations of measurements were assumed normal distributed.

The flow meters error depend on their capacity and setpoint. The air flow meter precision is defined with ±0.8% of setpoint plus ±0.2% of capacity values. For CH_4, CO_2 and H_2 flow meters, uncertainty is

equal to ±0.6% of setpoint or ±0.1% of capacity, whichever is greater. Precision values can be assumed to be in a 99% confidence interval, and thus correspond, in a normal distribution, to the interval between $[-3u_\sigma, 3u_\sigma]$. Standard deviations for flowrates $u_\sigma(\dot{V})$ can then be computed. For the chosen water flow rate, its flow meter has an uncertainty of $u_{95\%}(\dot{V}_{\mathrm{H_2O}}) = 0.046\,\mathrm{LPM}$.

Flow meters uncertainties have a direct impact in ϕ, Re and P_{flm}. The equivalence ratio ϕ can be expressed as:

$$\phi = \frac{\mathrm{AFR}_{stoich}}{\mathrm{AFR}} = \frac{[n_{air}/n_{fuel}]_{stoich}}{n_{air}/n_{fuel}} = \frac{n_{stoich}\,\dot{V}_{fuel}}{\chi^{air}_{\mathrm{O_2}}\,\dot{V}_{air}} \tag{3.7}$$

where n_{stoich} is the number of mols of air (n_{air}) required to oxidate one mol of fuel (n_{fuel}) in stoichiometric proportion

$$n_{stoich} = 2\,\chi_{\mathrm{CH_4}} + \frac{\chi_{\mathrm{H_2}}}{2}\,, \tag{3.8}$$

and $\chi^{air}_{\mathrm{O_2}} = 0.21$ is the volume fraction of oxygen in dry air used. Taking into account that $\dot{V}_{fuel} = \dot{V}_{\mathrm{CH_4}} + \dot{V}_{\mathrm{CO_2}} + \dot{V}_{\mathrm{H_2}}$, the standard deviation of the equivalence ratio $u_\sigma(\phi)$ is hence calculated from:

$$u^2_\sigma(\phi) = \sum_{i=1}^{3} \left\{ \left[\frac{\partial\phi}{\partial\dot{V}_{fuel,\,i}}\right]^2 \times u^2_\sigma(\dot{V}_{fuel,\,i}) \right\} + \left[\frac{\partial\phi}{\partial\dot{V}_{air}}\right]^2 \times u^2_\sigma(\dot{V}_{air}) \tag{3.9}$$

where i corresponds to each species present in the fuel. The partial derivatives can be evaluated from Equation 3.7.

As for the Reynolds number, Equation 3.4 allow us to infer that its variance is:

$$u^2_\sigma(Re) = \left(\frac{1}{l \times \nu_u}\right)^2 \times \sum_{i=1}^{4} u^2_\sigma(\dot{V}_{u,\,i}) \tag{3.10}$$

In this case, index i represents each gas specie in unburnt mixture (fuels and air). No uncertainties in geometry measurements were considered.

Lastly, for flame power (defined in Equation 3.5), we have:

$$u^2_\sigma(P_{flm}) = \left[\rho_{\mathrm{CH_4}} \times LHV_{\mathrm{CH_4}}\right]^2 \times u^2_\sigma(\dot{V}_{\mathrm{CH_4}}) + \left[\rho_{\mathrm{H_2}} \times LHV_{\mathrm{H_2}}\right]^2 \times u^2_\sigma(\dot{V}_{\mathrm{H_2}}) \tag{3.11}$$

Table 3.3: Uncertainties of gases and water flow rate and their propagation to equivalence ratio, Reynolds and flame power; average and maximum errors are calculated based on all conditions tested.

			$u_{95\%}$		u_r	
			avg	max	avg	max
Flame Condition and Water Flow Rate	$\dot{V}_{air}$	[SLPM]	0.140	0.188	1.11%	1.70%
	$\dot{V}_{\mathrm{CH_4}}$	[SLPM]	5.0×10^{-3}	9.3×10^{-3}	0.45%	0.83%
	$\dot{V}_{\mathrm{CO_2}}$	[SLPM]	3.0×10^{-3}	5.3×10^{-3}	0.84%	3.09%
	$\dot{V}_{\mathrm{H_2}}$	[SLPM]	0.7×10^{-3}	3.2×10^{-3}	0.26%	1.07%
	Re		4.065	5.395	1.97%	2.93%
	ϕ		0.010	0.021	1.21%	2.12%
	P_{flm}	[W]	2.976	5.547	0.43%	0.75%
	$\dot{V}_{\mathrm{H_2O}}$	[LPM]	0.046	0.046	3.70%	3.70%

The error standard deviation of each variable was computed for each flame condition and fuel composition used. With those, the 95% confidence interval and respective relative error could be determined. Their average and maximum values are presented in Table 3.3.

3.2.1 Power and temperature measurements

Since $R_{e,TEG}$ is small, the use of any multimeter to directly read the current is impractical: the electric resistance of the multimeter itself is of the same order of the TEG one. A different method, based on the precise determination of $R_{e,load}$ and measurement of closed circuit voltage U_{cc}, had to be employed to overcome this problem. The load resistance terminals were connected to a current generator to ensure that the load would maintain a stable and constant resistance over time, for different currents. This allowed at the same time the precise measurement of $R_{e,load}$. P_{TEG}[W] can now be estimated from the closed circuit voltage drop U_{cc}[V] and $R_{e,load}$[Ω], using the formula:

$$P_{TEG} = U_{cc} \times I_e = U_{cc} \times \frac{U_{cc}}{R_{e,load}} = \frac{U_{cc}^2}{R_{e,load}} \tag{3.12}$$

where I_e[A] is the current flowing through the resistance. This same method is used by other authors to evaluate the electric output of the TEG [15, 56, 68].

In the computer, the analog input channels of the acquisition board were configured for the *K-type* thermocouples and for the characteristics of the voltage divider circuit (proportional relation between U_m and U_{cc} - see Figure 3.3), enabling the direct and continuous monitoring of power and temperature. The acquisitions lasted 3 min each, with a 5 min interval between them to ensure steady state condition was attained.

To estimate the heat rejected from the TEG in the cold side (q_C[W]), it was assumed as simplification that all heat was absorbed by the water in the HX, increasing its temperature from $T_{\mathrm{H_2O},in}$ to $T_{\mathrm{H_2O},out}$. That said, a simple energy balance between HX inlet and outlet returned the desired heat rejected:

$$q_C \approx \dot{m}_{\mathrm{H_2O}} \times c_{\mathrm{H_2O}} \times (T_{\mathrm{H_2O},out} - T_{\mathrm{H_2O},in}) \tag{3.13}$$

where $\dot{m}_{\mathrm{H_2O}}$ [kg/s] $= \dot{V}_{\mathrm{H_2O}}$ [LPM] $\times \rho_{\mathrm{H_2O}}$[kg/m^3]$/(1000 \times 60)$ denotes the water mass flow rate and $c_{\mathrm{H_2O}}$ the water specific heat, assumed to be constant and equal to 4180 J/(kg K) [5].

Uncertainties

The measurement of temperature and voltage in the acquisition board are also subjected to a reading precision. For temperature, the 95% confidence interval corresponds to ±0.18 °C (based on datasheet information). As for measuring U_m, there is a bias error of $u_b(U_m) = \pm 20\,\mu$V and a precision of ±0.03%.

To quantify the uncertainty of U_{cc} measurement, linear fit tools allowed to estimate the error associated to the load resistance value ($U_{cc} = R_{e,load}\, I_e$) and the relation between U_m and U_{cc} by a constant g ($U_{cc} = g\, U_m$).

The variance and bias associated with the measurement of closed circuit voltage:

$$u_\sigma^2(U_{cc}) = [U_m \times u_\sigma(g)]^2 + [g \times u_\sigma(U_m)]^2 \tag{3.14}$$

$$u_b(U_{cc}) = g \times u_b(U_m) \tag{3.15}$$

are used, together with the standard deviation of U_{cc} during the 3 min acquisition (associated with TEG operation and denoted $u_\sigma(U_{cc,TEG})$ in the next equation), to calculate the uncertainty of closed circuit voltage

$$u_{95\%}(U_{cc}) = \sqrt{u_b^2(U_{cc}) + k^2\left[u_\sigma^2(U_{cc}) + u_\sigma^2(U_{cc,TEG})\right]} \tag{3.16}$$

where k=2 to obtain the 95% interval.

Looking at Equation 3.12, the uncertainty for power yielded, which depends on the uncertainty of close circuit voltage and load resistance, can be determined with:

$$u_\sigma^2(P_{TEG}) = \left[\frac{\partial P_{TEG}}{\partial U_{cc}} \times \sqrt{u_\sigma^2(U_{cc}) + u_\sigma^2(U_{cc,TEG})}\right]^2 + \left[\frac{\partial P_{TEG}}{\partial R_{e,load}} \times u_\sigma(R_{e,load})\right]^2 \tag{3.17}$$

$$u_b(P_{TEG}) = \frac{\partial P_{TEG}}{\partial U_{cc}}\, u_b(U_{cc}) = \frac{2U_{cc}}{R_{e,load}}\, u_b(U_{cc}) \tag{3.18}$$

$$u_{95\%}(P_{TEG}) = \sqrt{u_b^2(P_{TEG}) + k^2 u_\sigma^2(P_{TEG})} \tag{3.19}$$

The equations presented were applied to the results from all conditions tested and allowed to calculate the uncertainty of each variable. Those are presented in Table 3.4. The maximum relative error shown for temperature is for 18 °C (the lowest temperature registered).

Table 3.4: Statistical errors when measuring TEG power and temperature related variables; average and maximum values are based on the errors for each flame and fuel condition tested.

			$u_{95\%}$		u_r	
			avg	max	avg	max
Power and Temperature	$R_{e,load}$	[Ω]	9.4×10^{-4}	9.4×10^{-4}	0.34%	0.34%
	U_{cc}	[V]	13.4×10^{-3}	49×10^{-3}	1.51%	4.89%
	P_{TEG}	[W]	0.091	0.352	3.10%	9.81%
	Temperature	[°C]	-	0.18	-	0.95%

3.2.2 Flow field

The camera lens was used with the aperture set to its maximum ($f/2.8$). This permitted to capture sufficient light from particles, have a shallow depth of field and use small exposure times (avoiding the blur of particles). In order to diminish the optical aberrations over the field of view of the camera, the focus plane was set away from the minimal focal length. It was found that the resolution of 33.2 pix/mm (res = 30.12 µm/pix), with a magnification factor of M = 4.607, was adequate to capture the flow in detail and avoid pixel locking (particle Airy disk diameter D_{Airy} smaller than a single pixel), which introduces large uncertainties. The region of study took an area with 25 mm width and 50 mm height.

This led to a small characteristic time scale: for some flame conditions, it would take 1/60s for a particle to travel across the mentioned region of interest. Therefore, the temporal resolution was set to be the smallest possible - 15 Hz.

As the laser pulses, several parts from the main assembly (burner, plates, flame holder, screw bolts) reflect a good portion of light. Edmund Optics light absorbing black-out material was placed as close as possible from the focus plane to black-out those reflections. Despite the drawback of losing detail in the material edges regions due to light diffraction, it allowed to use higher laser intensity, which turned out essential for more particle brightness and less uncertain results. The two bolts used for fixation were painted black-matte, all the setup was covered with a black thick fabric and all acquisitions were carried out absent from ambient light.

Prior to all acquisitions, an alignment calibration was carried out to ensure that the camera was perpendicular to the laser sheet. An object with a textured surface was firstly placed coincident with the laser plane (Figure 3.6a); after turning the laser off, the object was captured by the camera; by making small focus and rotation adjustments, the camera was progressively taken into its aligned position, in which the textured surface was perfectly focused both on the left and right ends of the image (Figure 3.6b).

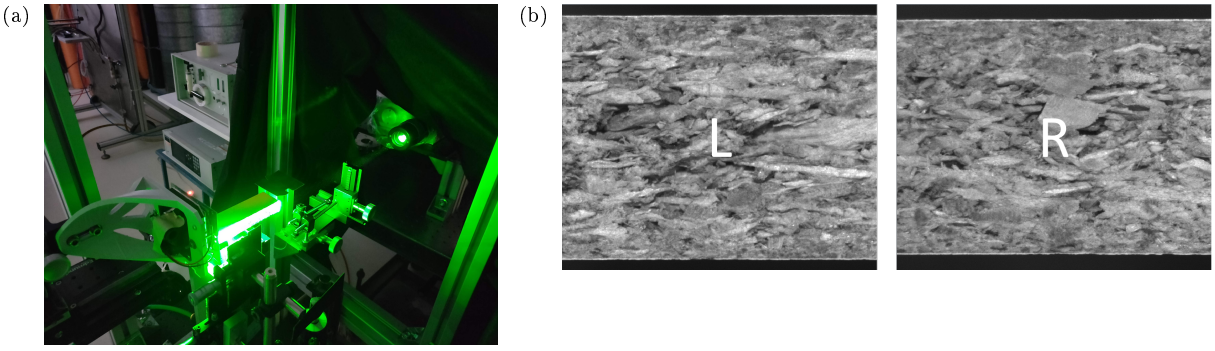

Figure 3.6: Calibration for PIV camera and laser orthogonality; (a) the object surface was made coincident with laser sheet and (b) the left and right ends of the object surface (coincident with the laser plane) were both focused.

Since the flow is studied in an Eulerian description, it is fundamental to define interrogation areas. Each of them will have an associated vector related with the particle movements, according to the strength of each correlation. Double frame acquisition and single exposure were used, which preserves the temporal order of the particle images *i.e.*, the velocity vector direction is unique and unambiguous.

The interrogation area size $[\mathrm{IA}_x, \mathrm{IA}_y]$ [pix], velocity vector $\vec{V}$[m/s], image resolution (res[m/pix]) and overlap percentage between interrogation areas $[o_{\mathrm{IA},x}, o_{\mathrm{IA},y}]$ dictate the required time interval between frames Δt[s]

$$\Delta t < \min\left(\frac{[\mathrm{IA}_x, \mathrm{IA}_y] \times (1 - [o_{\mathrm{IA},x}, o_{\mathrm{IA},y}])}{[V_x, V_y] \times res}\right) \tag{3.20}$$

for the particles movement not to be lost between frames. Δt should then be the minimum of the two possible values that result from the piece-wise multiplication and division of the vectors $\vec{\mathrm{IA}}$, $o\vec{_{\mathrm{IA}}}$ and $\vec{V}$. As Figure 3.7a illustrates, when particle displacements are smaller than a bounding region (constrained by Equation 3.20) inside the IA, it is guaranteed their movement is not lost between frames.

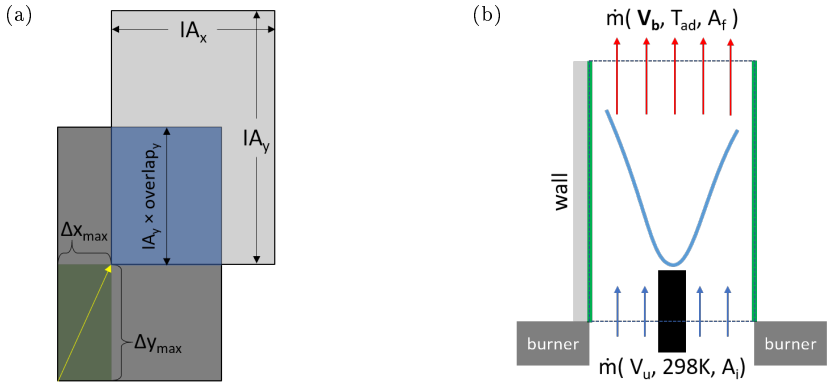

Figure 3.7: PIV methodologies to estimate the required time interval between frames Δt; (a) particle displacements smaller than the region defined by $\Delta x_{max} \times \Delta y_{max}$ in the IA ensure particles are detected between frames; (b) to predict $V_{y,max}$, burnt gases are assumed to reach T_{ad} in a confined control volume.

A IA size was firstly defined. Since the vertical component of velocity was expected to be much higher compared to the horizontal one, the calculation of Δt was done for a desired interrogation area of size $[\mathrm{IA}_x, \mathrm{IA}_y] = [16, 32]$. The interrogation areas overlap was set to $o_{IA} = 50\%$ both in x and y directions, for increasing vector density and reducing processing time [69].

Finally, the maximum V_y velocity possible was predicted considering a mass balance in a control volume, in which burnt gases were not allowed to expand in x direction and would reach the adiabatic flame temperature (Figure 3.7b). The burnt gases velocity is given by:

$$V_b = V_u \times \frac{\rho_u}{\rho_b} \times \frac{A_i}{A_f} \tag{3.21}$$

Since the IA size and IA overlap were fixed in Equation 3.20, different values of V_b translated into different Δt. The time between frames was chosen to be 50 µs, 75 µs or 100 µs, whichever was closer to the value of Δt calculated for each condition.

Figure 3.8 is an example (for $Re = 250$ in isothermal conditions *i.e.* without flame) of pre-processing of images, prior to the cross-correlation between frames. The Figure shows how three steps helped to obtain more particle contrast and hence more and better correlations. After that, and because the flow is statistically steady, an average correlation was employed to analyze the 200 pairs of frames acquired during 13.3 s, producing a unique vector field. For each interrogation area, velocity is calculated from a final correlation map, which is the weighted average of the 200 individual cross-correlation maps. This process automatically despises weak correlations (that may arise from insufficient particle density in some frames) and sporadic erroneous correlations (that are not consistent throughout the frame pairs).

Preliminary tests were conducted in isothermal conditions, both with and without the wall, in two different z coordinates. Those intended to confirm that the flow could be, in fact, described as two dimensional. The obtained results validated the methodology described so far and, as can be observed on Figure 3.9, verified that the velocity profiles do not change considerably along z coordinate. Taking

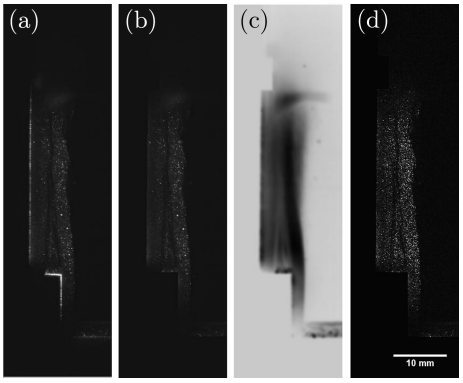

Figure 3.8: PIV pre-processing of (a) raw image involved: (b) the black-out of regions not to analyze, (c) filter applied to minimize unbalanced brightness and correct light sheet non-uniformity, and (d) top-hat Gaussian filter to enhance and homogenize particles contrast.

these into account it is possible to assume that, in the plane of study:

$$\frac{\partial \vec{V}}{\partial z}\Big|_{z=0} \approx 0 \tag{3.22}$$

$$\vec{V}\Big|_{z=0} \approx [V_x, V_y, 0] \tag{3.23}$$

After the velocity maps were obtained, two tools from Dynamic Studio [63] to remove spurious vectors were used. Those are based on V_x and V_y scatter plots and spacial coherence of vectors.

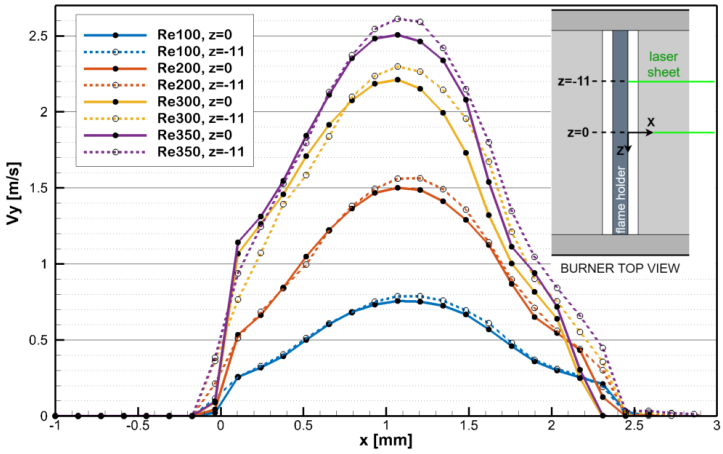

Figure 3.9: PIV isothermal tests: vertical velocity (V_y) profiles measured at $y = 2\,\text{mm}$ for two different z planes, without the wall; burner top view (inset).

Uncertainties

To evaluate correlation uncertainty in PIV analysis, a tool based on the quantification of signal-to-noise ratio was adopted. It uses a method [70] which deduces a radial velocity error from the ratio between the highest and second highest correlation peaks in each interrogation area. The error increases if the peak ratio decreases or if the peaks are located farther away. The tool is applied to raw vector maps, before any vector validation or post-processing.

All the velocity vectors absolute and relative errors were analyzed, for all interrogation areas of the

frames, in an histogram with 150 bins. From those, the most expected value (E_p) correspond to the bin with most occurrences. The 95% percentile allowed to compute $u_{95\%}$ and u_r. The results are presented in Table 3.5.

Table 3.5: Velocity radial uncertainty for the four flame conditions tested with BG100; the expected value E_p and the 95% percentile values are taken from the histograms with the absolute and relative error of all interrogation areas.

		V [m/s]	abs. error [mm/s]		rel. error	
Re	ϕ	E_p	E_p	$u_{95\%}$	E	u_r
200	0.7	2.16	14	34	2.24%	5.49%
200	0.8	2.18	70	172	2.16%	5.29%
300	0.7	3.03	103	252	2.18%	5.34%
300	0.9	3.13	105	257	2.23%	5.46%

The pixel resolution does not have a significant impact in the PIV uncertainty. To prove it, the diameter D_{Airy}, produced from small particles Mie scattering, can be calculated from M, aperture $f/$ and the laser light wavelength [62]:

$$D_{Airy} = 2.44\, f/ \times (M+1)\, \lambda \tag{3.24}$$

The Al_2O_3 particles produce an Airy disk with a diameter of 191 µm, 6.35 greater than the pixel resolution. The image resolution is hence small enough for the software to compute the intensity peak location with subpixel precision (avoiding the previously mentioned pixel locking).

3.2.3 Quenching distances and flame structure

The focal distance was set to the minimal supported by the lens, in order to have the highest possible resolution of 56.51 pix/mm ($res = 17.70$ µm/pix). The camera position was chosen to capture the flame tip for the conditions tested. The final captured area had an approximate size of 13×27mm. A $f/16$ aperture and an exposure time of 10 ms were used. Similarly to what was done in PIV, the acquisitions were conducted in a dark environment to reduce image noise and enhance contrast.

Prior to all acquisitions, an image intensifier gain for each OH^* and CH^* was set. The gains defined were maintained across all tests, to permit the comparison between results (of different fuels blends and flame conditions). The gain was increased until pixels started to saturate for the flame condition with stronger chemiluminescence (BG100, $\phi = 1.0$, $Re = 200$), to have the best image contrast possible for the weaker flames. When using the image intensifier, one should be careful not to operate it with small gains: that would imply to increase camera aperture and let more light to enter in the lens, which could burn the photocatode. In order to have a more precise estimation of d_q, 30 images were captured at a rate of 5 Hz for each flame condition. A 5 min interval was kept between acquisitions for the system to reach steady state conditions.

The accurate measurement of quenching distances relies on (i) correct calibration of setup (ii) information of wall position x_{wall}, and (iii) location of flame front boundary closest to the wall $x_{flm,0}$.

Subtracting their pixel coordinates in the image, d_q can be calculated:

$$d_q\,[\mu\text{m}] = (x_{flm,0}\,[\text{pix}] - x_{wall}\,[\text{pix}]) \times res\,[\mu\text{m/pix}] \tag{3.25}$$

In the following sub-chapters, methods to accomplish these requirements are described.

Alignment and wall coordinate

Prior to image acquisitions, a series of steps were carried out to ensure that the wall and camera were aligned with a precision down to the tenth of degree. This alignment process is crucial because a 1° angle misalignment can represent a deviation about 350 µm in the estimation of d_q. Therefore, the setup is mounted in a movable cart endowed of precise y translation and rotation movements, shown in Figure 3.10. At the end, this alignment method permits (besides the alignment) the calculation of image resolution and exact determination of wall pixel location (x_{wall} coordinate).

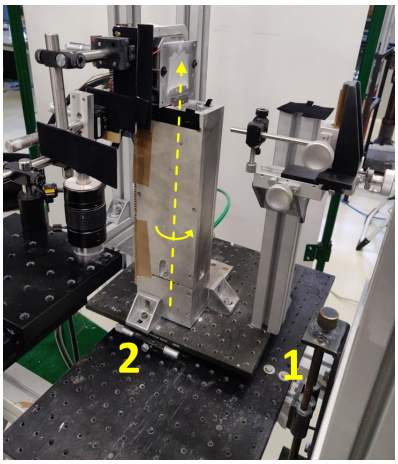

Figure 3.10: Equipment is fixed in platforms capable of y axis (1) translation and (2) precise rotation.

The method was adapted from the one used by Häber and Suntz [71] and uses a small ball bearing sphere, with diameter $D_{sphere} = 10.3\,\text{mm}$, that gently touches the wall (Figure 3.11) and is supported by small rod. Unlike a rectangular shape, the spherical shape can be identified even if partially hidden. This shape identification is done using the Hough transform in MATLAB image analysis toolbox, which returns the sphere center and radius. For these images taken during alignment, the camera aperture was set to the smallest one ($f/32$), to obtain silhouette shapes with sharper edges and facilitate image processing.

Figure 3.12 contains, from left to right, a scheme with different steps followed during the alignment. The process can be divided in six main steps:

1. The wall was moved to the left a distance equal to the radius of the sphere ($\Delta x = -D_{sphere}/2$). Then, with the sphere touching the wall, its center was located at the coordinate where the wall surface once was (Figure 3.12a).
2. With the sphere touching the wall at $z = 0$ (so its center would be coincident with the y axis, in turn of which the experimental setup can rotate), the setup must be moved until the center of the

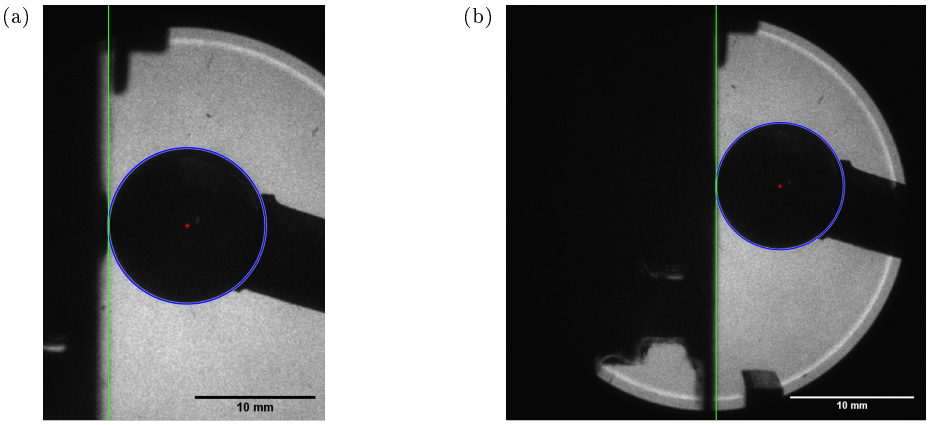

Figure 3.11: Photos of sphere touching the wall at $z = 0$, for a (a) not yet aligned and (b) aligned setup; sphere edges and centers are identified and the vertical thin line represents the coordinate where the sphere touches the wall, *i.e.* x_{wall}.

sphere was close to the half-width of the image captured. This allowed, at the end of the alignment, for the wall surface to be centered in the camera images.

3. The sphere was moved along z coordinate (Figure 3.12b) and pictures were taken at each position; the z coordinate displacement should be maintained relatively small (in the present work it was no more than 20 mm), before optical aberrations preclude the assumed linear relation between pixel horizontal distances and z coordinate, along the wall planar surface.
4. The images obtained in the previous step were processed: contrast was maximized to facilitate the identification of spherical shape using Hough transform, and sphere center coordinates were determined for each image.
5. The misalignment angle β was estimated from pixel horizontal offsets, calculated at each z coordinate; if it was not small enough (the objective was set to 0.14° in the present work[3]), corrections were made using millimetric angle adjuster and we went back to step 3; otherwise, we proceeded to the next step. At this point, although the evaluated sphere radius varies with z coordinate, the sphere center remains at the same x pixel if $\beta \approx 0$ (Figure 3.12c). The image in Figure 3.11a was taken after this step; notice there is a small shadow from the sphere on the wall, resulting from the wall not being fully aligned yet.
6. Lastly, the wall was moved to its final position ($D_{sphere}/2$ to the right); the wall surface was then perpendicular to the camera and close to the half-width of image captured (Figures 3.11b and 3.12d).

The sphere z coordinates were varied every 2 mm. The use of the smallest aperture possible translated into a wide depth of field and therefore the image remained focused (and sphere edges sharp) enough for image processing in the different z coordinates. The angle of misalignment was estimated using linear fitting to the data points, shown in Figure 3.13. It is possible to understand the outcome of successive β angle evaluations and corrections: repeating steps 3, 4 and 5 three times led to a misalignment angle of only $\beta = 0.045$ deg. When aligned, x_{wall} pixel coordinate (identified with vertical lines in Figure 3.11) is obtained using the evaluated sphere center coordinate and radius. Image resolution is evaluated as well,

[3] for estimated quenching distance errors associated below 50 µm

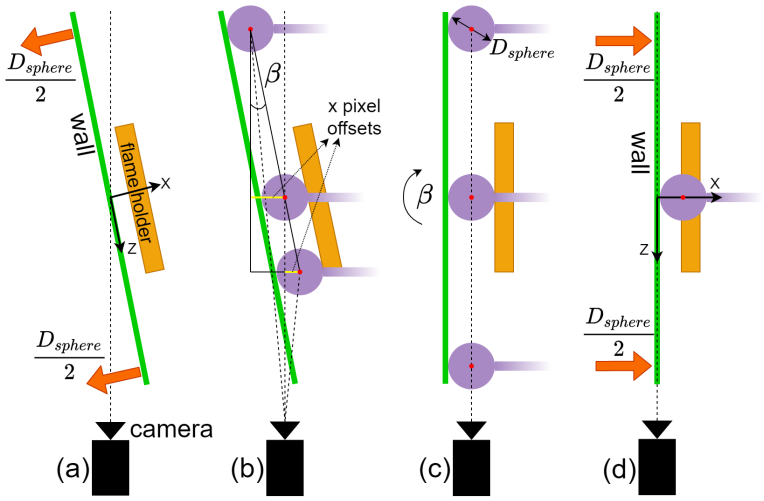

Figure 3.12: Camera and wall alignment involves different steps (a-d); the sphere of diameter D_{sphere} is used for perceiving the wall surface; at the end, the wall surface should be perpendicular to the lens (misalignment angle $\beta \approx 0$) and be in the half-width of the image.

from $res = D_{sphere}[\mu m]/D_{sphere}[pix]$.

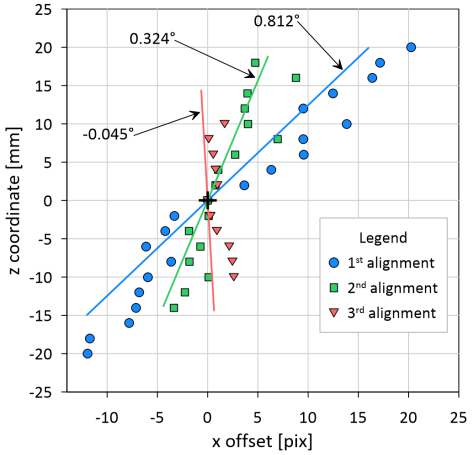

Figure 3.13: Sphere center offset for different z coordinates along the wall, in consecutive alignments. From the 1st alignment to the 3rd one, the misalignment angle β was reduced down to 0.045°.

Chemiluminescence images processing

Depending on the type and capabilities of the equipment (in case of experimental work) or available data (for numerical studies), a suitable methodology to identify flame front can be adopted from the many existing. Some authors use the HRR and its derivative ∇HRR [39, 43, 72–74]. Others, base themselves in temperature profiles and heat fluxes near the wall [39, 40, 47, 72, 75]. The concentration and/or molar fraction of species (CO_2, CH, CH_4) [42, 76] or even radicals fluorescence (usually OH) [40, 43, 77] can also be employed to anchor the flame front position. In the present work, another common methodology, based on the chemiluminescence of flame radicals, was chosen. This approach was employed by other authors performing similar types of studies [4, 71], as a qualitative way to identify the flame front.

The flame front was traced using the points where the intensity of OH* and CH* chemiluminescence

reached 50% of their maximum value. It was shown that there is a proportional relation between excited radicals concentration and their chemiluminescence intensity [78]. The use of the 50% intensity presents a robust technique, since this region of the flame has a better signal-to-noise ratio and is less sensitive to small perturbations in the flame, that could increase the uncertainty of the measurement.

Independently of the method chosen, its applicability and validity for all the conditions tested should be a major concern. As it will be demonstrated in results chapter 4.4, numerical simulations of a one-dimensional adiabatic flame confirmed that OH* and CH* peak concentrations are consistent with maximum HRR location for BG and BG + H_2 flames, endorsing the method chosen to identify the flame front.

These numerical simulations are performed using a mechanism based on GRI-Mech 3.0, which does not account for the N_2 chemistry. It is supplemented, however, with chemiluminescent species kinetics, to simulate the concentrations of excited radicals. The supplementary species and reactions are the result of multiple authors work, compiled by Quintino *et al.* [78]. In their work, the proposed kinetics model for chemiluminescent species was validated in biogas pre-mixed flames stabilized in a Bunsen burner. Later, Rocha *et al.* [79] did a similar analysis, validating this time the model for BG+H_2 flames. The final complete database was implemented in the Cantera Python module. With it, a 1D freely propagating adiabatic flame is simulated, with initial conditions $T_u = 298.15\,\mathrm{K}$, $p = 1\mathrm{atm}$.

The outcome of image processing techniques applied to an OH* chemiluminescence photo can be seen in Figure 3.14. The process involves image magnification by a factor of five, to increase its resolution and trace the flame front with sub-pixel precision. This is very important to enable a better statistical description of d_q, since its value will not be locked in multiples of pixel resolution. The pixels were interpolated using the linear method, leading to a resolution close to $3.54\,\mathrm{pix/\mu m}$. The pixels whose value is greater than $I_{max}/2$ define the region of the flame front. d_q can now be computed from the most left pixel and the well determined wall position coordinates (Equation 3.25).

Concentration of OH* was known to be a good indicator of the location and intensity of the HRR [80]. Furthermore, results from Panoutsos *et al.* [81] indicated that the relation between radical concentration and HRR was approximately linear. This was of major importance to give a physical interpretation to the pixel signal/intensity from OH* chemiluminescence (I_{OH}), and hence extend the interpretation of our results. Since the flame surface is projected on z axis, I_{OH} can be translated into the total volumetric heat generated $\dot{q}'''[\mathrm{W/m}]$ along the flame length (in z direction):

$$I_{\mathrm{OH}} \propto \int_{-l/2}^{l/2} \dot{q}'''\, dz \tag{3.26}$$

where l is the burner length (approximately equal to the flame length). If dimensions are to be attributed to I_{OH}, it represents a power per surface area *i.e.* $\left[\mathrm{W/m^2}\right]$.

For the results analysis, two useful variables related to the heat release were defined: heat release thickness $\delta_{q,\mathrm{OH}}[\mathrm{m}]$ and heat release in quenching $\dot{q}'_{q,\mathrm{OH}}$. Those were obtained from image processing of OH* radical chemiluminescence (Figure 3.15).

The heat release thickness is defined as the distance between the points where normalized pixel

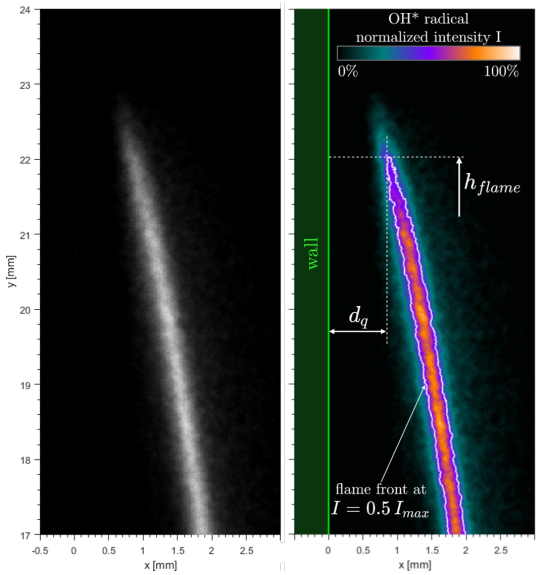

Figure 3.14: Photo of a BG60 20%H_2 flame ($\phi = 0.9, Re = 300$) using OH* radical (left) and the corresponding processed image (right), with the flame front position outlined in white; it corresponds to the pixels where the radical intensity reaches 50% of the maximum; the quenching distance is determined knowing the wall pixels location (x_{wall}) *a priori*.

intensity rise above ($x_{flm,1}$) and drops below ($x_{flm,2}$) 25%:

$$\delta_{q,\mathrm{OH}} = x_{flm,2} - x_{flm,1} \tag{3.27}$$

where, given the assumptions and the close relation with HRR, most of the combustion heat is produced. Those points are at the same height as of the pixel that defines quenching distance, marked with an horizontal arrow in the x direction, in Figure 3.15a.

As for the heat release in quenching, it is determined from the integral of pixel intensity, in the same interval that defines $\delta_{q,\mathrm{OH}}$:

$$\dot{q}'_{q,\mathrm{OH}} = \int_{x_{flm,1}}^{x_{flm,2}} I_{\mathrm{OH}}\, dx \tag{3.28}$$

and thus is an indicative figure of the amount of energy released in that zone, per unit length in y direction [W/m].

The choice of calculating these quantities along the x direction facilitated the numerical implementation for image batch processing. Figure 3.15b illustrates how $\delta_{q,\mathrm{OH}}$ and $\dot{q}'_{q,\mathrm{OH}}$ variables can be computed numerically, when the profile of I_{OH} at the y coordinate of quenching point is extracted from the image.

Uncertainties

The precision of measurement of quenching distances has systematic and statistical errors associated. The systematic errors arise mainly from pixel resolution and lens optical aberrations. Since the quenching region is located at half-width of the image, the region where d_q is evaluated does not suffer significant distortions and thus optical aberrations were neglected. The statistical errors arise from (i) the uncertainty associated with determining x_{wall} (quantified with 20 measurements and described with Student's t-

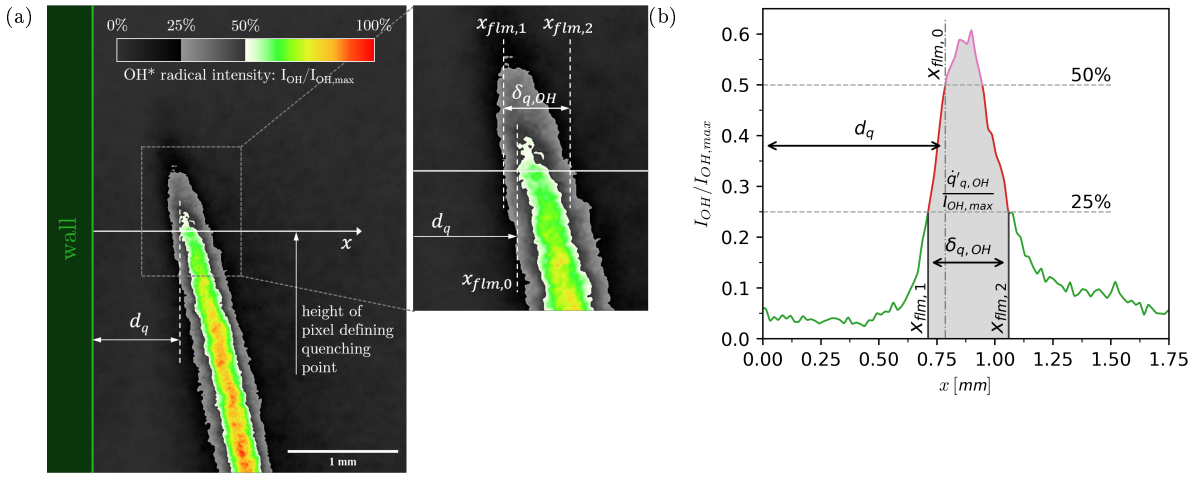

Figure 3.15: Calculation of relevant variables from OH* chemiluminescence: d_q, heat release thickness $\delta_{q,\mathrm{OH}}$ and heat release in quenching $\dot{q}'_{q,\mathrm{OH}}$; (a) processed image of a BG60 20%H_2 flame (same as Figure 3.14), with a colormap that highlights relevant thresholds (25% and 50%) of normalized pixel intensity; (b) profile of normalized pixel intensity in the x direction and at the height of the pixel defining quenching point.

distribution), and (ii) from the different evaluated flame tip positions (influenced by disturbances in flow and diffusion of chemiluminescent species) and camera noise. For the method used to determine the flame front, weaker chemiluminescent flames are more susceptible to noise introduced by the image intensifier.

Considering all sources of error, the final uncertainty in determining quenching distance is:

$$u_{95\%}(d_q) = \sqrt{u_b^2(res) + k^2\left[u_\sigma^2(\textit{flm front}) + u_\sigma^2(x_{wall})\right]} \tag{3.29}$$

where $u_b(res) = 17.70\,\mu\mathrm{m}/2$ is the systematic error from pixel resolution and $u_\sigma(\textit{flm front})$, $u_\sigma(x_{wall})$ are the error standard deviations associated to flame front position and determination of wall coordinate. To obtain the 95% confidence interval we used $k = 2$. Table 3.6 contains the average and maximum values of the error, considering all tested conditions.

Table 3.6: Uncertainties associated with the determination of quenching distances; entries without a value for u_r do not have a reference value.

			$u_{95\%}$		u_r	
			avg	max	avg	max
Quenching Distances	determine x_{wall}	[µm]	21.1	21.1	-	-
	flame front position	[µm]	60.9	138.8	5.63%	10.11%
	quenching distance d_q	[µm]	61.6	139.0	5.71%	10.13%

The choice of the 25% threshold to calculate $\delta_{q,\mathrm{OH}}$ and $\dot{q}'_{q,\mathrm{OH}}$ relates to the robustness of the method to be applied when processing all images. If the 50% was used instead, $\delta_{q,\mathrm{OH}}$ would be very thin and, for the weaker flames, uncertainty when calculating $\delta_{q,\mathrm{OH}}$ and $\dot{q}'_{q,\mathrm{OH}}$ would rise considerably. As Figure 3.15b suggest, when the chemiluminescence intensity is smaller than 25%, values are more susceptible to acquisition noise.

Chapter 4

Results

The results analysis begins with the characterization of TEG and system operation: power and efficiency maps were derived and with them, the influence of fuel blend and flame conditions in its performance was assessed. Meanwhile, the ability of the mathematical model to simulate TEG behavior was also appraised. To explain the patterns observed, we turned our attention into understanding the processes of heat transfer to the TEG. Results from velocity field are firstly analyzed, followed by a brief study on flame structure, considered fundamental to better explain the results shown in the last sub-chapter, regarding flame quenching.

4.1 TEG operation

To characterize TEG and system operation, tests were carried out for all fuel blends, Re and ϕ (Table 3.2). For higher equivalence ratios (hence higher flame speeds), some conditions resulted in resonating flames and therefore were not taken into account in the analysis. On the other hand, for certain fuels, flame flashback occurs for small Reynolds ($Re = 100$ and $Re = 150$) and higher equivalence ratios.

In order to validate the results and methods used, P_{TEG} and temperatures T_H, T_C obtained experimentally were compared with the values indicated in TEG's datasheet (Figure 4.1). The datasheet values of P_{TEG} correspond to the case with matched load resistance, *i.e.* $R_{e,load} = R_{e,TEG}$, and with homogeneous surface temperatures. These are represented with lines: one for $T_C = 30\,^{\circ}\mathrm{C}$ and another for $T_C = 50\,^{\circ}\mathrm{C}$. Experimental results from all tested conditions are grouped according to the measured T_C, and are represented by different markers.

For a certain T_C and T_H, all the P_{TEG} experimental values were smaller than datasheet's ones, with a maximum deviation close to 0.5 W. There are two factors contributing to this deviation. The first is related with the difference between $R_{e,load}$ and $R_{e,TEG}$ in our setup. This difference is always positive and tends to zero as the hot side temperature approaches its highest value. With this, one expects measured and datasheet's powers to become similar as T_H increases, and to deviate more for smaller temperatures. The second factor is that the temperature readings from the two thermocouples in the hot side do not represent the value of T_H indicated in datasheet, which is unique in the whole TEG hot surface. In fact,

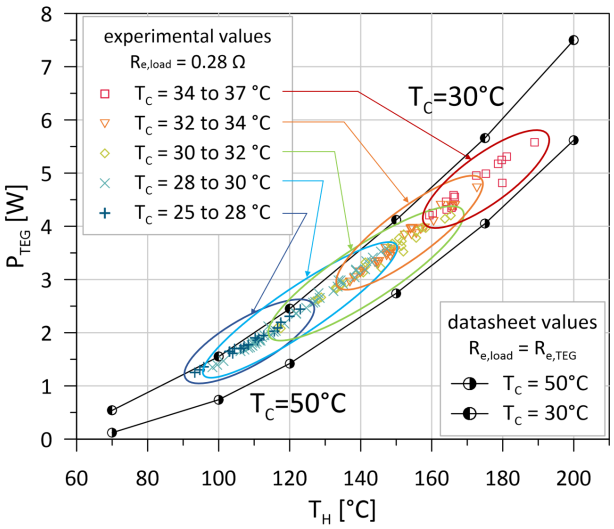

Figure 4.1: Variation of P_{TEG} with T_H and T_C surface temperatures: comparison between experimental results and TEG's datasheet information; lines correspond to datasheet values (considering homogeneous surface temperatures and matched $R_{e,load}$) and markers to experimental results.

that temperature distribution is far from being homogeneous in our experimental setup: regions close to plate tips and beneath the area where the flame quenches are colder than the region where thermocouples are placed (which is more exposed to the heat transferred from flame and burnt gases). As temperature raises, T_H thermocouples readings deviate more from the values presented in the datasheet, indicating higher temperatures than the mean temperature of the plate. Like the first factor, this contributed also for the measured points to deviate from matched P_{TEG}, but this time for the highest values of T_H.

The HX used was capable of keeping T_C at relatively low values for all tested conditions, since the difference between its maximum and minimum values was only 12 °C. The temperature difference between the two thermocouples placed in the cold side was on average 2.58 °C, indicating also a more uniform temperature distribution than the hot side surface. Small variations registered in the temperature of the tap water supplied to the HX (3 °C to 4 °C throughout the day) also hindered the repeatability of measurements.

These three factors represent thus the limiting aspects in our measurements. Nevertheless, the chosen methodologies allowed us to infer conclusions and figures about whether a specific condition is beneficial or not for P_{TEG} and why.

To better understand how the flame conditions influence the power yielded by the thermoelectric, P_{TEG} was mapped varying Re and ϕ. Figure 4.2 shows, as an example, the results from the tests conducted, using BG100. Power and efficiency maps for other fuel blends can be seen in Appendix D.1.

Fixing a specific burner Re number, P_{TEG} increased substantially with ϕ, from lean to stoichiometry. The power increase was less pronounced when fixing ϕ and increasing Re; for leaner mixtures and higher Re, that increase became insignificant. These tendencies were also maintained for all the BG and BG+H_2 blends tested and can be consulted in Appendix D.1. Previous results obtained for BG100 with a similar experimental setup [4] also endorse these observations[1].

[1] Although the different method to estimate the power yielded led to higher P_{TEG} figures, tendencies remained the same.

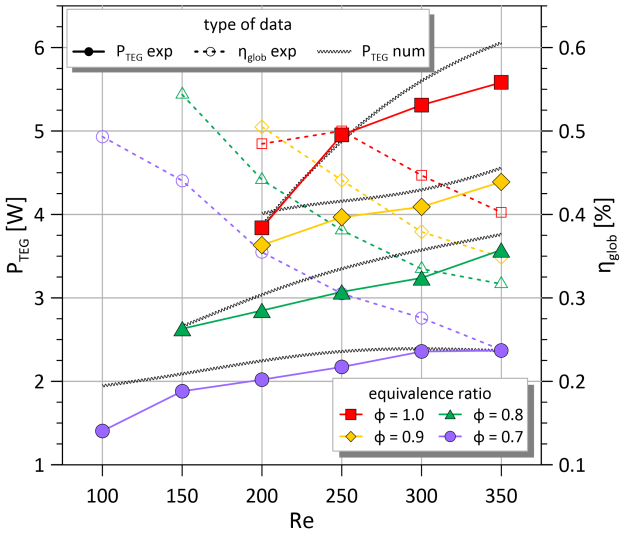

Figure 4.2: Map of P_{TEG} and global efficiency η_{glob} for BG100; filled markers linked by continuous lines indicate experimental P_{TEG} and hollow markers with dashed lines the correspond to η_{glob}; numerically obtained P_{TEG} (by the mathematical model) is also shown for each ϕ.

The estimation of P_{TEG} given by the mathematical model (for BG100) is also shown in Figure 4.2 by the black, thicker lines. Despite an overprediction, the curves follow closely the experimental values of P_{TEG}. The largest deviations between numerical and experimental values for BG100 occurred for the weakest and most powerful flame conditions (around 0.5 W). For other fuel blends, the model showed larger deviations for the most powerful flames, with $\phi = 1.0$.

As another way to characterize TEG operation, the thermoelectric efficiency was estimated from Equations 1.2, 2.11 and 3.13. It showed that η_{TEG} depended mainly on the mixture equivalence ratio (increasing with it), while Re promoted smaller improvements. Notice that η_{TEG} evolved in the same manner with Re and ϕ as P_{TEG} did, which can be explained if we realize that the influence of Re and ϕ in the TEG system is rather related with its cold and specially hot side temperatures (T_C did not change significantly). In fact, conditions with similar T_H yielded similar P_{TEG} and similar η_{TEG}. Larger temperature differences $T_H - T_C$ provide larger voltage drops at TEG terminals (from Seebeck effect - Equation 2.8) and improves power yielded. If $R_{e,load}$ and $R_{e,TEG}$ are kept close, η_{TEG} is proportional to Carnot's efficiency by a factor which depends on $Z\overline{T}$ (Equation 1.3). For the thermoelectric materials used in this TEG and range of temperatures registered, $Z\overline{T}$ varies at most 0.04 (between 0.76 and 0.81 - determined from materials properties in TEG's datasheet in Appendix B.1); the fluctuations in η_{TEG} are thus mainly attributed to the different T_H Reynolds and specially ϕ can produce. For most fuels, η_{TEG} reached the highest values for $\phi = 0.9, 1.0$ and $Re = 350$.

Regarding the influence of H_2, η_{TEG} improved slightly when χ_{H_2} was raised. That is also attributed to the aforementioned influence of T_H, which increased with the higher burnt gases temperature. Moving from BG60 to BG60+20%H_2 led to a η_{TEG} average improvement of 6.79% with respect to the value for BG60. When 20% of H_2 was added to BG80, the improvement was less pronounced: only 2.43%. Taking into account all the 142 conditions tested, η_{TEG} fits a normal distribution with mean value of 2.35% and a variance of 0.184%.

The system's global efficiency (shown in Figure 4.2 for BG100), was calculated from:

$$\eta_{glob} = \frac{P_{TEG}}{P_{flm}} \tag{4.1}$$

and is the ultimate efficiency one is interested in optimize. It exhibited the same dependency on ϕ and Re across all fuel types: there was a sharp decrease when increasing Re and, in general, it improved with ϕ. In terms of magnitude however, there were no sufficient differences in η_{glob} between fuels to tell if a specific fuel was superior to others: the overall maximum value of $\eta_{glob} = 0.65\%$ is reached when using BG60 with $\phi = 0.9$ and $Re = 100$; the minimum global efficiency was only 0.18%, registered for the same fuel mixture with $\phi = 0.7$ and $Re = 350$. As it will be explained ahead, this lowest efficiency is associated with the excessive height at which flame stabilizes. For most situations, η_{glob} value is located *ca.* between 0.25% and 0.50% (Appendix D.1).

Since η_{glob} varied significantly with the different flame conditions and, in opposition to η_{TEG}, decreased sharply whenever Re was incremented, it meant it was being largely influenced by another efficiency. That is associated with the heat transfer (HT):

$$\eta_{HT} = \frac{q_H}{P_{flm}} = \frac{\eta_{glob}}{\eta_{TEG}} \tag{4.2}$$

It tells how much of the flame heat power P_{flm} is being transferred to the TEG's hot surface. For BG100, as example, the values were higher than η_{TEG} and more disperse at the same time: the lowest efficiencies occurred for the highest Reynolds (minimum of 10.21%) and the highest efficiency was more than two times larger (23.4%). For all the conditions tested, η_{HT} ranged from 8.60% to 30.97%. One can conclude that the HT efficiency is considerably interconnected with η_{glob} and is the factor that is contributing the most to its variability, being affected in the same manner when varying flame conditions.

Although the tendency of power curves from flame condition remained the same for all the other fuels tested, the introduction of CO_2 and H_2 in the fuel mixture contributes to change the combustion reaction on several aspects (as explained in chapter 1.4), which ultimately affected T_H and, consequently, P_{TEG}.

In order to quantify the variation in TEG power yielded with different fuels composition, the percentage increase/loss of power ($\Delta\%P$) was calculated from fuel i to fuel j, and for each condition (ϕ_m, Re_n). Table 4.1 contains the results of that analysis, whose figures correspond to the average between all flame conditions:

$$\overline{\Delta\%P_{i\to j}} = \frac{1}{m \times n} \sum_{1}^{m} \sum_{1}^{n} \Delta\%P_{i\to j}(\phi_m, Re_n) \tag{4.3}$$

As expected, there was a significant loss of power when increasing χ_{CO_2} in the mixture, from BG100 to BG80 (-7.56%) and to BG60 (-13.75%). This power loss was compensated whenever hydrogen content increased. Adding 20% of H_2 to those BG mixtures helped to reduce the mentioned power loss (with respect to BG100) by more than half: BG80+20%H_2 and BG60+20%H_2 produced on average, less 3.33% and 5.62% of power than BG100, respectively. Moreover, the potential of using hydrogen as biogas dopant is emphasized when comparing the benefits of diluting BG60 and BG100 in a 50:50 proportion *vs.* diluting BG60 and H_2 in a 80:20 proportion (volume basis). The first situation is equivalent to move from

Table 4.1: Relative increase/loss of TEG electrical power between fuels. The value from row fuel i to column fuel j is calculated averaging all the individual Reynolds and equivalence ratios conditions, for which the equation $\Delta\%P_{i\to j}(\phi, Re) = (P_j - P_i)/P_i$ is used.

	BG100	BG80 0%H_2	BG80 10%H_2	BG80 20%H_2	BG60 0%H_2	BG60 10%H_2	BG60 20%H_2
BG100	0.00%	-7.56%	-4.84%	-3.33%	-13.75%	-8.48%	-5.62%
BG80 0%H_2	8.94%	0.00%	2.90%	4.88%	-6.93%	-1.24%	2.48%
BG80 10%H_2	5.61%	-2.73%	0.00%	1.73%	-9.54%	-4.08%	-0.59%
BG80 20%H_2	3.78%	-4.45%	-1.59%	0.00%	-10.86%	-5.56%	-2.26%
BG60 0%H_2	17.35%	7.87%	11.15%	12.96%	0.00%	5.52%	10.11%
BG60 10%H_2	9.93%	1.56%	4.61%	6.20%	-5.13%	0.00%	3.81%
BG60 20%H_2	6.34%	-2.02%	0.93%	2.58%	-8.81%	-3.57%	0.00%

BG60 to BG80, which yielded an improvement of 7.87%. The second situation corresponds to change from BG60 to BG60+20%H_2, which led to a larger improvement of 10.11%.

Regarding the mathematical model performance, it was satisfactory overall: despite sporadic deviations up to 0.75 W, the average over prediction from the mathematical model (in comparison with experimental P_{TEG} values) was only 0.19 W. The line that describes this relation fits the points with a coefficient of determination of 0.978 (Figure 4.3). This small over prediction can be attributed to a fact already enunciated, from the thermocouples in the hot side being placed in the hottest portion of the wall (close to the flame); their readings might not translate the true value of T_H across the entire hot surface. Recall that these temperatures were used to train a neural network and give two boundary conditions to the model (chapter 2.3).

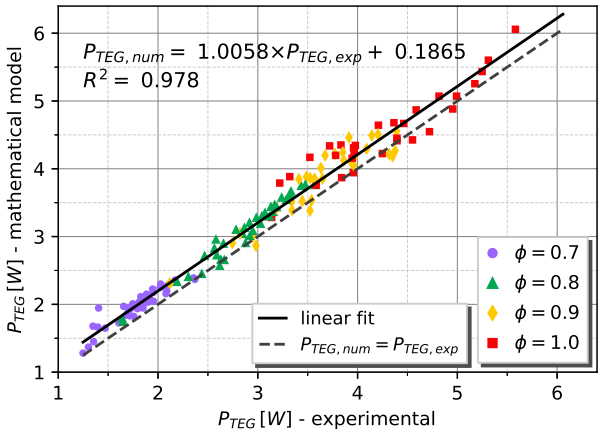

Figure 4.3: Performance of mathematical model in predicting P_{TEG}: comparison with experimental results; dashed line represents the location where numerical and experimental values are equal, while the continuous line is the linear fit to the points.

At the end of this sub-chapter, we can understand that the impact that different flame conditions and fuels have in TEG operation lies on the way they affect T_C and specially T_H. The influence fuels have in TEG operation is limited to the way P_{TEG} escalates with the different blends (shown in Table 4.1). As for system efficiency, it showed to depend mainly on η_{HT}, whose variation by more than three times between flame conditions reinforced the need to understand the mechanisms of heat transfer; not

only to dictate which conditions are the most favorable and why, but also to understand how the system can be further optimized. Besides, given the limitations of our setup, we realize that the TEG system (and η_{TEG}) cannot be further optimized: it would involve having $R_{e,load} = R_{e,TEG}$ or improving $Z\overline{T}$ of thermoelectric materials, which is impractical. Despite this, as it was shown, η_{TEG} will increase with T_H (hence with the amount of HT to the TEG). The way for improvement lies thus in the study of the heat transfer to the wall.

4.2 Heat transfer

To better understand the HT from flame and burnt gases to the wall, we analyzed the heat flux q''_{wall} profiles from BG100 flames in SWQ to a cold wall at 330 K. These profiles were obtained by two research groups, for the same burner and flame conditions, and are shown in Figure 4.4a. Kosaka *et al.* [75] deduced heat fluxes experimentally, measuring temperatures close to the wall (using CARS technique). They assumed one dimensional Fourier's law (Equation 1.4) to calculate q''_{wall} from an approximate temperature gradient near the wall (using temperatures measured at 100 µm from the wall). Zirwes *et al.* [74] performed numerical CFD simulations. As the authors suggested, their results showed good agreement with the experimental ones if scaled by a factor of 1/1.8. Our data extrapolation foresees the evolution of q''_{wall} beyond the available data.

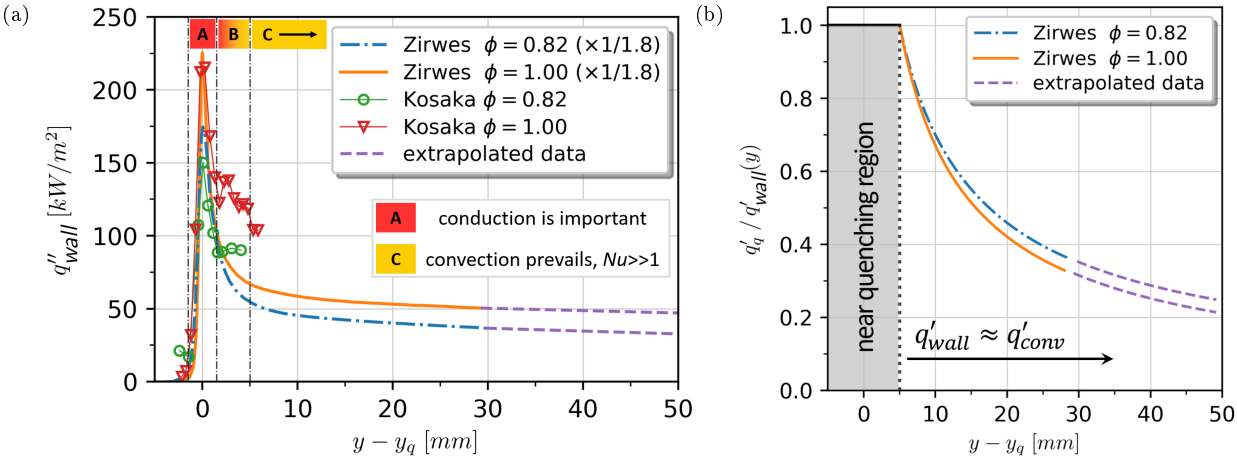

Figure 4.4: Analysis of wall heat flux q''_{wall} for BG100 flames in SWQ, as function of the y distance above the quenching point y_q, where q''_{wall} is maximum; (a) profiles are deduced using experimental [75] and numerical [74] results; (b) contribution of q''_{wall} near quenching region (q'_q) to the overall heat transferred to the wall (q'_{wall}), depending on the available height for HT above y_q.

Other authors [40, 47] show similarly shaped profiles for steady state SWQ. Different regions can be identified in these profiles. Those are marked (qualitatively) in Figure 4.4a with letters A, B and C. (i) In zone A there is an important contribution from conduction. In the literature it is often considered the unique HT mechanism in this region; q''_{wall} starts with a sharp increase, reaches a peak for the coordinate where flame lies closest to the wall (where d_q is defined) and decreases again abruptly, marking the end of the quenching region. (ii) In zone B, the wall heat flux diminish and convection gains importance over conduction (Nusselt number, Nu, increases), which might explain the deviation of experimental values

shown (derived from an assumption close to pure conduction) from the numerical ones. Finally, (iii) in zone C, convective heat transfer from the column of hot burnt gases to the wall prevails, due to the higher gases velocity and the formation of a thermal boundary layer [74].

To quantify the importance of the heat transferred near the quenching region to the total heat exchanged in the wall up to a certain y coordinate, the ratio:

$$\left.\frac{q'_q}{q'_{wall}\,(y)}\right|_{y\geq 5\,\mathrm{mm}} = \frac{\int_{-\infty}^{5\,\mathrm{mm}} q''_{wall}\,dy}{\int_{-\infty}^{y} q''_{wall}\,dy} \tag{4.4}$$

was calculated and plotted, for the two heat flux profiles from Zirwes *et al.* [74], in Figure 4.4b. As the equation suggests, the simplifying assumption of a coordinate ($y = 5\,\mathrm{mm}$) separating the regions near and farther away from the flame was employed. The location was chosen for marking the position where q''_{wall} enters the aforementioned regime governed by convection, where the direct influence of the flame to HT is no longer present. The data previously extrapolated for higher values of y was also included. Both curves are relatively close to each other, which is a sign that the shape of q''_{wall} curves of Figure 4.4a is similar for the two equivalence ratios. It is noticeable that, although it is very intense, the contribution from the heat transfer near quenching q'_q to the total heat transferred q''_{wall} decreases rapidly with the available area for convective heat transfer, upstream the flame front.

In view of what has been said about the aspects influencing conduction and convection along the wall, it was attempted to correlate P_{TEG} (which is known to increase with T_H and, hence, with the total heat transferred to the wall) with a reduced number of representative flame-related variables. Two were selected: the adiabatic flame temperature T_{ad} (for the close relation with T_b) and the Reynolds number (for increasing flow velocity and transport hot gases along the wall, essential for convection HT). The adiabatic flame temperature encompasses the effects from fuel blend composition and ϕ at the same time. T_{ad} varies approximately linearly with ϕ from 0.7 to 0.9 for BG100 [33].

The equation used to relate P_{TEG} with T_{ad} and Re uses three parameters k, a and b which are obtained by minimizing the mean squared error of the function (arbitrarily called F):

$$F(k,a,b) = \left|P_{TEG} - k\,T_{ad}^{a}\,Re^{b}\right| \tag{4.5}$$

which was calculated for all data points. Simplex optimization algorithm was used. The obtained correlation is presented in Figure 4.5, where it is shown that the variables and equation chosen can fit the data points with a coefficient of determination around 0.95.

This correlation is important because (i) describes power yielded in a simpler way, making up a practical tool to use (more than the developed mathematical model) to easily predict P_{TEG} or if the control of a future, optimized concept, is desired; (ii) allows to generalize and supports what was stated before, regarding the Reynolds influence: since $b = 0.38 < 1$, for successive increments of Re, the increment of P_{TEG} will be smaller and smaller, until the point when no significant improvement is noticed; (iii) finally, since P_{TEG} is closely related to T_H (and hence to q_{wall}), it suggests that the amount of heat transferred to the wall from flames in SWQ can also be described from T_{ad}, Re, and an equation

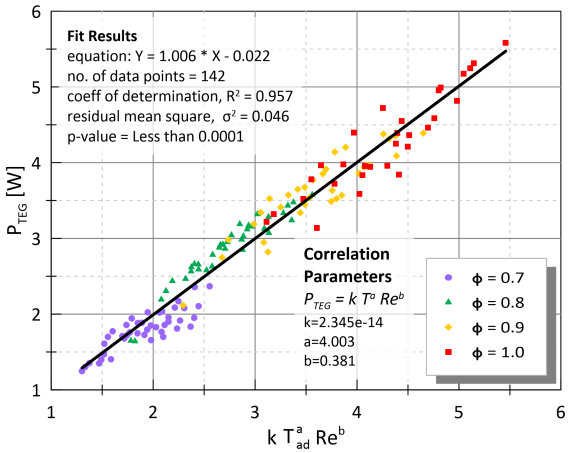

Figure 4.5: Correlation for simplified description of P_{TEG} from T_{ad} and Re, using an equation of the type $P_{TEG} = k\,T_{ad}^{a}\,Re^{b}$.

of this type.

Nevertheless, the reasons for the observed dependencies of P_{TEG} and η_{HT} on fuel mixtures, equivalence ratios and Reynolds numbers are still unclear and unexplained. As it was demonstrated in Figure 4.4b, convection upstream the flame can play a pivotal role in the total amount of heat transferred to the wall. For that reason, we decided to proceed with the examination of gases velocity field in the vicinity of the wall.

4.3 Velocity field

This analysis was carried out with the aim of knowing, in detail, the flame velocity field in SWQ: how magnitude, streamlines and velocity near the wall are affected by the different fuels and flame conditions, which are the most favorable ones, and what modifications in wall and/or burner geometry can lead to performance and efficiency improvements. The PIV results permitted a better understanding of the patterns and tendencies described when analyzing P_{TEG} and η_{HT}, and were also useful to validate the method used to calculate flame height.

Three fuel mixtures were selected (BG100, BG60, and BG60+20%H_2) and, for each of them, equivalence ratio and Reynolds number were varied. The resulting twelve test conditions allowed to study the influence of each parameter.

The patterns and characteristics of the flow field, as well as shapes of streamlines derived from PIV analysis (Figure 4.6) are in accordance to other numerical and experimental results [73, 77, 82] when characterizing flow field during SWQ of BG100 flames. The divergence of velocity, illustrated in the detail of Figure 4.6a, was used as a way to outline where the flame front laid at. Looking at the continuity equation:

$$\nabla(\rho\,\vec{V}) = V_x\frac{\partial\rho}{\partial x} + V_y\frac{\partial\rho}{\partial y} + \rho\nabla\vec{V} = 0 \tag{4.6}$$

one can conclude that when we are in the presence of reactive flows with significant changes in temperature, positive values of $\nabla\vec{V}$ must be associated with a decrease in gas density. As numerical studies

show [47, 74, 82], in SWQ the strongest temperature gradients are registered in the flame front. The contours of velocity divergence, plotted in the detail of Figure 4.6a, show the location where the change in gas density (and temperature) was more intense. The streamlines curve as unburnt gases reach the preheat zone of the flame. Since the left branch of the flame is close to the wall, there is less space for gases expansion and the curvature in the streamlines is more abrupt compared with the right branch of the flame. The projection of gases away from the wall ended up affecting the way the right branch of the flame stabilized: without being confined to a narrow space (like in the case of the left branch), streamlines show that a significant part of fuel mixture is consumed more gradually and over a larger area. Despite the observation at naked eye, that suggests the flame can be interpreted as symmetric for some flame conditions, these results prove that each side of the flame has distinctive kinetics. These conclusions can also be taken for other fuel blends other than BG100; plots with their velocity contours and streamlines can be found in Appendix D.2.

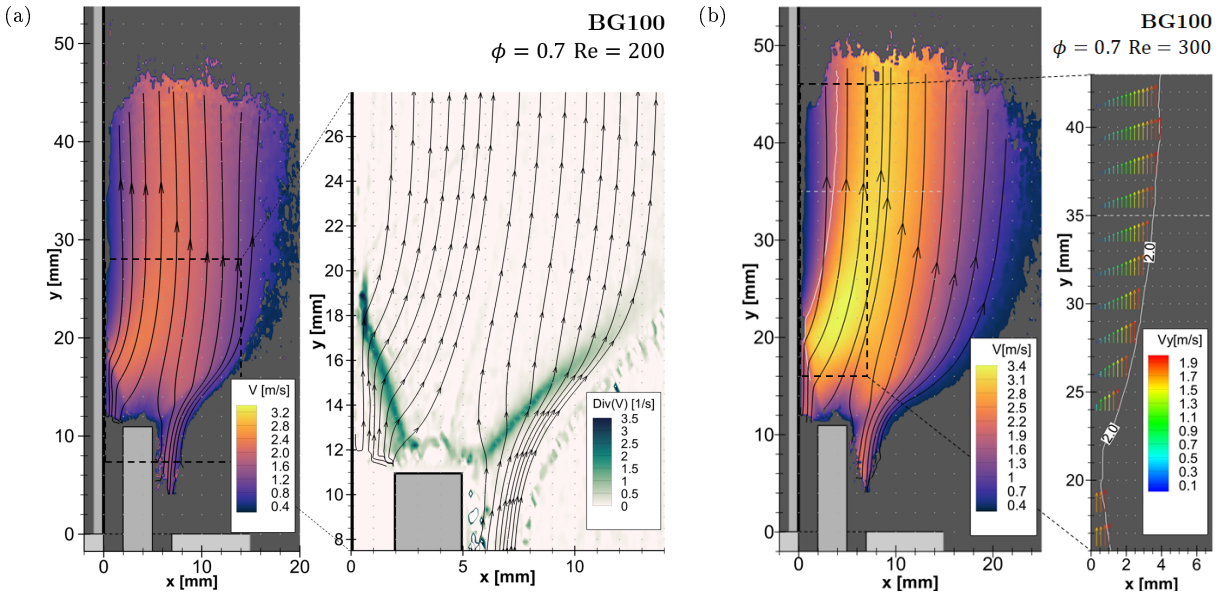

Figure 4.6: Velocity magnitude and streamlines for BG100 flames with the same equivalence ratio $\phi = 0.7$ and different Re; (a) $Re = 200$: velocity divergence $\nabla\vec{V}$ helped identify the flame location; (b) $Re = 300$: profiles of V_y along the wall, where the white line traces the contour where $V_y = 2\,\mathrm{m/s}$.

Increasing the Reynolds number by 100 influenced the velocity field significantly (Figure 4.6b): not only velocity magnitude increased, but also the projection of gases away from the wall led to a wider region of non-negligible average velocities. The velocity field is affected by different aspects. The most important ones are the velocity of unburnt gases leaving the burner's slits (associated with Re), buoyancy forces and isotropic expansion of heated gases. The last two aspects will ultimately depend on the temperature the burnt gases can reach. While the buoyancy forces act on the fluid in y direction and accelerate it upwards, the gases sudden expansion in the flame front contributes to deviate streamlines away from the wall, accelerating gases in both x and y directions.

Although there was not a reference velocity to properly define a boundary layer, by tracing isolines with a specific V_y, it was possible to capture the development of an hypothetical boundary layer. In Figure 4.6b and respective detail, the white lines correspond to the points where $V_y = 2\,\mathrm{m/s}$. The

"boundary layer" thickness reduced to a minimum near the quenching region, where $\partial V_y/\partial x$ reached its highest value. From that point on, one can assume that a new boundary layer, characterized by a rapid growth, develops. The increased dynamic viscosity and decreased density of high temperature gases will also contribute (in addition to the aforementioned gases expansion) to this faster boundary layer growth [83, 84], since viscous forces gain importance over inertial forces. Jainski *et al.* [77] conducted a PIV analysis in a similar setup and noticed the same effects during the SWQ of a turbulent flame. In those types of flames however, and according to their results, flame wrinkling and instantaneous quenching distance can alter significantly the shape of streamlines in quenching region. This, on its turn, affects the evolution and growth of the boundary layer, which is even greater than in the situation of laminar flames [85]. Also in what regards the balance between viscous and inertial forces for the case of turbulent flames and flows, the change in mixture kinematic viscosity can lead to increased length scales and even result in the relaminarization of the flow downstream the flame [42, 47].

Since the unburnt gases, in between wall and flame holder, approach the flame with $V_x \approx 0$ and the burnt gases leave the flame front with a velocity closer to its normal, the relation derived from unburnt gases and flame velocities:

$$\sin\theta = \frac{V_{flm}}{V_u} \tag{4.7}$$

can afford a rough estimation of the angle θ, at which flame stabilizes (Figure 4.7). It shows that higher V_{flm} will diminish the flame height, which of course, will dictate the y_q coordinate at which flame quenches and influence the area available for heat convection, upstream the flame.

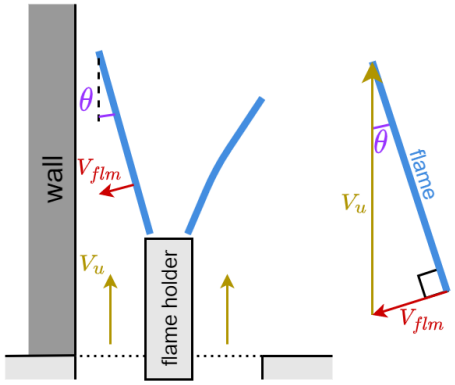

Figure 4.7: Estimation of stabilization angle θ from unburnt gases and flame propagation velocities.

Figure 4.8 contains velocity profiles taken at $y = 35\,\text{mm}$ (illustrated by the dotted line in Figure 4.6b). At this height, the velocity direction is close to vertical. The most important result from the graph is that the parameter affecting flow field the most was the burner Reynolds number: there are two clear groups of curves, one for $Re = 200$ (with filled markers) and another for $Re = 300$ (with hollow markers). Whenever changing either ϕ (identified with different marker shapes), the CO_2, or H_2 content of the mixture, the variations in peak velocity were much smaller (*ca.* 0.1 m/s to 0.3 m/s) compared to the ones when varying Re by 100 (close to 1 m/s). The graphic shows also consistent results regarding profile shape for $x < 5\,\text{mm}$, where neither fuel composition or ϕ influenced the shape of the curves. For $Re = 300$, V_y evolves approximately linearly with x, which is also verified for other y coordinates, as the

detail of Figure 4.6b shows. For the case of $Re = 200$, the shape of profile was also similar for different y coordinates. Appendix D.3 contains detailed V_x and V_y velocities for different y coordinates, for BG100, $Re = 200$, $\phi = 0.7$.

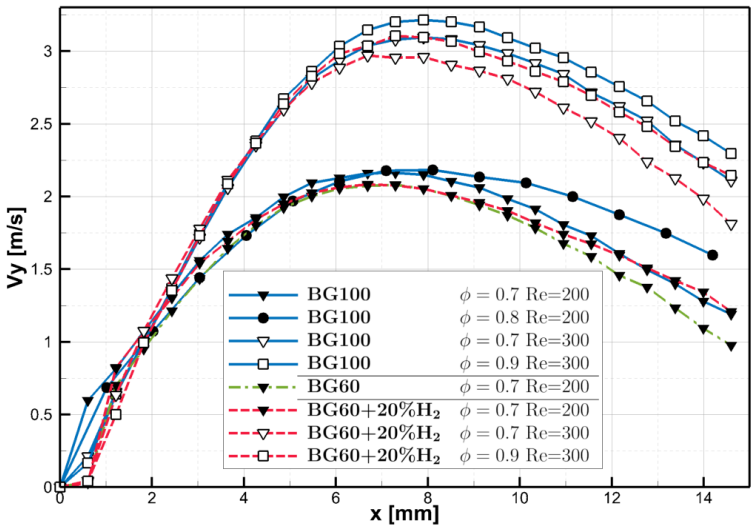

Figure 4.8: Velocity profiles at $y = 35\,\text{mm}$, near the wall, for different fuels and flame conditions.

The effects from gases expansion and their projection far from the wall was clearly noticed when moving from $\phi = 0.7$ to $\phi = 0.8$ in BG100, with $Re = 200$: although the peak velocity remains roughly the same in magnitude, its location moves slightly to the right and velocities get more intense for the points in the right end of the profile. This can also be observed, although less pronounced, when varying CO_2 and H_2 concentration. We can thus infer that the increase in velocity magnitude (using the means at our disposal) come at the cost of gases being pushed away from the wall.

In numerical simulations of flames in SWQ, results of temperature distribution evidence the formation of a thermal boundary layer right after the quenching region [47, 74, 76]. Any heat transfer process dominated by convection can be reduced to conduction when analyzed in the vicinity of the wall:

$$q''_{conv} = \kappa(T_{wall}) \times \frac{\partial T}{\partial x}\Big|_{x=0} \tag{4.8}$$

The thermal conductivity of burnt gases κ near the wall will increase with the surface temperature T_{wall}. The temperature gradient near the wall depends on several complex aspects: it will increase with higher burnt gases temperature, but only if velocity field and Prandtl number remain approximately the same. For all fuel compositions tested, it was verified from the adiabatic, numerical simulations that Prandtl remained approximately constant throughout the combustion process: it was bounded between $0.664 < Pr < 0.716$. Given this, if different flame conditions have similar velocity fields, the ratio between thermal and hydraulic boundary layers thicknesses is also similar and one can say that $\frac{\partial T}{\partial x}\big|_{x=0}$ will be higher for the situation where T_b is higher.

The effect of different fuel mixtures in T_b was already assessed: it degrades with carbon dioxide and increases with hydrogen addition. As ϕ approaches stoichiometry, a greater portion of the air in the blend takes part in the reaction, allowing burnt gases temperature T_b to increase. Reynolds number directly

influences velocity and, if the advection is significant, can also help transport hot gases farther up the wall, before they loose too much heat and reduce their temperature[2].

Even though the velocity measurement near the wall is limited beyond a certain x coordinate due to reflections (roughly $x < 0.8\,\text{mm}$), it is intelligible that the mentioned shift of peak velocity to the right hampers the increase of velocity gradient near the wall, which would turn out essential to increase the temperature gradient in Equation 4.8.

The way η_{glob} and, in particular η_{HT}, varies with Re and ϕ (chapter 4.1) can now be better understood. The increase of Re results in higher quantity of heat released, which is accompanied by stronger advection and will promote higher temperatures throughout the y coordinate. This was corroborated by temperature measurements. Its increase is however, also associated with a reduction in the area of heat transfer (flame height increases since V_u increases - Equation 4.7); besides, the velocity close to the wall does not improve significantly due to gases expansion and velocity profiles shift in the x direction (Figure 4.8). Even though increasing Re led to the increase of T_H measured in most situations (which is a sign that q_H increases), a large portion of the heat from P_{flm} is simply advected to the atmosphere. Without sufficient time to convect a great portion of flame heat to the wall, increases in T_H become less pronounced, and η_{HT}, η_{glob} drop down.

On the other side, if Re is kept constant, the velocity field in the vicinity of the wall is not severely affected, while at the same time T_b can be enhanced by approaching stoichiometry or adding H_2 to the fuel mixture. This results in a larger area for heat transfer (flame stabilizes at smaller angle because V_{flm} increases) and, since Prandtl number and velocity profiles are maintained, higher temperature gradients near the wall are expected, favoring the increase of q_{conv} and overall η_{HT}.

4.4 Flame structure

After analyzing how fuels and flame conditions affected the convective heat transfer, P_{TEG}, and efficiencies, the analysis will now focus on the flame itself. This investigation of flame structure by chemiluminescence techniques was considered vital not only to validate methods to calculate d_q, but also to help understand the phenomena observed during quenching. In this chapter, the influence of H_2 and ϕ in the flame structure is studied, for which information from important chemiluminescent species OH^* and CH^* is used.

In order to validate the acquisition methods and choice of the 50% chemiluminescence intensity as flame front markers, numerical simulations of excited radical concentrations from Cantera's 1D adiabatic flame were compared with the chemiluminescence intensity from experimentally acquired images, for representative fuels and equivalence ratios. In Figure 4.9a, the two types of results are plotted. The coordinate $z_{flm} = 0$ corresponds to the midpoint between $z\,(\text{HRR}_{max})$ and $z\,(\nabla(\text{HRR})_{max})$, which is often used to define the flame front. The vertical lines near $z_{flm} = 35\,\mu\text{m}$ correspond to the maximum heat release rate (HRR) locations for the different flames. These locations are calculated from the simulations and therefore refer only to numerical results.

[2]This was verified experimentally with a Pt/Rh *R-type* thermocouple at the top end of the plate.

The experimental values were obtained from the pixel intensity, measured perpendicularly to the flame front, in the zone between the flame holder and quenching region (see flame picture of Figure 4.9b - BG60, $Re = 200$, $\phi = 0.9$, OH* radical). The experimental results were anchored to the z_{flm} axis by making coincident the experimental and numerical CH* radical peak, for each mixture. Experimental results are plotted together with numerical ones on the same axis (with adequate translation from pixels to micrometers units) solely to compare profiles shapes and patterns.

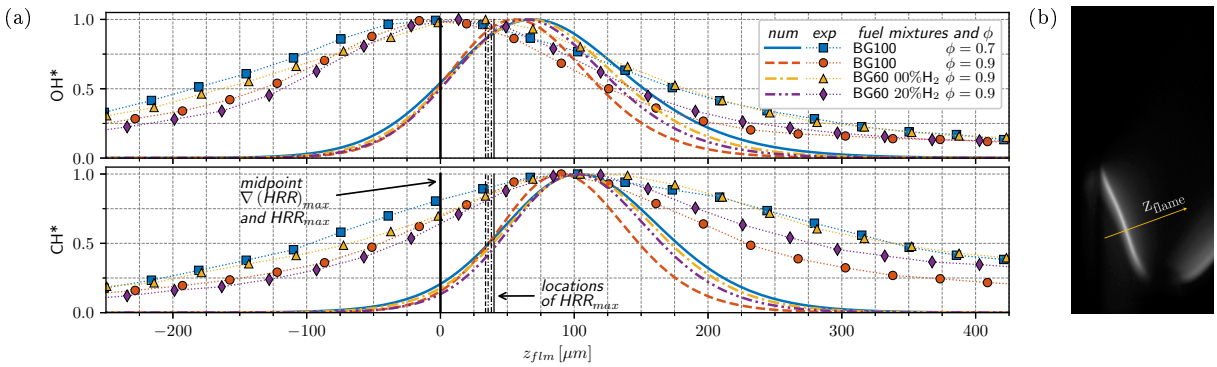

Figure 4.9: (a) Chemiluminescence and concentration profiles of OH* and CH* for four different conditions, at $Re = 200$. Thicker lines correspond to normalized concentration of radicals, obtained from numerical simulations; markers correspond to normalized experimental chemiluminescence intensity, (b) measured in the region illustrated for BG60, $Re = 200$, $\phi = 0.9$ (OH* radical); maximum peaks of CH* were made coincident for experimental and numerical results.

For both numerical and experimental data, OH* peak concentration and chemiluminescence intensity always preceded the CH* one. The distance between radicals peaks was consistent also: about 37 µm on average for 1D adiabatic simulations and 84 µm for chemiluminescence results. This consistency is in accordance with numerical and experimental results from Kathrotia *et al.* [80]: for BG100 + H_2 + Air mixtures and different ϕ they reported invariable distance from OH* and CH* peaks to the maximum HRR location. Numerical simulations conducted by other authors [81], this time for BG100 + Air planar flames with different ϕ, also state a regular distance from OH* and CH* peaks to the maximum HRR location. They found this distance to be from 25 µm to 40 µm for OH* and from 60 µm to 80 µm for the case of CH*, which is in agreement with our numerical results shown in the Figure 4.9a.

More importantly, taking into account the methodology used to trace the flame front, is the fact that the 50% normalized concentration of OH* deviated less than 5 µm from the estimated flame front coordinate $z_{flm} = 0$, for all the conditions simulated. It is an evident proof that those are strongly correlated. For the case of CH*, the 50% normalized concentration was rather correlated with the maximum HRR location, being no more than 10 µm apart from each other. That said, it is shown that the 50% chemiluminescence intensity from CH* and specially OH* are excellent HRR and hence flame front position markers, and can be used to calculate quenching distances.

The broadening of the profiles obtained experimentally is a consequence of the fact that neither the flame is close to be one dimensional (reactants had a small velocity component which was tangential to flame front, as PIV results demonstrated), neither it is adiabatic. This will slow down all the flame kinetics and diminish the Damköhler number [33, 47] *i.e.*, the ratio between transport and reaction time

scales. As a result, reactions take more space to complete and the flame thickness increases, leading ultimately to wider profiles of OH* and CH*. This is evident also looking at numerical and experimental results separately: the mixtures with widest (BG100, $\phi = 0.7$) and narrowest (BG100, $\phi = 0.9$) profiles coincide in numerical and experimental results. These correspond to mixtures with slower and faster reaction kinetics, respectively.

The chemiluminescence intensity will increase with the number of excited radicals CH* and OH*, which are products of exothermic reactions. As they pass from the excited to the ground state, photons in a specific wavelength are emitted. In Figure 4.10 one can distinguish, in detail, the chemiluminescence of the two radicals: an average between the two images shows the global shape of the flame; by applying an exponential filter (to highlight the pixels with highest values) and overlaying OH* and CH* images, it is possible to see that the highest intensity of chemiluminescence occurs in the mentioned region between flame holder and quenching zone. The higher velocity and flow rate of reactants in the middle of the burner's slit channel translates into greater species concentration, increased amount of exothermic reactions (whose products include CH* and OH*), and consequently higher flame temperatures and emission of spontaneous light.

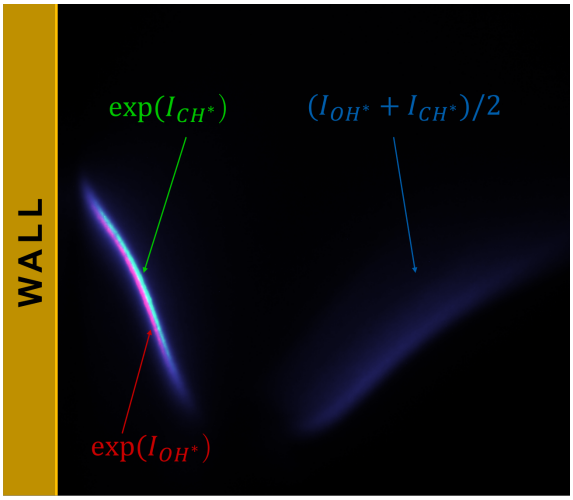

Figure 4.10: Overlay of processed OH* and CH* images (colored in red and green, respectively) of a BG100, $\phi = 0.9$, $Re = 200$ flame; an exponential filter was applied to the radical images; the image in blue is the average between the two radical images and shows the global shape of the flame.

From our observations it was noticed that the light intensity from OH* and CH* decreases whenever moving to leaner equivalence ratios or diluting CO_2 in the mixture. On the contrary, adding H_2 increases the chemiluminescence intensity. From the mixtures studied and presented in Figure 4.9, the ones that resulted in more intense radiated light (for both OH* and CH*) were, in descending order: BG100, $\phi = 0.9$; BG60+20%H_2, $\phi = 0.9$; BG60, $\phi = 0.9$; and BG100, $\phi = 0.7$. For Reynolds $Re = 300$, Figure 4.11 allows to make comparisons not only about chemiluminescence intensity, but also about flame propagation speed. From the pictures it is expected BG80+20%H_2 to have the highest flame speed since its flames stabilize with the smallest height and thus largest stabilization angle (Equation 4.7). The different intensities in each branch (left/right) of the flames evidences again the asymmetry in flame structure and kinetics, already indicated when analyzing flow field (chapter 4.3).

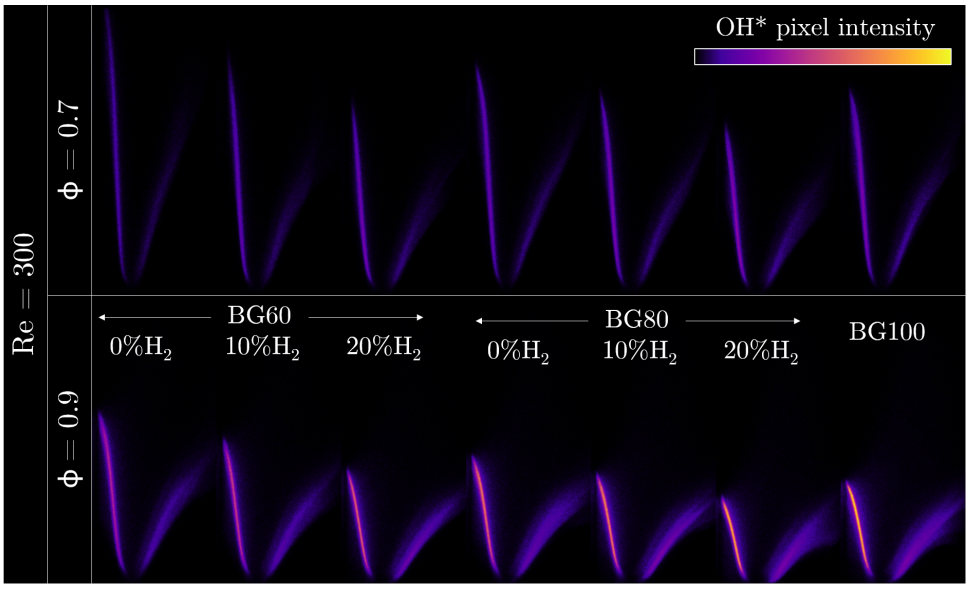

Figure 4.11: Chemiluminescence of OH^* for all the flames tested for Reynolds number $Re = 300$; a colormap is applied to the raw images to highlight the differences in intensity.

The intensity of OH^* and CH^* chemiluminescence has been shown also to be related to the magnitude of HRR for different equivalence ratios of methane-air premixed flames [81]. This HRR intensity has a pivotal importance in the distance a quenched flame stabilizes from the wall and in the heat transferred to the wall, as we will discuss further ahead (chapter 4.5.2). It is therefore important to better understand how ϕ, χ_{CO_2} and χ_{H_2} can affect it. Regarding the equivalence ratio, even though it does not change the chemical path of reactions significantly, the changes in fuel mass fraction will directly affect the concentration of OH and CH in the flame front. The reduced flame temperature is a sign that the amount of energy available to excite these species is also smaller, ultimately leading to weaker chemiluminescence. Adding carbon dioxide will lead to the same results, since the aforementioned dilution and thermal effects will reduce the concentration of combustible fuel (and species) and the flame temperature. When the amount of H_2 enrichment in biogas blends increases, the formation of species such as H, O and OH are enhanced [36]. These species are crucial to increase reaction rates of exothermic reactions that account for a great portion of total heat released during biogas combustion. According to Wei *et al.* [35], H_2 reactivity is further highlighted as the content of carbon dioxide in biogas increases. It can induce early heat release at low temperatures and enhance maximum HRR at high temperatures. All the reactions will take place faster and the chemical energy of reactants will be released quicker, causing a spike of HRR and excited species concentration.

The information from this brief analysis permitted not only to prove that the flame tracer method is adequate for calculating the quenching distance, but also to explain how the fuel mixture and equivalence ratio affect radicals concentration, chemiluminescence and HRR (which is crucial for the flame quenching).

4.5 Quenching distances

Quenching distances were determined for all fuel blends (Table 3.2). Two equivalence ratios $\{0.7, 0.9\}$ and two Reynolds numbers $\{200, 300\}$ were studied for each blend. For BG100, $\phi = \{0.8, 1.0\}$ were also included in the tests for comparison with literature. There were in total thirty different conditions, for which chemiluminescence of both OH* and CH* was analyzed.

To the best of our knowledge, there are no previous works about side-wall quenching of stationary BG + H_2 + Air premixed flames. On the contrary, for CH_4 + Air flames, several articles can be found in literature for different quenching configurations (tube, parallel plates, transient and stationary flames in HOQ and SWQ). Three of them were considered to compare and validate results, for being the most relevant and novel works about experimental quenching distance measurement in a similar SWQ configuration. Their results are presented in Figure 4.12a. Jainski *et al.* [40], Häber *et al.* [71] and Kosaka *et al.* [43] all shared the same burner and flame conditions; their flame is turbulent and nearly 13 times more powerful than ours ($Re = 5000$ and $P_{flm} \approx 10\,\mathrm{kW}$).

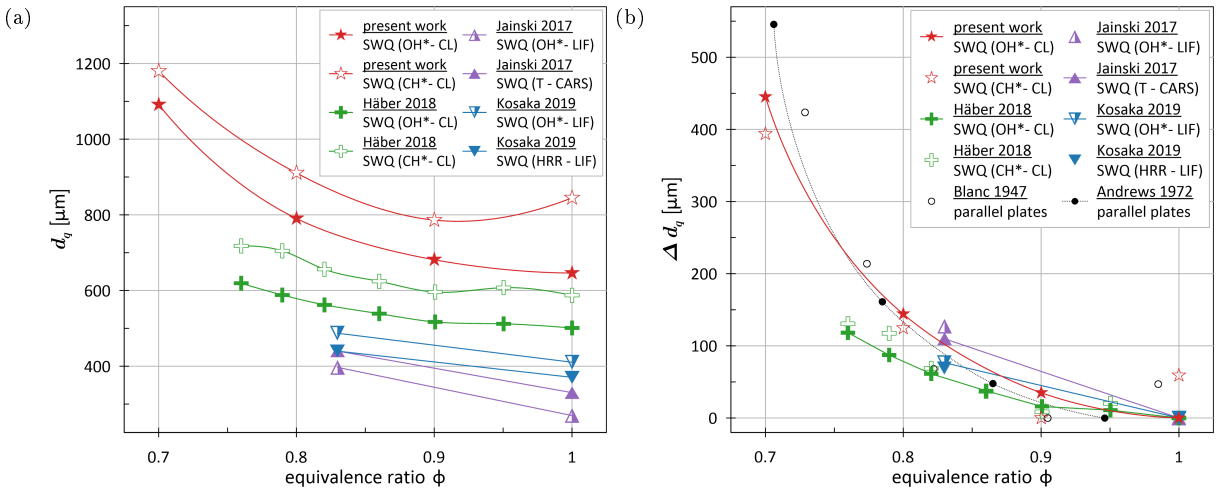

Figure 4.12: Comparison of (a) absolute d_q and (b) relative $\Delta d_q(\phi) = d_q(\phi) - d_{q,\,min}$ for BG100 + Air premixed flames by several authors, where "chem" denotes chemiluminescence methods, "LIF" stands for Laser Induced Fluorescence, and "CARS" for Coherent anti-Stokes Raman spectroscopy; the HRR method used by Kosaka et al. is based on the measurement of CH_2O and OH fluorescence.

In their papers the authors used different experimental techniques, which led to differences in d_q up to 300 µm. Chemiluminescence techniques resulted in the highest values of d_q. The results attained in this work are, however, the highest of them all. They are about 200 µm higher than the ones from Häber (both for OH* and CH* radicals). The calibration process also makes the measurements extremely sensitive to small setup misalignment. Authors usually compare results and tendencies using a relative quenching distance defined as:

$$\Delta d_q(\phi) = d_q(\phi) - d_{q,\,min} \tag{4.9}$$

which disregards systematic errors and is less susceptible to aspects such as surface temperatures (d_q decreases with T_{wall}) and flame front identification methods. Those are plotted in Figure 4.12b and show that the evolution of d_q obtained in this work is homologous to the results from other works, specially if

we consider the use of OH* radical. All the results show decreasing differences in d_q when moving from lean to stoichiometric mixtures, following trends similar to hyperbolic curves. Two sets of quenching distances in parallel plates configuration were also included for comparison [86, 87] and, interestingly, those had an evolution close to the one registered by us in SWQ, even despite the fact that, in absolute terms, d_q is much larger for that situation. For all works, the minimum d_q ($\Delta d_q = 0$) was reached for $\phi = 1.0$ with the exception of our CH* and Blanc [86] results, where the smallest d_q was for $\phi = 0.9$.

4.5.1 BG and H_2

Regarding the influence that biogas and H_2 have in the flame quenching distance, d_q increased with χ_{CO_2} and decreased with χ_{H_2} (Figure 4.13), as expected from flame and radicals chemiluminescence analysis.

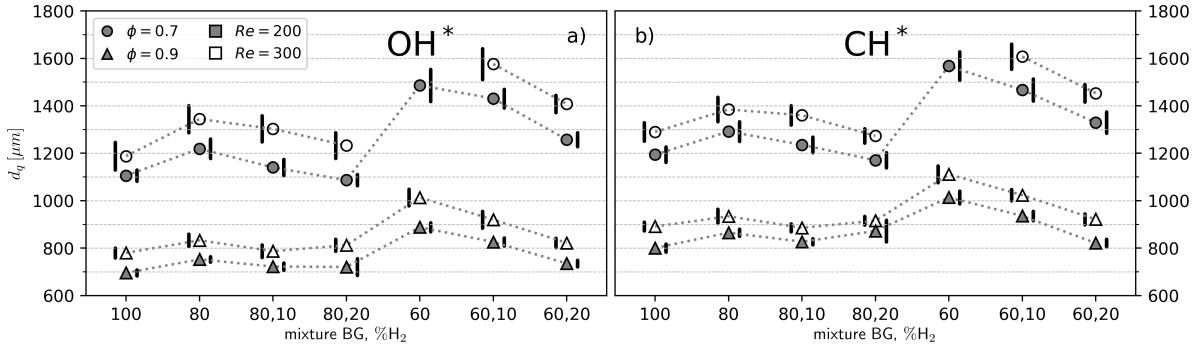

Figure 4.13: Quenching distances for all fuels tested, $\phi = \{0.7, 0.9\}$ and $Re = \{200, 300\}$, evaluated from (a) OH* and (b) CH* chemiluminescence; some conditions are not shown due to the excessive flame height (not captured on camera); error bars represent the ± standard deviation from the 30 different d_q values computed for each condition; markers fill relates with Re and their shape with ϕ.

Although tendencies in d_q for the two radicals are the same, quenching distances using OH* (Figure 4.13a) radical were always smaller than the ones using CH* (Figure 4.13b) by, on average, 85.6 µm (u_σ = 36.2 µm standard deviation), which is practically the same value as the mean distance between peaks of OH* and CH* chemiluminescence profiles, for the mixtures shown on Figure 4.9 (84 µm). This is also in conformity with the values obtained by Häber *et al.* [71] for methane flames, who report a difference in the order of 100 µm.

The flames with higher Reynolds number yielded larger values of d_q. For each fuel blend and ϕ, the ratio $d_q(Re = 300)/d_q(Re = 200)$ was practically constant: using the OH* chemiluminescence, that ratio was on average 1.119 (with a u_σ of only 0.028); for CH* the average was 1.091 and the standard deviation 0.018.

For leaner flames (and specially for $Re = 300$), the variance associated with d_q was, in general, higher. At these conditions, the flame stabilized at a smaller θ angle (Equation 4.7 and Figure 4.11) and struggled to overcome the velocity of unburnt mixture. With this, the flame tip became very sensitive to small perturbations in the mixture blend homogeneity or even flow rate, being momentarily closer or farther away from the wall. The narrower range of pixel intensity values for leaner flames also made the process of determining flame front more sensitive to camera and image intensifier noise.

Figure 4.13 shows that blends of BG80+10%H_2, BG80+20%H_2 and BG60+20%H_2 yielded approxi-

mately the same quenching distance of BG100. The contribution of H_2 to reduce d_q depends however on the type of biogas mixture. 20% of H_2 addition to BG60 reduced d_q by 18.1% on average ($u_\sigma = 2.1\%$), while for the case of BG80 the improvement was smaller and less consistent, with 6.4% on average ($u_\sigma = 3.3\%$); in particular, when the content of hydrogen in BG80 with $\phi = 0.9$ changes from 10% to 20%, there was no improvement in d_q, which contrasts with all the other results. With the increased content of H_2 (and consequent reduction of non combustible CO_2) in the mixture, the number of exothermic reactions increases, leading to higher HRR and mitigating the reduction in reaction kinetics near the wall due to lower temperatures (more heat losses). Since H_2 also changes the chemical path of combustion process and increases the number of low-energy activation reactions, the flame can survive with higher energy losses. The flame and radicals are thus able to approach the wall further when H_2 is present in fuel mixture. As evidenced by the results, this influence will be more notorious when the grade of biogas fuel is lower (when biogas has more CO_2).

Even though the wall temperature T_{wall} influences the quenching distance (chapter 1.4.1), the small temperature differences registered for the conditions tested do not have a significant influence on the result of d_q. From the measurements at different T_{wall} by Kosaka *et al.* [43], an increase in temperature of 240 K led to a reduction in d_q only about 100 µm in methane premixed flames. Boust *et al.* [41] increased T_{wall} by 200 K and obtained smaller quenching distances around 50 µm. In the Table 4.2, temperatures measured by the two thermocouples in the hot side of TEG surface (Figure 3.2) are shown for some of the tested conditions. For being very thin (1 mm) and made of Aluminium ($\kappa = 237\,\mathrm{W/(K\,m)}$), the temperature difference between the hotter and colder sides of Al plate is small enough to state that $T_{wall} \approx T_H$. From all conditions tested, BG60 ($\phi = 0.7$, $Re = 200$) has the smallest T_H temperature, whilst the highest T_H was recorded for BG100 ($\phi = 0.9$, $Re = 300$). This surface temperature difference of only 60 K is small when compared to the value $T_{flm} - T_{wall}$ (Equation 1.4), which is *ca.* 1100 K if $T_{flm} \approx 1500$ K is assumed [39] and confirms that T_{wall} does not have a significant influence in d_q for the conditions tested.

Table 4.2: Temperatures in the hot side of the TEG module for different fuels and flame conditions; $T_{H,b}$ and $T_{H,t}$ represent respectively, the bottom and top thermocouples values.

Fuel	ϕ	Re	$T_{H,\,b}$ [K]	$T_{H,\,t}$ [K]
BG60	0.7	200	378.2	381.8
BG60+20%H_2	0.9	200	424.1	413.3
BG60+20%H_2	0.9	300	426.4	423.9
BG80+20%H_2	0.9	300	434.3	425.5
BG100	0.9	300	438.3	428.7

As stated in the introduction, the contribution from radical recombination at the wall increases with wall temperature and/or type of species and their concentration (sub-chapter 1.4.1). In hydrogen combustion, those reactions start to gain importance at lower temperatures. Popp and Baum [45], in their study of premixed BG100 flames at different equivalence ratios in HOQ, concluded that beyond 400 K, the wall can no longer be considered completely inert for radical recombination reactions. Häber and Suntz [71] assumed $T_{wall} = 500$ K as the upper limit for reasonable description of quenching solely

by heat losses, for lean/stoichiometric premixed BG100 flames. Regarding $H_2 + O_2$ mixtures, [44] state that for the range of surface temperatures tested by them ($298\,\mathrm{K} > T_{wall} > 423\,\mathrm{K}$), the opposing trends from experimental and numerical results in SWQ and HOQ arise from the absence of models to simulate radical recombination at the wall. The radicals which recombine at the wall surface are the same ones that take part in crucial exothermic, low activation energy reactions at the lower temperatures of the flame pre-heat/induction zone, to trigger other reactions. In the quenching region, if T_{wall} is sufficiently high, a bridge for radical diffusion is made between flame induction zone and the wall: the abundant concentration of species boosts mass diffusion towards the wall (where Soret effect can also play an important role in the diffusion of H radicals). In this situation, these surface recombination reactions become the dominant means of consumption of flame radical species. A depletion of important radicals in the flame forces it to stabilize at a higher distance from the wall, hence increasing d_q. One of the most important recombination reaction at the wall, either for CH_4 + Air [45] and $H_2 + O_2$ [47] premixed flames, is:

$$H + OH + M \longrightarrow H_2O + M \tag{4.10}$$

Since the concentration of H and OH species increase when hydrogen is used, and given the mentioned literature's temperature range for which radical recombination reactions were noticed, one cannot rule out completely the influence that they might had in our tests. Moreover, the exception in d_q decrease for BG80+20%H_2, $\phi = 0.9$ could be explained on this basis.

4.5.2 Quenching distance, HRR and HT

On the assumption of heat losses governing flame extinction, the quenching distance d_q will depend on the amount of heat the flame is able to lose at a certain temperature T_{flm}, beneath which there is no sufficient heat energy to activate the oxidation reactions. It is known T_{flm} does not vary significantly for BG100 lean premixed flames [39]. Therefore, it was attempted to correlate d_q only with the amount of heat generated in the flame tip. To do so, a single variable $\overline{\dot{q}'''_{q,\mathrm{OH}}}$ obtained from chemiluminescence information was used:

$$\overline{\dot{q}'''_{q,\mathrm{OH}}} = \frac{\dot{q}'_{q,\mathrm{OH}}}{\delta_{q,\mathrm{OH}} \times l} \tag{4.11}$$

and translates into an average HRR in the quenching region. The heat release thickness $\delta_{q,\mathrm{OH}}$ and heat release in quenching $\dot{q}'_{q,\mathrm{OH}}$ were defined in Equations 3.27 and 3.28, respectively; l is the burner slit length.

The correlation obtained is shown in Figure 4.14. The data was split by Reynolds number and points were fitted with a curve of the type:

$$d_q = a \times \overline{\dot{q}'''_{q,\mathrm{OH}}}^{\,b} \tag{4.12}$$

The results show that d_q can be described only from the the HRR in the flame tip: the curves show excellent agreement with the points of all fuel blends and equivalence ratios, with coefficients of determination above $R^2 > 0.98$. Moreover, the two curves obtained have a similar exponent parameter $b = -0.45$; the constant of proportionality a will rather escalate with Re.

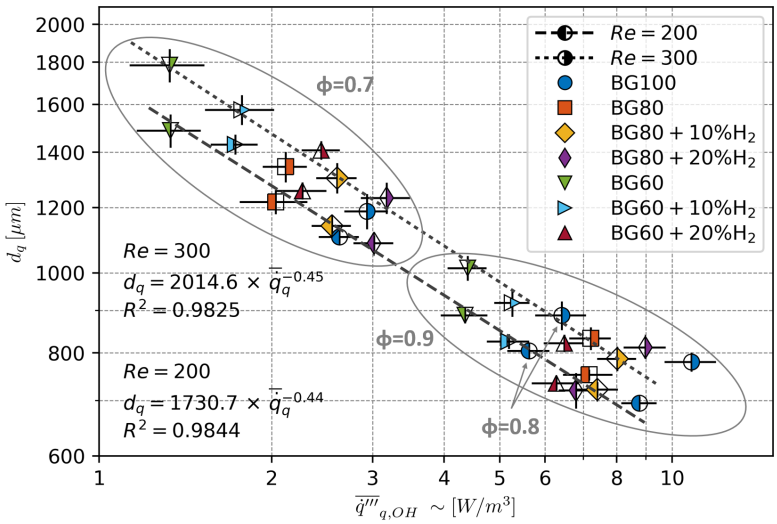

Figure 4.14: Quenching distance dependence on the average flame tip HRR, in the quenching region; error bars represent the ± standard deviation of the values associated to each point; each marker translates into a certain mixture, and their fill to $Re = 200$ or $Re = 300$.

Since this correlation was obtained on the heat losses basis, an energy balance analysis of the flame tip can help us to better understand the results and get further information from the plot. According to Williams' second criterion for flame extinction [88], if the flame front is modeled as a slab near the wall (Figure 4.15), the generation of energy in any of its portion must approximately balance the heat losses from the slab to the surroundings. In quenching, heat losses occur mainly to the wall, for the strong temperature gradients in that direction.

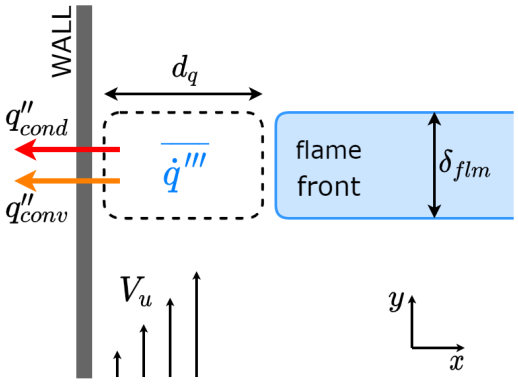

Figure 4.15: Scheme of flame extinction near the wall by conduction and convection heat losses.

We can assume by approximation that the heat generated by combustion in the quenching region ($\overline{\dot{q}'''_q}$ times the volume $d_q\,\delta_{flm}\,l$) is all lost to the wall. Let it be assumed that both conduction and convection (with a convective heat transfer coefficient h) can take place in this process, since the different correlations parameters obtained for $Re = 200$ and $Re = 300$ in Figure 4.14 suggest that the velocity of unburnt mixture influence flame quenching:

$$\overline{\dot{q}'''_q}\ (d_q\,\delta_{flm}\,l) = (\delta_{flm}\,l) \times (q''_{cond} + q''_{conv}) = (\delta_{flm}\,l)\left[\kappa\,\frac{T_{flm} - T_{wall}}{d_q} + h\,(T_{flm} - T_{wall})\right] \tag{4.13}$$

Rearranging the equation we can write:

$$\overline{\dot{q}_q'''}\, d_q = \kappa\, \frac{T_{flm} - T_{wall}}{d_q}\, \left(1 + \frac{h\, d_q}{\kappa}\right) = \kappa\, \frac{T_{flm} - T_{wall}}{d_q}\, (1 + Nu) \tag{4.14}$$

and finally:

$$\frac{\overline{\dot{q}_q'''}\, d_q^2}{\kappa\, (T_{flm} - T_{wall})} = Nu + 1 \tag{4.15}$$

The Nusselt number, Nu, represents the importance of convection over conduction heat transfer. By dimensional analysis, and for flow parallel to a flat plate, it is known to be a function of Reynolds and the Prandtl numbers:

$$Nu \propto Re^{1/2}\, Pr^{1/3} \tag{4.16}$$

With that in mind, and recalling that the chemiluminescence intensity is approximately proportional to the HRR [81], one can use the constants c_1 and c_2 to write:

$$\frac{c_1\, \overline{\dot{q}_{q,\mathrm{OH}}'''}\, d_q^2}{\kappa\, (T_{flm} - T_{wall})} = c_2\, Re^{1/2}\, Pr^{1/3} + 1 \tag{4.17}$$

As Equation 4.17 shows, a relation of the type $d_q \propto \overline{\dot{q}_q'''}^{-0.5}$ is expected for a certain Reynolds number. The exponent in the curves of Figure 4.14 was $b = -0.45$ (see Equation 4.12), which is in fact close to -0.5. The difference in value can be attributed to aspects like:

- Non pure linearity between HRR, chemiluminescence intensity and pixel signal recorded in camera CMOS (I_{OH}).
- Small variation of $T_{flm} \approx 1500\,\mathrm{K}$ for different fuel blends and ϕ, above which oxidation reactions can survive.
- Change of relative importance of radical recombination reactions for the noblest fuels, with higher concentration of light species and low activation energy reactions for the richest equivalence ratios.

The parameters c_1 and c_2 were optimized to fit the Equation 4.17 to the values of d_q and $\overline{\dot{q}_{q,\mathrm{OH}}'''}$ acquired experimentally. It was assumed the difference $T_{flm} - T_{wall}$ not to vary considerably and to be approximately equal to $1500 - 400 = 1100\,\mathrm{K}$. The thermal conductivity of the unburnt mixture κ was therefore evaluated at the mean temperature of 950 K for the different fuel blends and equivalence ratios tested. It did not change significantly and had a mean value of $\kappa = 0.0738\,\mathrm{W/(m\,K)}$ ($u_\sigma = 0.0032\,\mathrm{W/(m\,K)}$). The same occurred for Prandtl, which had a mean value of $Pr = 0.698$ ($u_\sigma = 0.010$). The final equation fitted the results with an $R^2 = 0.971$ (Figure 4.16). The determined coefficients c_1 and c_2 indicate respectively that (i) the volumetric heat generation is 51.2×10^6 times larger than the value used for the correlation, based on pixel chemiluminescence intensity value *i.e.*,

$$\overline{\dot{q}_q'''} = 51.2 \times 10^6\, \overline{\dot{q}_{q,\mathrm{OH}}'''}\,; \tag{4.18}$$

and (ii) that convective heat transfer in the quenching region is not negligible and is in the same order

of magnitude as conduction:

$$\begin{aligned} Nu+1\big|_{Re=200} &= 2.07 \Rightarrow Nu\big|_{Re=200} = 1.07 \\ Nu+1\big|_{Re=300} &= 2.76 \Rightarrow Nu\big|_{Re=300} = 1.76 \end{aligned} \tag{4.19}$$

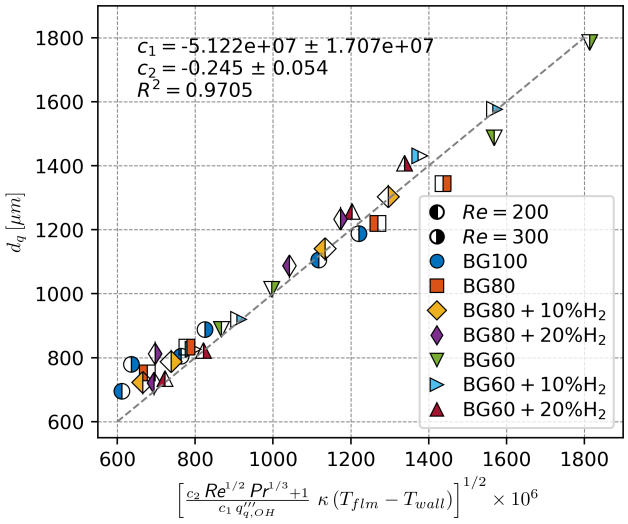

Figure 4.16: Correlation of experimental data with model describing heat losses by conduction and convection in flame quenching; each marker translates into a certain mixture, and their fill to $Re = 200$ or $Re = 300$.

There are some arguments that endorse the coefficients obtained. The first is that the maximum peak value of HRR in a freely propagating flame ranges from 0.75 GW/m^3 to 3.75 GW/m^3 for the conditions tested (according to Cantera' simulations). From the chemiluminescence results and the obtained value for c_1, the average HRR in the flame tip would range from 0.066 GW/m^3 to 0.512 GW/m^3, which is a reasonable value. Secondly, since κ and $(T_{flm} - T_{wall})$ are maintained within the same fuel blend and equivalence ratio when varying Re, one can use the parameters a (Equation 4.12) shown in Figure 4.14 for $Re = 200$ and $Re = 300$ and Equation 4.17 to state that:

$$\frac{\left[c_1\,\overline{\dot{q}'''_{q,\mathrm{OH}}}\,d_q^2\right]_{Re=300}}{\left[c_1\,\overline{\dot{q}'''_{q,\mathrm{OH}}}\,d_q^2\right]_{Re=200}} = \frac{\left[\kappa\,(T_{flm}-T_{wall})\,(Nu+1)\right]_{Re=300}}{\left[\kappa\,(T_{flm}-T_{wall})\,(Nu+1)\right]_{Re=200}} \Rightarrow \tag{4.20}$$

$$\Rightarrow \frac{\left[\overline{\dot{q}'''_{q,\mathrm{OH}}}\,d_q^2\right]_{Re=300}}{\left[\overline{\dot{q}'''_{q,\mathrm{OH}}}\,d_q^2\right]_{Re=200}} = \frac{Nu\big|_{Re=300}+1}{Nu\big|_{Re=200}+1} \approx \left(\frac{2014.6}{1730.7}\right)^2 = 1.355 \tag{4.21}$$

and, according to the information obtained from the constant c_2, this ratio is equal to $2.76/2.07 = 1.333$ (Equation 4.19), which is close and means that the differences in parameter a are justified by the different Nu numbers. Lastly, when the heat flux profiles along the wall q''_{wall} from other works [74, 75] were presented in Figure 4.4, they acknowledged the need to divide numerically obtained profiles by 1.8 to match the values of profiles obtained experimentally in quenching zone, which were based on pure conduction assumption (Equation 1.4). For their flame and based on numerical information, the Nusselt number would hence be $Nu = 0.8$: convection contributed to increase heat transfer by 80% with respect

to the pure conduction case.

We conclude then that the advection of gases next to the wall can shape the temperature profile in the quenching region and thus influence the amount of heat transferred to the wall (Equation 4.8) and d_q. The hypothesis of assuming pure heat conduction for stationary SWQ flames in the quenching region is therefore discredited with these results. It was found convection to contribute in the same order of magnitude as conduction.

Chapter 5

Conclusions

The main goal of this work was to assess the influence of hydrogen addition to biogas for the direct heat-to-electric power conversion using thermoelectric generators, to create a reliable, compact, and portable solution, useful for applications in remote and inhospitable places, not connected to the grid. The contribution of H_2 was studied not only in the perspective of the impact in system performance (TEG power and efficiency yielded), but also on how it affected velocity field, flame structure, heat release rate, and flame-wall interaction, which are decisive for flame stabilization in small combustion chambers (that portable devices entail).

Seven fuel blends were studied. BG100 and two biogas mixtures (BG60 and BG80) were chosen, to which H_2 was added up to 20%. A working range of flame conditions was also defined. Those were characterized by the mixture equivalence ratio (varied between 0.7 and 1.0) and burner Reynolds number (varied between 100 and 350). From power and efficiency measurements for those different conditions, it was realized that heat transfer processes were the key not only to explain the results observed, but also for system improvement. Two distinct zones of heat transfer (one in quenching region where conduction is important and another upstream the flame governed by convection) were defined based on results from other authors [74, 75]. For that reason, the velocity field was scrutinized using PIV techniques. Velocity magnitudes and streamlines, as well as profiles near the wall, were analyzed in the perspective of their contribution for heat convection and to explain TEG performance results. To investigate the heat transfer from flame to the wall, we turned our attention into the flame tip. Chemiluminescence information from OH^* and CH^* radicals was used to evaluate the effects of H_2 and equivalence ratio in flame structure as well as the heat release rate in that zone. That information was used together with quenching distances to understand not only the nature of quenching mechanism (heat losses and/or radical recombination reactions) for the flames tested, but also to quantify the importance of conduction and convection for the heat transferred in the quenching region.

5.1 Achievements

The main findings related with the work developed are:

1. TEG power increases largely with ϕ and slightly with Re. In opposition to TEG efficiency, heat transfer efficiency varied significantly (more than 3 times with the different conditions tested) and influenced system efficiency the most. Although η_{glob} remained the same across all fuel blends tested, power yielded by TEG changed with the fuel composition.

2. For a flame in SWQ, the decrease in gases density in the flame front induces the deviation of streamlines far away from the wall and promotes the rapid growth of a boundary layer, right after the quenching region. That reduces velocity (and temperature) gradients in the vicinity of the wall, inhibiting the heat transfer and causing most of the heat to be lost, ultimately penalizing heat transfer efficiency.

3. Adding H_2 to BG is very effective to increase power harvested in the TEG module and to decrease flame quenching distances, essential for better flame stabilization and heat transfer in downsized combustion chambers. The lower the grade of BG fuel mixture, the higher the impact of H_2: with 20% addition to BG60, P_{TEG} improved by 10% on average, and quenching distances reduced by 18%.

4. For the close relation with HRR, chemiluminescence intensity from OH^* can be used to diagnose d_q. It was found the intensity of chemiluminescence to be proportional to $d_q^{-0.45}$ for lean mixtures of any BG+H_2 fuel blends tested and for a given unburnt mixture velocity.

5. A description of flame quenching by heat losses (with a coefficient of determination $R^2 > 0.97$) explains the type of relation obtained with chemiluminescence (enunciated in point 4.) and suggest that convection is not negligible for heat transfer in quenching zone, contrarily to what is usually assumed. The unburnt mixture velocity increases the importance of convection over conduction. For $Re = 200$ and $Re = 300$, we obtained Nusselt numbers $Nu = 1.07$ and $Nu = 1.76$, respectively.

In the process, auxiliary tools and methodologies were also developed. Those were critical in the experimental work, to ensure accurate results and to allow an extended interpretation of them:

1. A mathematical model to simulate TEG operation from different fuels and flame conditions was successfully developed. It models all thermoelectric effects in the TEG and uses a useful tool (based on a neural network) to extrapolate results for other fuels and flame conditions. The coefficient of determination between mathematical model and experimental results reached $R^2 > 0.97$.

2. The choice of an adequate, fixed load resistance in TEG electrical circuit makes TEG power to vary monotonically with heat absorbed. That is useful to take conclusions regarding the amount of heat transferred only by monitoring P_{TEG}.

3. An alignment procedure, fundamental to diagnose quenching distances experimentally, was adapted from Häber and Suntz [71] to our setup and proves capable of reaching precision down to the tenth

of degree. Methods for chemiluminescence image processing and to extract information about HRR in quenching zone were also developed.

5.2 Future Work

Several proposals for system efficiency and heat transfer improvement were inferred during the analysis of TEG operation and PIV results. Those should be considered if a final concept is to be implemented:

- The placement of a barrier, parallel to the existing wall (Figure 5.1a), can help to take advantage of gases expansion, increase velocity near the wall and, consequently, convective heat transfer. Besides, the surface side which is not in contact with the flame can be covered with a thermal insulator, to reduce heat losses by natural convection.
- If a small enclosure or combustion chamber is made to help increase the gases residence time (Figure 5.1b), more heat from burnt gases would be harnessed and would not be lost to the atmosphere.
- Lower Reynolds number yielded always higher system efficiencies, even for flames near flashback. By reducing the width of the burner slits (Figure 5.1c), less powerful flames can be stabilized and the limits of efficiency for this concept (TEG + flame in SWQ) can be explored.

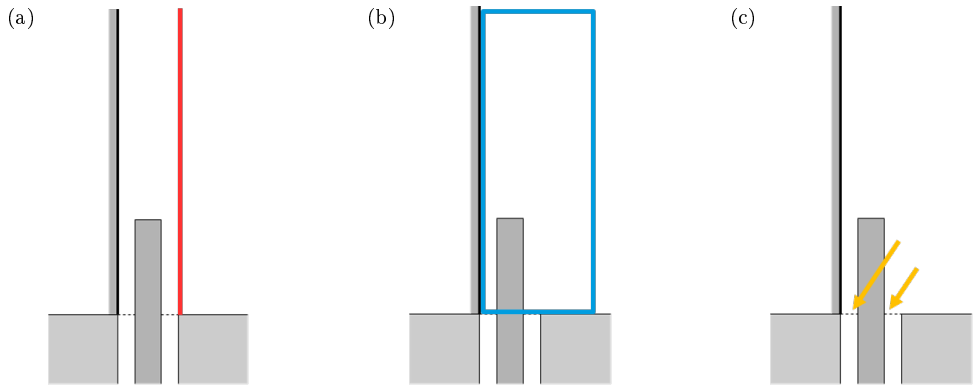

Figure 5.1: Future work proposals regarding burner and combustion chamber geometry, to (a) take advantage of gases expansion, (b) increase residence time of hot gases or even (c) stabilize less powerful flames and explore higher η_{glob}.

The use of a fixed load resistance limited the maximization of TEG power and efficiency using different conditions tested (as discussed in the beginning of chapter 4.1). Maximum Power Point Trackers are electrical devices that, for any perturbation in $R_{e,load}$ or in the amount of heat absorbed, adapt the total load resistance to maximize the power yielded. These devices performance is evaluated with their response time and behavior under different types of perturbations. Although several algorithms were developed for photovoltaic systems, the research for harvesting power with TEGs has caught less attention; those are, yet, essential for any end-use product working with TEGs. As some works suggest [89, 90], the optimization of these algorithms is an interesting control problem, which could be tackled by Mechanical Engineering students from Systems Master degree branch at IST. The progresses made in the mathematical model developed can be useful for this type of work.

Finally, the analysis of heat transfer done in this work was limited by the non-existence of temperature data. That is difficult to measure experimentally without resorting to expensive equipment nor intrusive techniques (which can be critical for such small flame). The development of numerical CFD simulations of flames in SWQ with inert walls would be useful to extend the detail of the work here developed on several levels. There is now also plenty of experimental data (from velocity field, radicals concentration or even quenching distances) that give enough bases to validate CFD simulation and hence facilitate the challenges that such work entails.

Bibliography

[1] International Energy Agency, World energy flows, 2020. URL: https://www.iea.org/sankey/.

[2] B. E. Layton, A comparison of energy densities of prevalent energy sources in units of joules per cubic meter, International Journal of Green Energy 5 (2008) 438–455. doi:10.1080/15435070802498036.

[3] Y. Apertet, H. Ouerdane, O. Glavatskaya, C. Goupil, P. Lecoeur, Optimal working conditions for thermoelectric generators with realistic thermal coupling, Epl 97 (2012) 28001. doi:10.1209/0295-5075/97/28001.

[4] T. Oliveira, Electrical Power Generation Using Thermoelectric Technology : A Detailed Study of Flame-Wall Interactions, Master's thesis, Instituto Superior Técnico, University of Lisbon, 2018.

[5] T. L. Bergman, A. S. Lavine, F. P. Incropera, D. P. Dewitt, Fundamentals of Heat and Mass Transfer, 7 ed., John Wiley & Sons, 2011.

[6] D. Beretta, N. Neophytou, J. M. Hodges, M. G. Kanatzidis, D. Narducci, M. Martin-Gonzalez, M. Beekman, B. Balke, G. Cerretti, W. Tremel, A. Zevalkink, A. I. Hofmann, C. Müller, B. Dörling, M. Campoy-Quiles, M. Caironi, Thermoelectrics: From history, a window to the future, Materials Science and Engineering R: Reports 138 (2019) 210–255. doi:10.1016/j.mser.2018.09.001.

[7] D. Champier, Thermoelectric generators: A review of applications, Energy Conversion and Management 140 (2017) 167–181. doi:10.1016/j.enconman.2017.02.070.

[8] S. Twaha, J. Zhu, Y. Yan, B. Li, A comprehensive review of thermoelectric technology: Materials, applications, modelling and performance improvement, Renewable and Sustainable Energy Reviews 65 (2016) 698–726. doi:10.1016/j.rser.2016.07.034.

[9] T. Kuroki, R. Murai, K. Makino, K. Nagano, T. Kajihara, H. Kaibe, H. Hachiuma, H. Matsuno, Research and Development for Thermoelectric Generation Technology Using Waste Heat from Steelmaking Process, Journal of Electronic Materials 44 (2015) 2151–2156. doi:10.1007/s11664-015-3722-8.

[10] J. Yang, F. R. Stabler, Automotive applications of thermoelectric materials, Journal of Electronic Materials 38 (2009) 1245–1251. doi:10.1007/s11664-009-0680-z.

[11] F. Frobenius, G. Gaiser, U. Rusche, B. Weller, Thermoelectric Generators for the Integration into Automotive Exhaust Systems for Passenger Cars and Commercial Vehicles, Journal of Electronic Materials 45 (2016) 1433–1440. doi:10.1007/s11664-015-4059-z.

[12] Q. Luo, P. Li, L. Cai, P. Zhou, D. Tang, P. Zhai, Q. Zhang, A Thermoelectric Waste-Heat-Recovery System for Portland Cement Rotary Kilns, Journal of Electronic Materials 44 (2015) 1750–1762. doi:10.1007/s11664-014-3543-1.

[13] NASA, Radioisotope power systems, 2020. URL: https://rps.nasa.gov/.

[14] Y. Xie, S. J. Wu, C. J. Yang, Generation of electricity from deep-sea hydrothermal vents with a thermoelectric converter, Applied Energy 164 (2016) 620–627. doi:10.1016/j.apenergy.2015.12.036.

[15] R. Shen, X. Gou, H. Xu, K. Qiu, Dynamic performance analysis of a cascaded thermoelectric generator, Applied Energy 203 (2017) 808–815. doi:10.1016/j.apenergy.2017.06.108.

[16] International Renewable Energy Agency, Renewable Power Generation Costs in 2018, 2019. URL: https://www.irena.org/-/media/Files/IRENA/Agency/Publication/2019/May/IRENA_Renewable-Power-Generations-Costs-in-2018.pdf.

[17] European Commission, A policy framework for climate and energy in the period from 2020 to 2030, 2014. doi:10.1007/s13398-014-0173-7.2. arXiv:9809069v1.

[18] D. Deubelin, A. Steinhauser, Biogas from Waste and Renewable Resources, Wiley - VCH, Weinheim, Germany, 2008. doi:10.1002/9783527632794.

[19] M. Tabatabaei, H. Ghavinati, Biogas: Fundamentals, Process, and Operation., Springer, Cham, Switzerland, 2018. doi:10.1007/978-3-319-77335-3.

[20] World Bioenergy Association, Global Bioenergy Statistics 2018, 2018. URL: https://worldbioenergy.org/uploads/181017%20WBA%20GBS%202018_Summary_hq.pdf.

[21] N. Scarlat, J. F. Dallemand, F. Fahl, Biogas: Developments and perspectives in europe, Renewable Energy 129 (2018) 457–472. doi:10.1016/j.renene.2018.03.006.

[22] N. Scarlat, F. Fahl, J. F. Dallemand, F. Monforti, V. Motola, A spatial analysis of biogas potential from manure in Europe, Renewable and Sustainable Energy Reviews 94 (2018) 915–930. doi:10.1016/j.rser.2018.06.035.

[23] L. Deng, Y. Liu, W. Wang, Biogas Technology, Springer Nature Singapore, 2020. doi:10.1007/978-981-15-4940-3.

[24] H. Balat, E. Kirtay, Hydrogen from biomass - Present scenario and future prospects, International Journal of Hydrogen Energy 35 (2010) 7416–7426. doi:10.1016/j.ijhydene.2010.04.137.

[25] J. O. Abe, A. P. Popoola, E. Ajenifuja, O. M. Popoola, Hydrogen energy, economy and storage: Review and recommendation, International Journal of Hydrogen Energy 44 (2019) 15072–15086. doi:10.1016/j.ijhydene.2019.04.068.

[26] J. Wang, Z. Huang, Y. Fang, B. Liu, K. Zeng, H. Miao, D. Jiang, Combustion behaviors of a direct-injection engine operating on various fractions of natural gas-hydrogen blends, International Journal of Hydrogen Energy 32 (2007) 3555–3564. doi:10.1016/j.ijhydene.2007.03.011.

[27] C. Jeong, T. Kim, K. Lee, S. Song, K. M. Chun, Generating efficiency and emissions of a spark-ignition gas engine generator fuelled with biogas-hydrogen blends, International Journal of Hydrogen Energy 34 (2009) 9620–9627. doi:10.1016/j.ijhydene.2009.09.099.

[28] E. Porpatham, A. Ramesh, B. Nagalingam, Effect of hydrogen addition on the performance of a biogas fuelled spark ignition engine, International Journal of Hydrogen Energy 32 (2007) 2057–2065. doi:10.1016/j.ijhydene.2006.09.001.

[29] C. Park, S. Park, Y. Lee, C. Kim, S. Lee, Y. Moriyoshi, Performance and emission characteristics of a SI engine fueled by low calorific biogas blended with hydrogen, International Journal of Hydrogen Energy 36 (2011) 10080–10088. doi:10.1016/j.ijhydene.2011.05.018.

[30] H. C. Barnett, R. R. Hibbard, Basic Considerations in the Combustion of Hydrocarbon Fuels with Air, National Advisory Committee for Aeronautics, 1957. URL: https://ntrs.nasa.gov/search.jsp?R=19930091007.

[31] W. Anggono, I. N. Wardana, M. Lawes, K. J. Hughes, S. Wahyudi, N. Hamidi, A. Hayakawa, Biogas laminar burning velocity and flammability characteristics in spark ignited premix combustion, Journal of Physics: Conference Series 423 (2013) 0–7. doi:10.1088/1742-6596/423/1/012015.

[32] C. Dong, Q. Zhou, X. Zhang, Q. Zhao, T. Xu, S. Hui, Experimental study on the laminar flame speed of hydrogen/natural gas/air mixtures, Frontiers of Chemical Engineering in China 4 (2010) 417–422. doi:10.1007/s11705-010-0515-8.

[33] S. R. Turns, An Introduction to Combustion - Concepts and Applications, 3rd ed., McGraw-Hill, New York, 2012.

[34] A. Di Benedetto, V. Di Sarli, E. Salzano, F. Cammarota, G. Russo, Explosion behavior of CH4/O2/N2/CO2 and H2/O2/N2/CO2 mixtures, International Journal of Hydrogen Energy 34 (2009) 6970–6978. doi:10.1016/j.ijhydene.2009.05.120.

[35] Z. L. Wei, C. W. Leung, C. S. Cheung, Z. H. Huang, Effects of equivalence ratio, H2 and CO2 addition on the heat release characteristics of premixed laminar biogas-hydrogen flame, International Journal of Hydrogen Energy 41 (2016) 6567–6580. doi:10.1016/j.ijhydene.2016.01.170.

[36] J. Li, H. Huang, Huhetaoli, Y. Osaka, Y. Bai, N. Kobayashi, Y. Chen, Combustion and Heat Release Characteristics of Biogas under Hydrogen- and Oxygen-Enriched Condition, Energies 10 (2017) 1–11. doi:10.3390/en10081200.

[37] C. L. Tang, Z. H. Huang, C. K. Law, Determination, correlation, and mechanistic interpretation of effects of hydrogen addition on laminar flame speeds of hydrocarbon – air mixtures, Proceedings of the Combustion Institute 33 (2011) 921–928. doi:10.1016/j.proci.2010.05.039.

[38] T. Poinsot, D. Veynante, Theoretical and Numerical Combustion, 3rd ed., Edwards, Philadelphia, 2012.

[39] C. K. Westbrook, A. A. Adamczyk, G. A. Lavoie, A numerical study of laminar flame wall quenching, Combustion and Flame 40 (1981) 81–99. doi:10.1016/0010-2180(81)90112-7.

[40] C. Jainski, M. Rißmann, B. Böhm, J. Janicka, A. Dreizler, Sidewall quenching of atmospheric laminar premixed flames studied by laser-based diagnostics, Combustion and Flame 183 (2017) 271–282. doi:10.1016/j.combustflame.2017.05.020.

[41] B. Boust, J. Sotton, S. A. Labuda, M. Bellenoue, A thermal formulation for single-wall quenching of transient laminar flames, Combustion and Flame 149 (2007) 286–294. doi:10.1016/j.combustflame.2006.12.019.

[42] A. Heinrich, F. Ries, G. Kuenne, S. Ganter, C. Hasse, A. Sadiki, J. Janicka, Large Eddy Simulation with tabulated chemistry of an experimental sidewall quenching burner, International Journal of Heat and Fluid Flow 71 (2018) 95–110. doi:10.1016/j.ijheatfluidflow.2018.03.011.

[43] H. Kosaka, F. Zentgraf, A. Scholtissek, C. Hasse, A. Dreizler, Effect of Flame-Wall Interaction on Local Heat Release of Methane and DME Combustion in a Side-Wall Quenching Geometry, Flow, Turbulence and Combustion 103 (2019) 181–192. doi:10.1007/s10494-019-00090-4.

[44] O. Ezekoye, R. Greif, R. F. Sawyer, Increased surface temperature effects on wall heat transfer during unsteady flame quenching, Symposium (International) on Combustion 24 (1992) 1465–1472. doi:10.1016/S0082-0784(06)80171-2.

[45] P. Popp, M. Baum, Analysis of wall heat fluxes, reaction mechanisms, and unburnt hydrocarbons during the head-on quenching of a laminar methane flame, Combustion and Flame 108 (1997) 327–348. doi:10.1016/S0010-2180(96)00144-7.

[46] F. Dabireau, B. Cuenot, O. Vermorel, T. Poinsot, Interaction of flames of H2 + O2 with inert walls, Combustion and Flame 135 (2003) 123–133. doi:10.1016/S0010-2180(03)00000-0.

[47] A. Gruber, R. Sankaran, E. R. Hawkes, J. H. Chen, Turbulent flame-wall interaction: A direct numerical simulation study, Journal of Fluid Mechanics 658 (2010) 5–32. doi:10.1017/S0022112010001278.

[48] K. T. Kim, D. H. Lee, S. Kwon, Effects of thermal and chemical surface-flame interaction on flame quenching, Combustion and Flame 146 (2006) 19–28. doi:10.1016/j.combustflame.2006.04.012.

[49] L. Q. Jiang, D. Q. Zhao, C. M. Guo, X. H. Wang, Experimental study of a plat-flame micro combustor burning DME for thermoelectric power generation, Energy Conversion and Management 52 (2011) 596–602. doi:10.1016/j.enconman.2010.07.035.

[50] S. Yadav, P. Yamasani, S. Kumar, Experimental studies on a micro power generator using thermoelectric modules mounted on a micro-combustor, Energy Conversion and Management 99 (2015) 1–7. doi:10.1016/j.enconman.2015.04.019.

[51] D. Shimokuri, Y. Taomoto, R. Matsumoto, Development of a powerful miniature power system with a meso-scale vortex combustor, Proceedings of the Combustion Institute 36 (2017) 4253–4260. doi:10.1016/j.proci.2016.06.180.

[52] B. Aravind, B. Khandelwal, S. Kumar, Experimental investigations on a new high intensity dual microcombustor based thermoelectric micropower generator, Applied Energy 228 (2018) 1173–1181. doi:10.1016/j.apenergy.2018.07.022.

[53] GENTHERM Global Power Technologies, Thermoelectric Generator 5030 Operating Manual, Calgary, Alberta, 2020. URL: https://www.globalte.com/products/thermoelectric-generators-tegs/overview.

[54] A. C. Fernandez-Pello, Micropower generation using combustion: Issues and approaches, Proceedings of the Combustion Institute 29 (2002) 883–899. doi:10.1016/s1540-7489(02)80113-4.

[55] F. Cheng, Y. Hong, C. Zhu, A Physical Model for Thermoelectric Generators With and Without Thomson Heat, Journal of Energy Resources Technology 136 (2014) 011201. doi:10.1115/1.4026280.

[56] F. Cheng, Calculation Methods for Thermoelectric Generator Performance, in: M. Nikitin, S. Skipidarov (Eds.), Thermoelectrics for Power Generation - A Look at Trends in the Technology, 2016. doi:10.5772/65596.

[57] F. Moukalled, L. Mangani, M. Darwish, The Finite Volume Method in Computational Fluid Dynamics, volume 113, Springer, Cham, Switzerland, 2015. doi:10.1007/978-3-319-16874-6.

[58] J. Kacprzyk, W. Pedrycz, Springer Handbook of Computational Intelligence, Springer, Berlin, Heidelberg, 2015. doi:10.1007/978-3-662-43505-2.

[59] D. J. C. MacKay, Bayesian Interpolation, Neural Computation 4 (1992) 415–447. doi:10.1162/neco.1992.4.3.415.

[60] F. Dan Foresee, M. T. Hagan, Gauss-Newton approximation to bayesian learning, in: IEEE International Conference on Neural Networks, volume 3, 1997, pp. 1930–1935. doi:10.1109/ICNN.1997.614194.

[61] F. Burden, D. Winkler, Bayesian regularization of neural networks, in: D. J. Livingstone (Ed.), Methods in Molecular Biology, volume 458, Humana Press, 2008, pp. 25–44. doi:10.1007/978-1-60327-101-1_3.

[62] M. Raffael, C. Willert, S. T. Wereley, J. Kompenhans, Particle Image Velocimetry - A Practical Guide, 3rd ed., Springer, 2007. doi:10.1007/978-3-319-68852-7.

[63] Dantec Dynamics, DynamicStudio User's Guide, Skovlunde, Denmark, 2016.

[64] D. G. Goodwin, H. K. Moffat, R. L. Speth, Cantera: An object- oriented software toolkit for chemical kinetics, thermodynamics, and transport processes, 2017. URL: https://cantera.org.

[65] G. Smith, D. Golden, M. Frenklach, N. Moriarty, B. Eiteneer, M. Goldenberg, C. Bowman, R. Hanson, S. Song, W. Gardiner, Gri-mech 3.0, chemical kinetic mechanism, 1999. URL: http://combustion.berkeley.edu/gri-mech/.

[66] R. B. Abernethy, R. P. Benedict, R. B. Dowdell, Asme Measurement Uncertainty, Journal of Fluids Engineering 107 (1985) 161–164. doi:10.1115/1.3242450.

[67] Joint Committee For Guides In Metrology, ISO/IEC GUIDE 98-3:2008 Evaluation of measurement data — Guide to the expression of uncertainty in measurement, September, 2008. URL: https://www.iso.org/standard/50461.html.

[68] A. Montecucco, J. Siviter, A. R. Knox, The effect of temperature mismatch on thermoelectric generators electrically connected in series and parallel, Applied Energy 123 (2014) 47–54. doi:10.1016/j.apenergy.2014.02.030.

[69] G. I. Roth, J. Katz, Five techniques for increasing the speed and accuracy of PIV interrogation, Measurement Science and Technology 12 (2001) 238–245. doi:10.1088/0957-0233/12/3/302.

[70] J. J. Charonko, P. P. Vlachos, Estimation of uncertainty bounds for individual particle image velocimetry measurements from cross-correlation peak ratio, Measurement Science and Technology 24 (2013) 065301. doi:10.1088/0957-0233/24/6/065301.

[71] T. Häber, R. Suntz, Effect of different wall materials and thermal-barrier coatings on the flame-wall interaction of laminar premixed methane and propane flames, International Journal of Heat and Fluid Flow 69 (2018) 95–105. doi:10.1016/j.ijheatfluidflow.2017.12.004.

[72] M. Mann, C. Jainski, M. Euler, B. Böhm, A. Dreizler, Transient flame-wall interactions: Experimental analysis using spectroscopic temperature and CO concentration measurements, Combustion and Flame 161 (2014) 2371–2386. doi:10.1016/j.combustflame.2014.02.008.

[73] A. Heinrich, S. Ganter, G. Kuenne, C. Jainski, A. Dreizler, J. Janicka, 3D Numerical Simulation of a Laminar Experimental SWQ Burner with Tabulated Chemistry, Flow, Turbulence and Combustion 100 (2018) 535–559. doi:10.1007/s10494-017-9851-9.

[74] T. Zirwes, T. Häber, F. Zhang, H. Kosaka, H. Bockhorn, R. Suntz, A. Dreizler, J. Janicka, 2D and 3D Numerical Simulation of Chemiluminescent Radical Concentrations During Side-Wall Quenching of Premixed Methane and Propane Flames, in: Proceedings of the European Combustion Meeting 2019, 2019, pp. 1–6.

[75] H. Kosaka, F. Zentgraf, A. Scholtissek, L. Bischoff, T. Häber, R. Suntz, B. Albert, C. Hasse, A. Dreizler, Wall heat fluxes and CO formation/oxidation during laminar and turbulent side-wall quenching

of methane and DME flames, International Journal of Heat and Fluid Flow 70 (2018) 181–192. doi:10.1016/j.ijheatfluidflow.2018.01.009.

[76] S. Ganter, A. Heinrich, T. Meier, G. Kuenne, C. Jainski, M. C. Rißmann, A. Dreizler, J. Janicka, Numerical analysis of laminar methane–air side-wall-quenching, Combustion and Flame 186 (2017) 299–310. doi:10.1016/j.combustflame.2017.08.017.

[77] C. Jainski, M. Rißmann, S. Jakirlic, B. Böhm, A. Dreizler, Quenching of Premixed Flames at Cold Walls: Effects on the Local Flow Field, Flow, Turbulence and Combustion 100 (2018) 177–196. doi:10.1007/s10494-017-9836-8.

[78] F. M. Quintino, T. P. Trindade, E. C. Fernandes, Biogas combustion: Chemiluminescence fingerprint, Fuel 231 (2018) 328–340. doi:10.1016/j.fuel.2018.05.086.

[79] N. Rocha, F. M. Quintino, E. C. Fernandes, H2 enrichment impact on the chemiluminescence of biogas/air premixed flames, International Journal of Hydrogen Energy 45 (2020) 3233–3250. doi:10.1016/j.ijhydene.2019.11.115.

[80] T. Kathrotia, U. Riedel, A. Seipel, K. Moshammer, A. Brockhinke, Experimental and numerical study of chemiluminescent species in low-pressure flames, Applied Physics B: Lasers and Optics 107 (2012) 571–584. doi:10.1007/s00340-012-5002-0.

[81] C. S. Panoutsos, Y. Hardalupas, A. M. Taylor, Numerical evaluation of equivalence ratio measurement using OH* and CH* chemiluminescence in premixed and non-premixed methane-air flames, Combustion and Flame 156 (2009) 273–291. doi:10.1016/j.combustflame.2008.11.008.

[82] S. Ganter, C. Straßacker, G. Kuenne, T. Meier, A. Heinrich, U. Maas, J. Janicka, Laminar near-wall combustion: Analysis of tabulated chemistry simulations by means of detailed kinetics, International Journal of Heat and Fluid Flow 70 (2018) 259–270. doi:10.1016/j.ijheatfluidflow.2018.02.015.

[83] R. K. Cheng, R. G. Bill, F. Robben, Experimental study of combustion in a turbulent boundary layer, Symposium (International) on Combustion 18 (1981) 1021–1029. doi:10.1016/S0082-0784(81)80106-3.

[84] T. T. Ng, R. K. Cheng, F. Robben, L. Talbot, Combustion-turbulence interaction in the turbulent boundary layer over a hot surface, Symposium (International) on Combustion 19 (1982) 359–366. doi:10.1016/S0082-0784(82)80207-5.

[85] G. Richard, D. Escudié, Turbulence effect on flame wall interaction, in: First International Symposium on Turbulent Shear Flows, 1999, pp. 519–523. URL: http://www.tsfp-conference.org/proceedings/1999/tsfp1-1999-84.pdf.

[86] M. V. Blanc, P. G. Guest, G. Von Elbe, B. Lewis, Ignition of explosive gas mixtures by electric sparks. I. Minimum ignition energies and quenching distances of mixtures of methane, oxygen, and inert gases, The Journal of Chemical Physics 15 (1947) 798–802. doi:10.1063/1.1746337.

[87] G. E. Andrews, D. Bradley, The burning velocity of methane-air mixtures, Combustion and Flame 19 (1972) 275–288. doi:10.1016/S0010-2180(72)80218-9.

[88] F. A. Williams, Combustion theory, 2nd ed., CRC Press, Boca Raton, 1985. doi:10.1201/9780429494055.

[89] J. H. Carstens, C. Gühmann, Maximum Power Point Controller for Thermoelectric Generators to Support a Vehicle Power Supply, Materials Today: Proceedings 2 (2015) 790–803. doi:10.1016/j.matpr.2015.05.099.

[90] Y. H. Liu, Y. H. Chiu, J. W. Huang, S. C. Wang, A novel maximum power point tracker for thermoelectric generation system, Renewable Energy 97 (2016) 306–318. doi:10.1016/j.renene.2016.05.001.

Appendix A

Publications

This work led to an oral presentation in an international conference:

- **M. D. Santos***, S. I. G. Dias, A. P. Gonçalves, E. C. Fernandes. "Impact of BG+H2 flames in thermoelectric power generation" in VCT2020 - Virtual Conference on Thermoelectrics, July 21-23, 2020.

and was accepted to be presented in another international conference:

- S. I. G. Dias, T. B. Oliveira, **M. D. Santos**, A. P. Gonçalves, E. C. Fernandes. "Study of Flame-wall Interactions impact on Thermoelectric Power Generation" in 5th World Congress on Momentum, Heat and Mass Transfer, Lisboa (Portugal).

to be held in April 2020, but which was postponed to October 2020 due to coronavirus pandemic.

Appendix B

Technical Datasheets

B.1 TEG GM200-49-45-30

GM200-49-45-30
Thermoelectric generator module

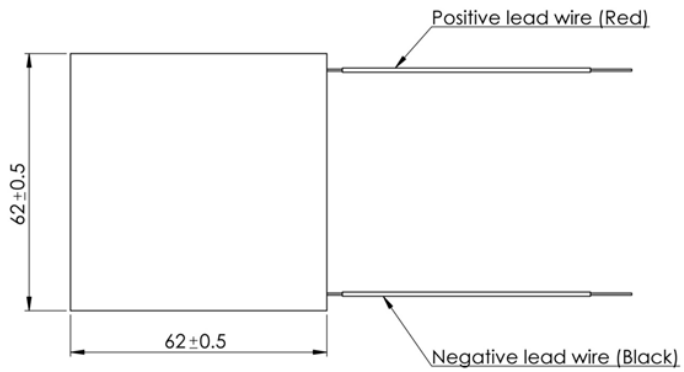

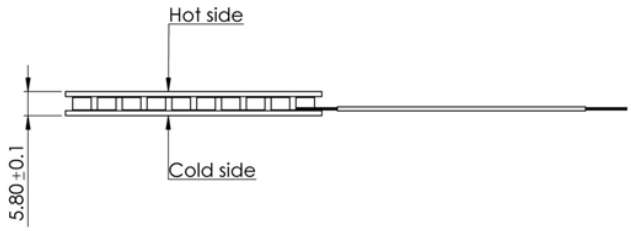

Parameters for hot side temp 200ºC and cold side temp 30ºC

Matched load output power	7.5W
Matched load resistance	0.27Ω ± 15%
Open circuit voltage	2.8V
Matched load output	5.3A
Matched load output voltage	1.4V
Heat flow through module	~149W
Maximum compress (non-destructive)	1MPa
Maximum operation temperature	Hot side - 200ºC. Cold side - 175ºC

Features

- Compact structure (no moving parts)
- Reliable performance
- Maintenance-free
- Noise-free operation
- Low-carbon, green technology

GM200-49-45-30
Thermoelectric generator module

Formulae for calculating thermoelectric properties (best fit derived from measured material characteristics)

Thermal conductivity

- $k_n = (0.0000334545 \times T^2 - 0.023350303 \times T + 5.606333)$ W/mK
- $k_p = (0.0000361558 \times T^2 - 0.026351342 \times T + 6.22162)$ W/mK

Seebeck coefficient

- $a_n = (0.001530736 \times T^2 - 1.08058874 \times T - 28.338095) \times 10^{-6}$ V/K
- $a_p = (-0.003638095 \times T^2 + 2.74380952 \times T - 296.214286) \times 10^{-6}$ V/K

Electrical conductivity

- $o_p = (0.015601732 \times T^2 - 15.708052 \times T + 4466.38095) \times 10^2$ S/m
- $o_n = (0.01057143 \times T^2 - 10.16048 \times T + 3113.71429) \times 10^2$ S/m

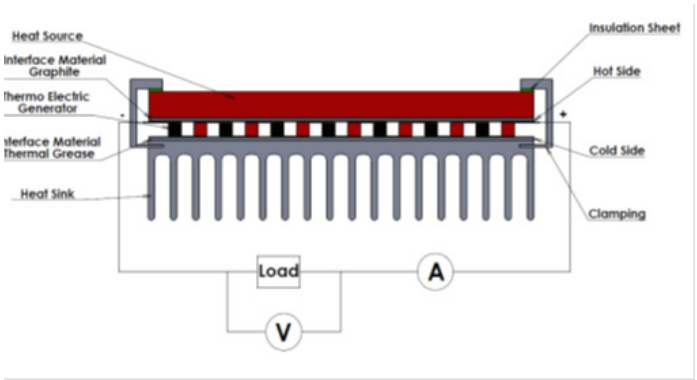

Where the subscript *n* refers to the n-type thermoelement and the subscript *p* refers to the p-type thermoelement.It should be noted here that the electrical conductivity relates to the electrical resistivity as follows: p=1/o Thus, where electrical resistivity is needed, one can calculate the electrical conductivity through the aforementioned formulae and then reverse to calculate the electrical resistivity.

Adaptive® Power Management

Adaptive is a registered trademark of European Thermodynamics Limited.
Web: www.etdyn.com Tel: +44(0)116 279 6899 E-mail: info@etdyn.com

GM200-49-45-30
Thermoelectric generator module

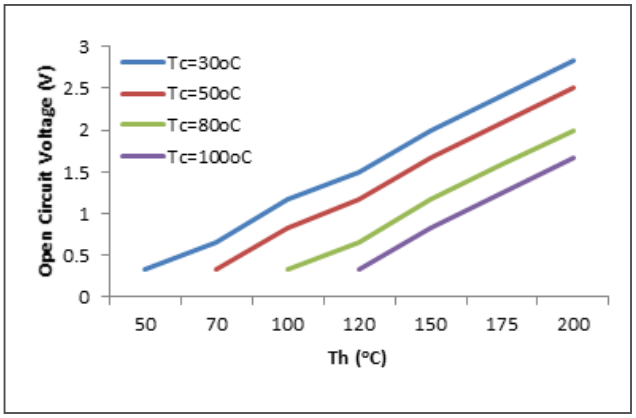

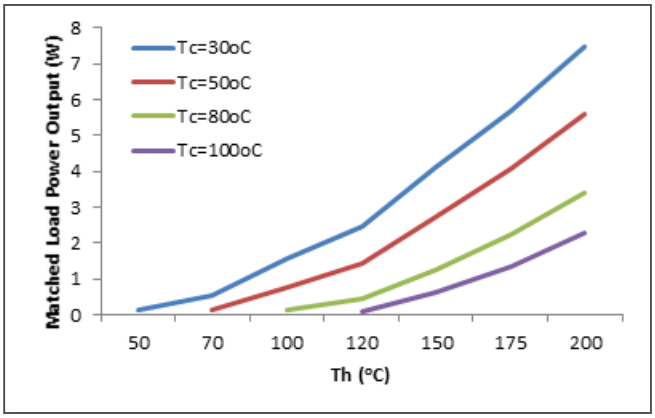

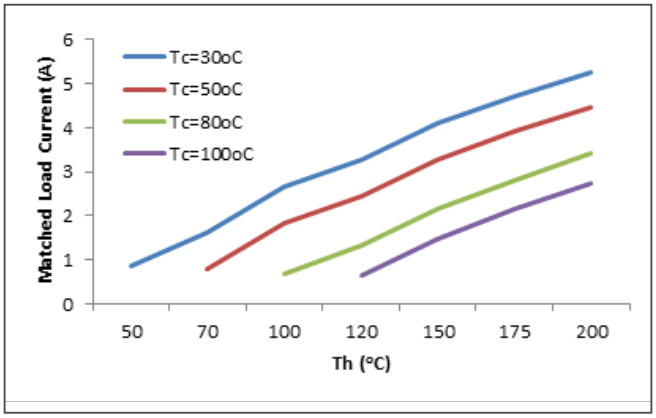

Note: Th = hot side temperature

GM200-49-45-30
Thermoelectric generator module

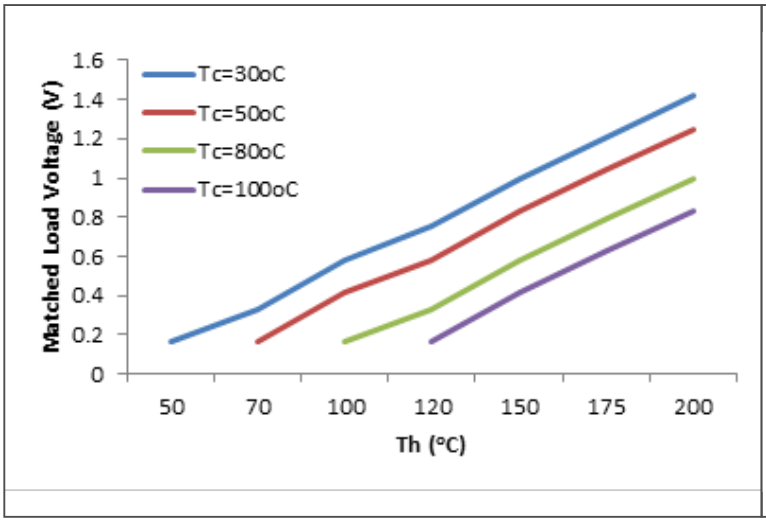

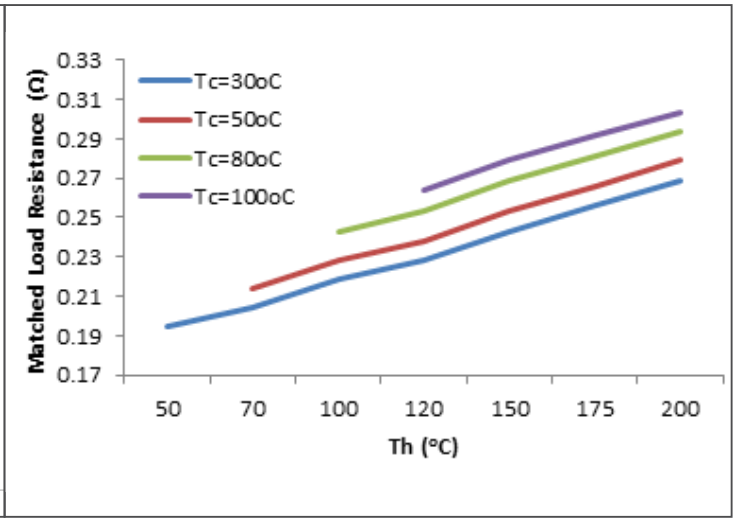

Note: Th = hot side temperature

Adaptive® Power Management

Adaptive is a registered trademark of European Thermodynamics Limited.
Web: www.etdyn.com Tel: +44(0)116 279 6899 E-mail: info@etdyn.com

Appendix C

Mathematical Model annexes

C.1 Flowchart

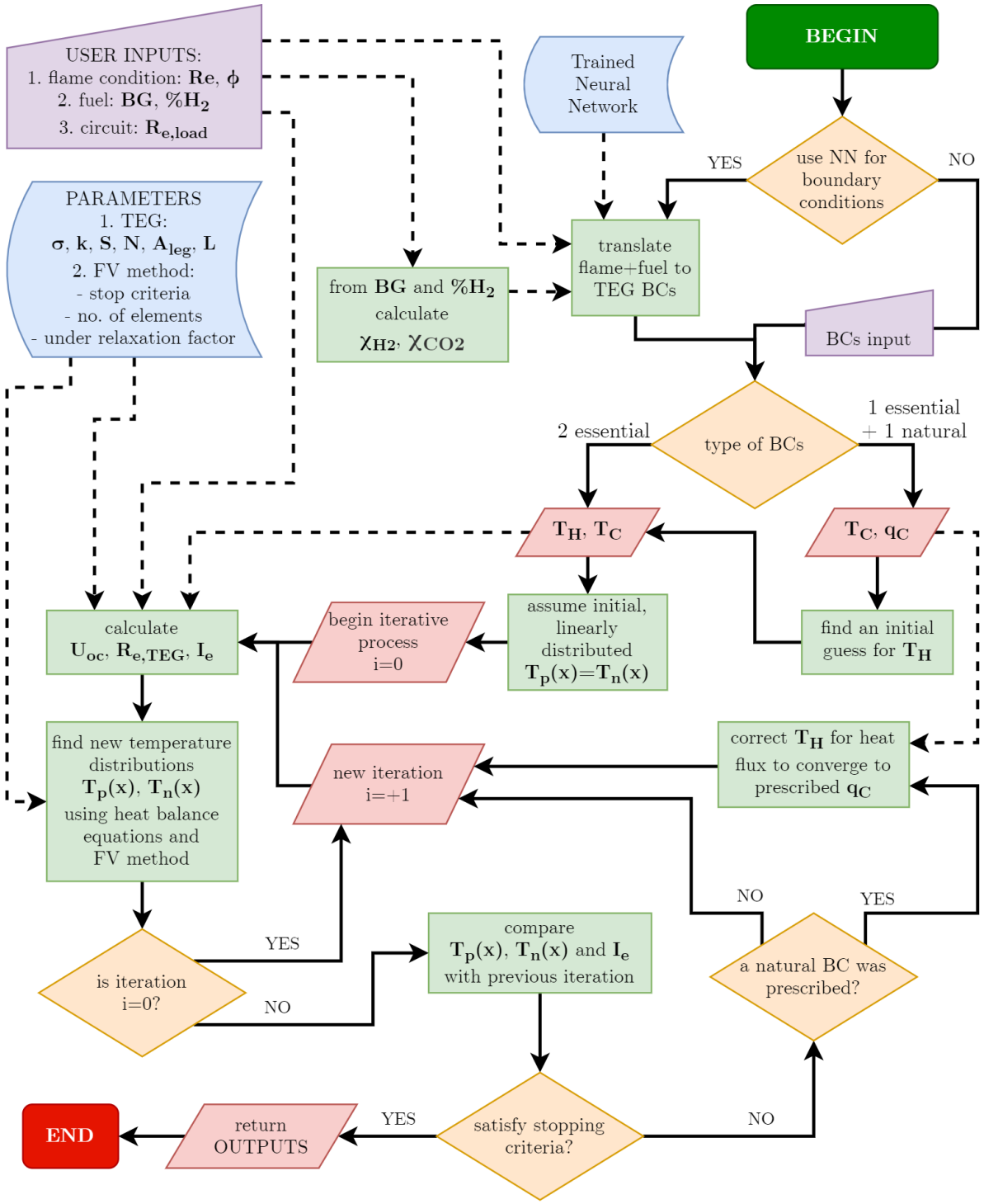

Figure C.1: Flowchart of mathematical model algorithm; continuous arrows indicate sequence flow; dashed arrows represent processes dependencies.

C.2 Neural Network fit results

As explained in section 2.3.2, a neural network uses training data to adjust its parameters and fit/interpolate the data, minimizing the error between targets and outputs from the net. The test data set can be used for posterior performance and over-fitting judgment. The coefficient of determination for testing is always smaller than training one. Nevertheless, as Figure C.2 shows, it is still very high with $R^2 = 0.9943$. This proves that the used neural network has good interpolation and generalization capabilities, without signs of over-fitting.

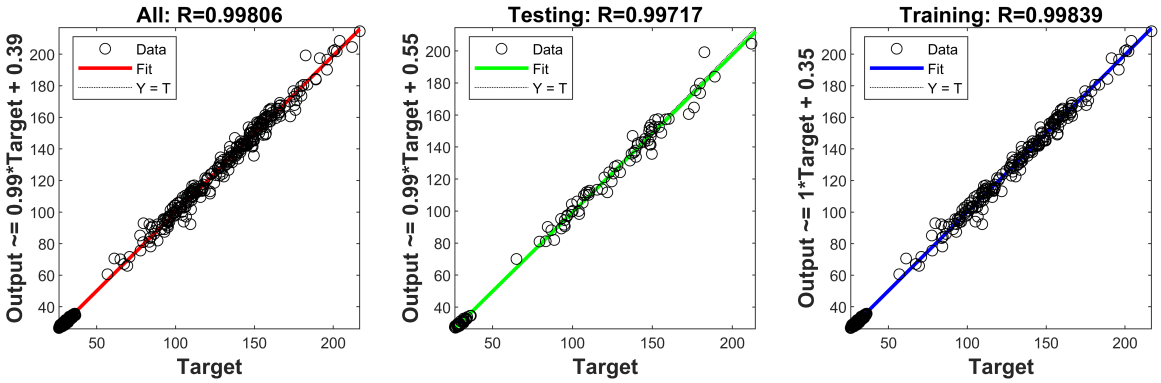

Figure C.2: Neural network training and testing regression results.

Appendix D

Results annexes

D.1 Power and efficiency maps

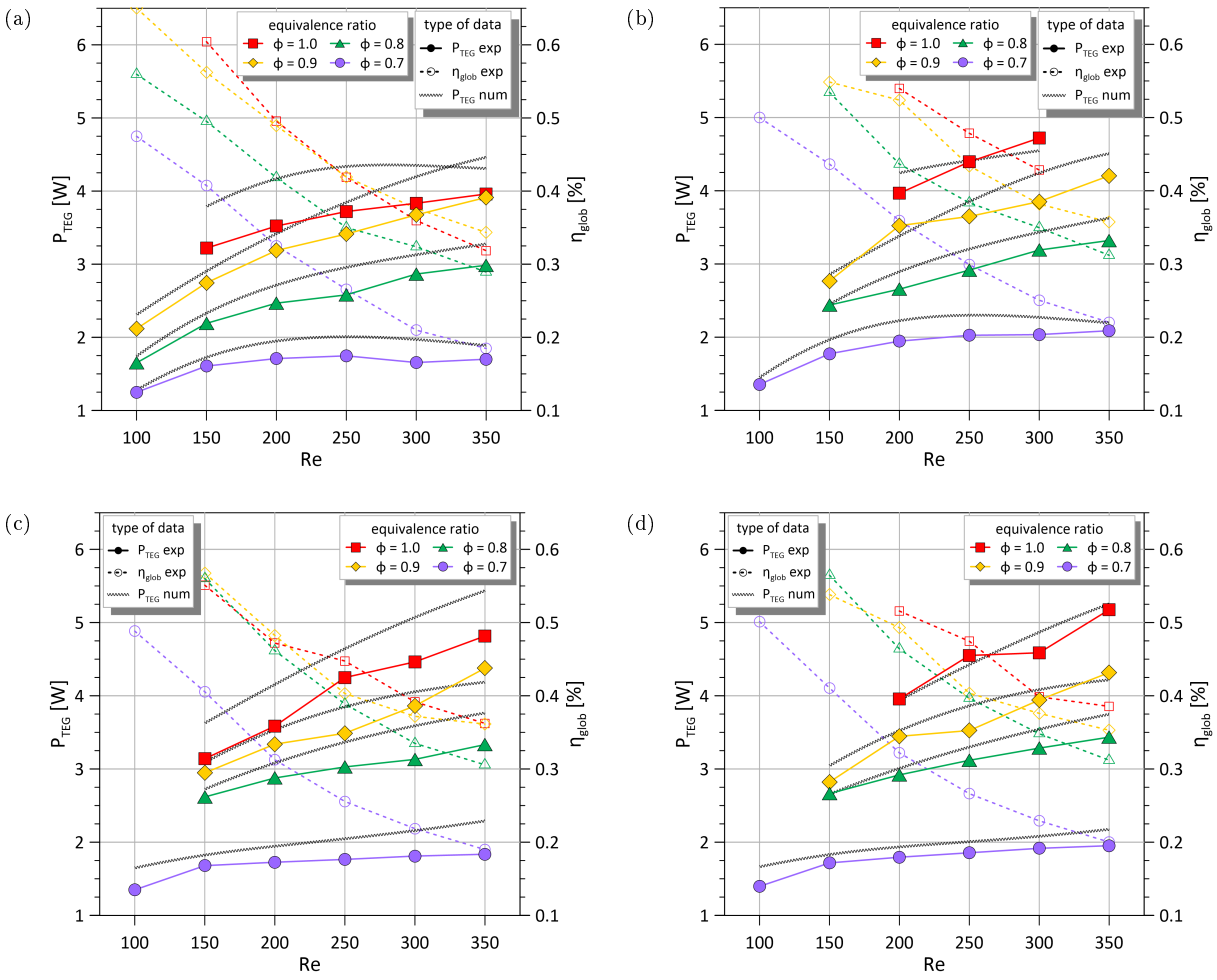

Figure D.1: Map of P_{TEG} and global efficiency η_{glob} for (a) BG60, (b) BG60+20%H_2, (c) BG80, and (d) BG80+10%H_2; filled markers linked by continuous lines indicate experimental P_{TEG} and hollow markers with dashed lines the correspond to η_{glob}; for each equivalence ratio, the black, thicker line indicate the numerically obtained P_{TEG} (by the mathematical model).

D.2 Velocity field for BG+H_2 fuel blends

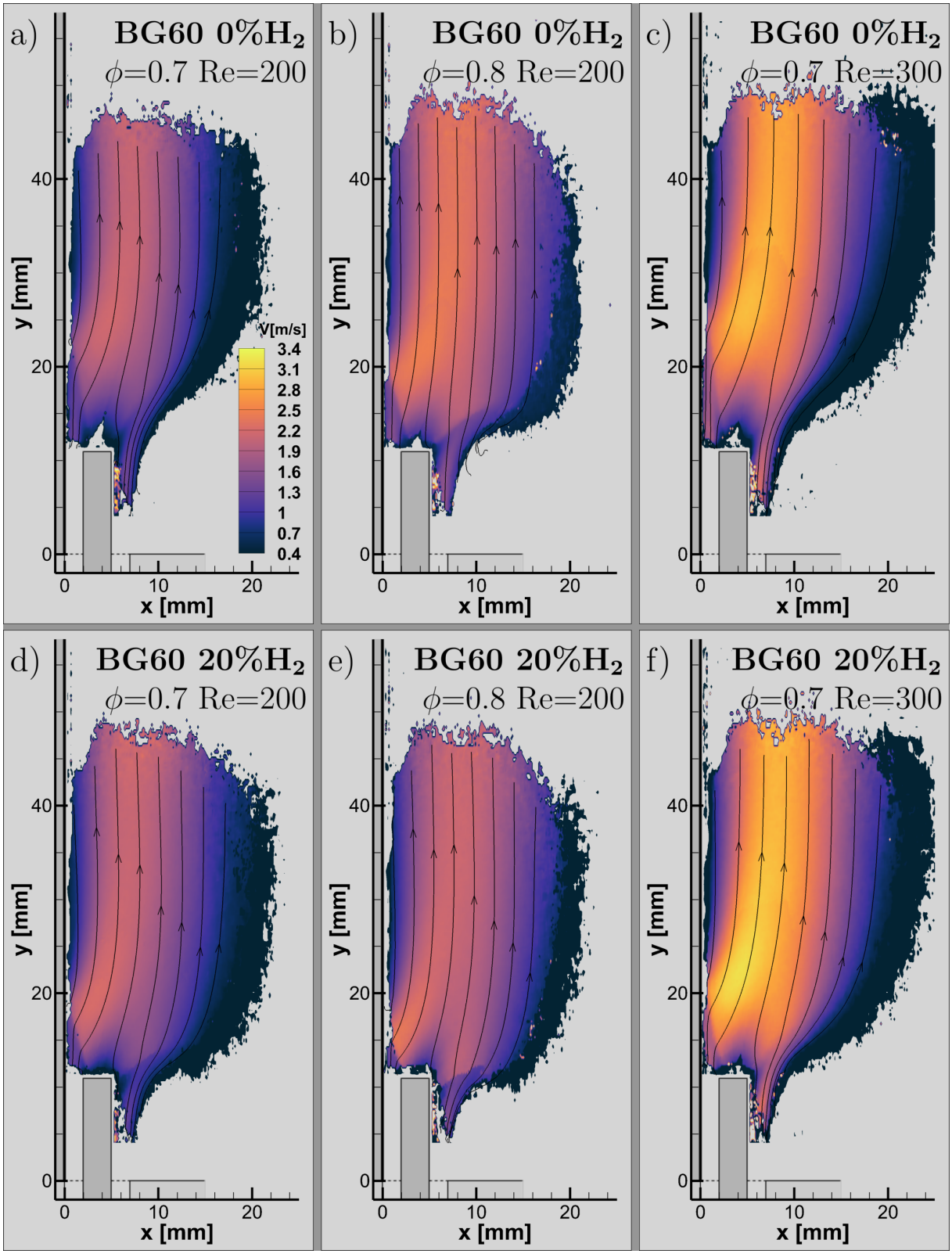

Figure D.2: Velocity fields for (a)(b)(c) BG60 and (e)(f)(g) BG60+20%H_2 fuel blends and respective influence of ϕ and Re (each column has the same flame condition); what was stated in the analysis of velocity field for BG100 (chapter 4.3) extends to these fuel blends; velocity contour scale is the same for all plots.

D.3 Detailed velocity profiles

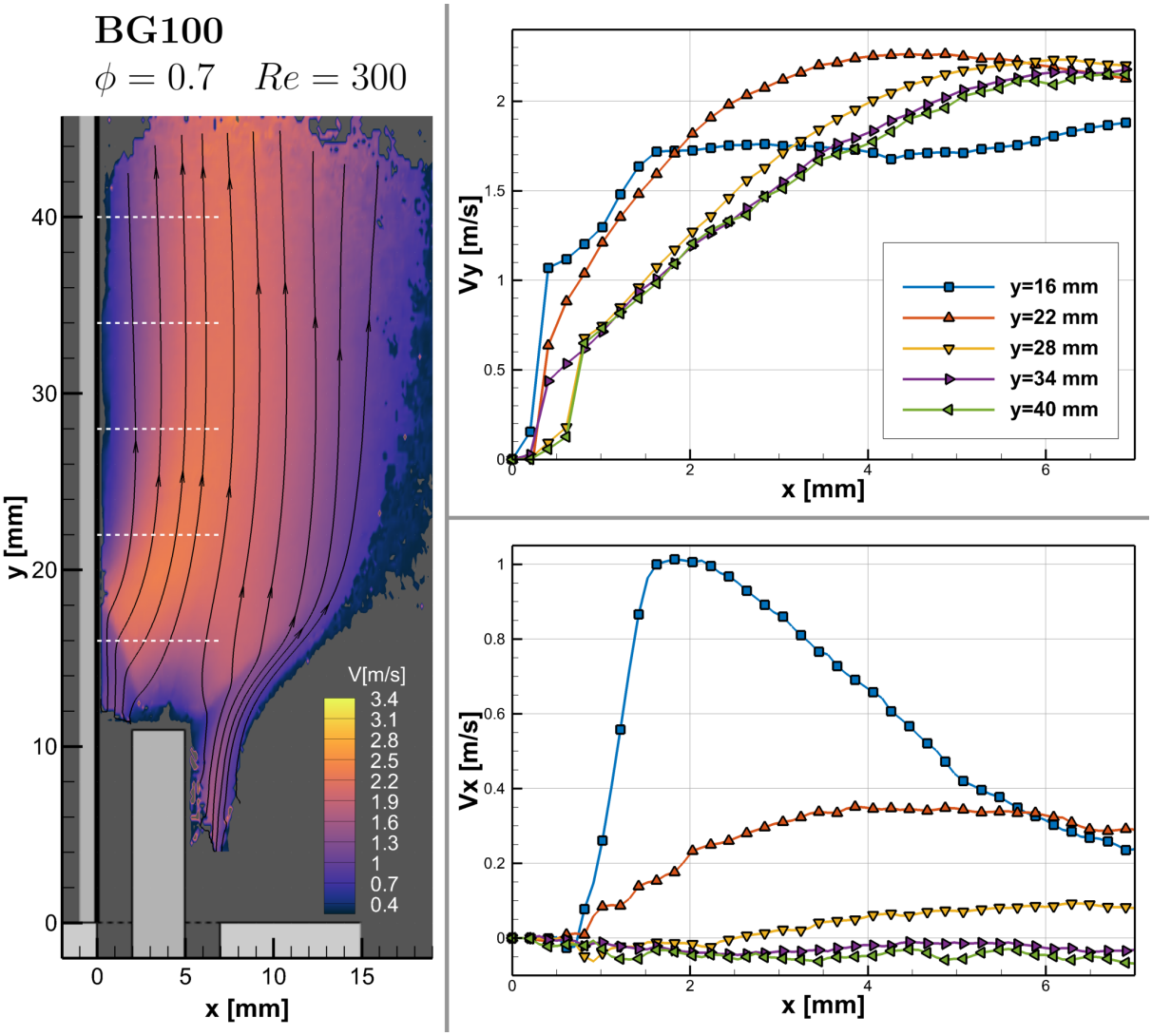

Figure D.3: Detailed V_x and V_y velocities profiles for a BG100 flame along the wall, for five different y coordinates along the wall; the accuracy of velocity estimation near the wall ($x < 0.8\,\mathrm{mm}$) is doubtful.